Blade Number Influence on Centrifugal Impeller Flow Behavior

by

Rifki Adi Nugroho

A thesis
presented to the University of Waterloo
in fulfillment of the
thesis requirement for the degree of
Master of Applied Science
in
Mechanical Engineering

Waterloo, Ontario, Canada, 2015

© Rifki Adi Nugroho 2015

I hereby declare that I am the sole author of this thesis. This is a true copy of the thesis, including any required final revisions, as accepted by my examiners.

I understand that my thesis may be made electronically available to the public.

Abstract

In this study, experiments were conducted to observe the performance and flow structure of the fluid inside the passage of 5 and 7 bladed impellers. The main purpose is to understand the influence of the number of blades on the performance and flow behavior of a centrifugal impeller. To analyze the flow behavior, the particle image velocimetry (PIV) technique that is known as a non-intrusive velocity measurements method was used. Fluid flow streamlines, mean normalized primary and secondary velocity, turbulence intensity (TI) and fluid angle deviation (β_d) were presented to understand the fluid flow behavior.

The results showed that the head rise of the fluid inside the 5 bladed impeller is lower than the 7 bladed impeller. However, the efficiency showed a similar value between the 5 and 7 bladed impeller. The PIV results showed that even though the 7 bladed impeller produced higher head rise, the losses were also higher. PIV results also showed that the influence of the number of blades on the fluid behavior was less at a high flow rate and more obvious at low flow rate.

Some significant differences of fluid behavior between the 5 and 7 bladed impellers were found. At the design flow rate, for the 5 bladed impeller, a well behaved flow structure was found. In comparison, there was separation flow on the blade pressure surface of the 7 bladed impeller that was probably caused by the high 'angle of attack'. In addition, a jet pattern that occurred near the exit of the blade pressure side appeared to be stronger for the 5 bladed impeller than the 7 bladed impeller. At low flow rates, the wake region that appeared on the blade suction side was larger for the 7 bladed impeller.

Finally, PIV measurements conducted in this study showed similarity in the performance result and flow structure with the several past studies obtained using other method measurements and visualizations. The ease and accurate results of PIV measurements suggest that this method is a potential tool to observe fluid flow inside the impeller in more detail for future studies.

Acknowledgements

First and foremost, I would like to thank God for all of the blessings He always gives to me.

This work also would not have been possible without support of a number of people to whom I am deeply in gratitude. I would like to thank my supervisor Professor D. A. Johnson for his support, encouragement, guidance, valuable knowledge and for helping me to pass through the hard times during my study in Waterloo.

Beside my advisor, I would like to thank my thesis readers, Professor John B. Medley and Professor Sean Peterson for their time and effort to read this thesis.

Special thanks to my mother Qonita who always prays for my success, my father Fachrur Rozie Hasy who never let me down and my others family Jaeni, Cucu Solihah, Safiera D. R. Utami, Jaya V. Dewata, Endah Sekarwangi and Ivan Yanuardi that encouraged me to accomplish this degree. I hope I can return what all of you have done to me.

I am also grateful to my colleagues Nicholas Tam, Faegheh Ghorbani Shohrat, Nigel Swytink-Binnema, Ahmed Abdelrahman, Kobra Gharali, Tyler Gallant and Farid Samara for willingness to offer any supports. Because all of you, Waterloo was like my home town.

I also would like to thank to Andy Barber, Jason Benninger and Robert Wagner who helped me building the new experiment test pump rig.

I thank to PT. Pupuk Kaltim and managements, Lola Karmila and her subordinates, Akhmad Rosadi and his subordinates who gave me trust, opportunity and precious support so that I can pursue my Master study.

I extend my thank to kang Aymen, mbak Adit, mas Wawan, mas Deni, mas Odie, Mbak Marry, Mbak Neny and other Indonesian families in the Region of Waterloo for for always serving delicious foods when we gathered. In addition, I must thank to mas Adhi, mas Robby, om Teddy, KJRI staffs and other Indonesian families in GTA region for being hospitality hosts when I was in GTA.

Finally, I would give my special thank to my lovely and amazing wife Febriani Sri Lestari and my hero, my life, my son Mirza Barick Sheehan Nugroho for all of your love and support. I will always love you.

Table of Contents

List of Tables viii

List of Figures ix

Nomenclature xvii

1 Introduction 1

1.1 Centrifugal pump . . . 3
1.2 Centrifugal pump performance . . . 4
1.3 Dimensionless pump performance . . . 8
1.4 Centrifugal pump efficiency and losses . . . 10
1.5 Fluid flow inside the impeller passage . . . 12
1.6 Influence of impeller geometry on centrifugal flow behaviour . . . 16
1.7 Objective . . . 22

2 Particle Image Velocimetry 24

2.1 Introduction . . . 24
2.2 Traced particle seeding . . . 26
2.3 Illumination Step . . . 29
2.4 Recording the image . . . 30
2.5 Post-Processing . . . 30

2.6 Validation . . . 32
2.7 Error in PIV . . . 33
2.8 PIV measurements of the fluid inside a centrifugal pump impeller . . . 35

3 Experimental Methodology **42**
3.1 Experimental test apparatus . . . 42
3.2 Designing and manufacturing laboratory impeller . . . 45
3.2.1 Impeller design . . . 45
3.2.2 Impeller manufacturing . . . 46
3.3 Impeller performance measurement . . . 48
3.3.1 Flow rate measurement . . . 50
3.3.2 Head rise measurement . . . 52
3.3.3 Brake horsepower measurement . . . 52
3.4 Pump performance data acquisition . . . 53
3.5 PIV measurement . . . 54
3.5.1 Camera for recording images . . . 55
3.5.2 Gemini laser system . . . 55
3.5.3 Seeding particles . . . 58
3.5.4 Calibration tool and shifting x and y position . . . 58
3.5.5 Image processing . . . 58
3.5.6 Calculating relative velocity . . . 62
3.5.7 Image and field of view . . . 64
3.5.8 PIV measurements result calculation . . . 65

4 Results and Discussion **68**
4.1 Performance results of the impellers . . . 68
4.1.1 Results of performance measurements for 5 and 7 bladed impellers . 68
4.1.2 Summary of performance results . . . 74

4.2 PIV results . . . 75
4.2.1 Introduction . . . 75
4.2.2 Mass balance calculation . . . 75
4.2.3 Flow behavior at the design and 75 % flow rates . . . 76
4.2.4 Flow behavior at high flow rates . . . 94
4.2.5 Flow behavior at low flow rates . . . 103
4.2.6 Summary of PIV results . . . 120

5 Conclusions and Recommendations **122**
5.1 Conclusions . . . 122
5.2 Recommendations . . . 123

APPENDICES **125**

A Uncertainty Analysis **126**
A.1 Uncertainty of pump performance measurements . . . 127
A.2 Uncertainty of PIV measurements . . . 127

B Uncertainty Analysis **130**

C Uncertainty Analysis **134**

References **138**

List of Tables

1.1 Descriptions of fluid velocity inside the impeller passage 8

3.1 DC motor specification 43

3.2 Impeller and blade specific geometry 46

3.3 Input data of experimental set up to the System 990N Uniflow 52

3.4 The input dimensions and the output data from The Dantec Studio software to calculate the new coordinate of the images for figure 3.17 59

4.1 Performance parameters of a 5 bladed impeller at 300 rpm 69

List of Figures

1.1 Comparison between positive displacement pump and dynamic pump characteristics, where μ = kinematic viscosity in m^2/s. Adapted from [45] . . 3

1.2 Schematic picture of general centrifugal pump 5

1.3 Effect of impeller and the diffuser to the fluid in the centrifugal pump. Adapted from [37] 5

1.4 Schematic picture of general centrifugal pump. Adapted from [45] 6

1.5 a. The centrifugal pump performance at a constant speed b. The centrifugal pump performance at a constant outlet diameter. Adapted from [45] 7

1.6 Velocity triangles at the impeller inlet and outlet of a centrifugal pump. Adapted from [45] 7

1.7 The classification of the centrifugal pump. Adapted from [15] 9

1.8 The losses occur in the centrifugal pump. Adapted from [21] 11

1.9 The slip model velocity triangle of the backward swept blade. Adapted from [37] 11

1.10 The prediction of infinite and finite number of blades flow inside the impeller. Adapted from [33] 13

1.11 2D inviscid forces of fluid inside the impeller passage. Adapted from [33] . 14

1.12 The prediction of the inviscid potential flow of fluid inside the impeller; a. the relative eddy through out the passage; b. the fluid flows inside the channel of the stationary blade; c. the sum of a and b flows. Adapted from [33] 15

1.13 Jet-wake structure in the rotating impeller. Adapted from [33] 16

1.14 Influence of the blade shape to the theoretical head of the impeller based on Euler turbomachine equation 1.2 17
1.15 Influence of the blade shape to the pump performance [11] 18
1.16 Flow structure inside the impeller (a). impeller blade exit angle (β_2) = 20^o, (b) Impeller blade exit angle (β_2) = 44^o [26] 18
1.17 The centrifugal pump performance a. H-Q curve; b. maximum efficiency curve; as a result of changing blade numbers [37] 19
1.18 Velocity profile radial and tangential velocity near inlet (top) and outlet (bottom) of a) 3 bladed impeller and b) 7 bladed impeller [32] 21
1.19 Mean normalized primary velocity (top) at: a) inlet and b) outlet and secondary velocity (bottom) at: c) inlet and d) outlet and at the design flow rate of the 8 bladed impeller obtained by Hesse and Howard [18] 22

2.1 General set up of the PIV measurement. Adapted from [3] 25
2.2 Particles shown in the plane or Image of flow field. Adapted from [3] . . . 25
2.3 Seeding particle response in turbulent flow. Adapted from [29] 27
2.4 Rayleigh scattering and mie scattering light of particle. Adapted from [35] 28
2.5 Effect of particle diameter on the light scattering in the flow. Adapted from [29] 29
2.6 General layout of the double cavity Nd:YAG laser configuration. Adapted from [40] 31
2.7 Typical timing diagram of PIV measurement. Adapted from [35] 31
2.8 The example of particles displacement peak obtained by cross correlation [12][13] 36
2.9 Vector maps of relative velocity fluid inside the passages of a centrifugal pump impeller from Pedersen [33] a). at the design flow Q/Qd b). at 0.25 Q/Qd 37
2.10 The field of fiew of PIV measurement in passage of impeller and the mean primary velocity along the passage of the impeller showing no jet-wake pattern at the design flow rate [3] 38
2.11 The streamlines of fluid flow inside the channel of impeller at the design flow rate of a. Inlet region and b. Outlet region from [3] 39

2.12 Dimensionless average relative velocity (W/u_2) inside the impeller at the design flow rate and r/R2= 0.8 a.) At Hub b.) At Shroud [44]; ξ pressure to suction side 40
2.13 Average relative velocity flow inside the impeller at high flow rate [23] . . . 41

3.1 Experimental pump testing rig top view 44
3.2 Experimental pump testing rig side view 44
3.3 Flow straightener installed downstream of the globe valve (dimensions : mm) 45
3.4 Blade geometry and notation for number of blades Z=5 47
3.5 Cross section and impeller assembly for number of blades Z= 5 47
3.6 Hub and shroud parts picture drawn in $Solidworks^{Tm}$ program 48
3.7 Pictures of 5 bladed impeller assembly 49
3.8 Layout of the straight run pipe for the ultrasound flow meter 51
3.9 Schematic diagram and picture of a Validyne pressure transducer [3] . . . 53
3.10 The layout of calibration of the pressure transducer conducted in the present 54
3.11 the calibration result of the 34.47 Kpa pressure transducer 55
3.12 Diagram of electrical circuit used to measure current and voltage of the motor 56
3.13 A picture of the experimental set up of PIV measurements 57
3.14 Wp/u_2 - θ chart in different time between pulses at a. 100 % flow rate and R/R2=0.8, b. 25 % rate flow amd R/R2=0.7 mm, the time between pulses $*$ is 50 ms, □ is 100 ms, △ is 175 ms and × is 250 ms 59
3.15 Flow visualization of 25 % flow rate at a passage of impeller for several times between pulses a. 50 μs, b. 100 μs, c. 175 μs, d. 250 μs. 60
3.16 A picture of calibration tools for the 5 and 7 bladed impellers 61
3.17 Illustration to calculate the new coordinate of the picture to the center of the impeller 61
3.18 Outlined of vectors of an interrogation region with respect to x, y and r, θ coordinate system 63
3.19 Outline of vectors at primary and secondary coordinate with respect to the primary (p) and secondary (s) coordinates 64

3.20 Illustration of 5 location measurements of the primary and secondary relative velocity for the 7 bladed impeller 65

3.21 A picture of an image particles of the 5 bladed impeller at t_d = 15 ms . . . 66

4.1 Head ($\diamond$) and efficiency ($\square$) curves for several flow rates of a 5 bladed impeller at 300 rpm 70

4.2 H-Q and WHP-Q Performance curves of a 5 bladed impeller at : $\times$ 500 rpm; $\triangle$ 400 rpm; $\square$ 300 rpm; $\diamond$ 200 rpm 71

4.3 Ψ' - ϕ' and η - ϕ' performance curves of a 5 bladed impeller at : $\times$ 500 rpm; $\triangle$ 400 rpm; $\square$ 300 rpm; $\diamond$ 200 rpm 71

4.4 The Cordier diagram [5] and points of n_s and D_s in comparison with other impellers; $\diamond$ Altaf [3]; $\triangle$ Pedersen [33]; $\circ$ This study 72

4.5 Ψ' - ϕ' performance curves of the 5 bladed impeller at : $\times$ 500 rpm; $\triangle$ 400 rpm; $\square$ 300 rpm; $\diamond$ 200 rpm and the 7 bladed impeller at :$-$ 500 rpm; + 400 rpm; $\circ$ 300 rpm; $*$ 200 rpm 73

4.6 Comparison of theoretical Euler and slip with experimental results on head and flow coefficient curve; $\times$ 7 blades theoretical head; $\diamond$ 5 blades theoretical head; $*$ 7 blades slip model head; $\square$ 5 blades slip model head; $\square$ 7 blades experimental head; $\triangle$ 5 blades experimental head 74

4.7 Comparison of flow rate calculation from PIV measurements at: $\diamond$ R/R_2 = 0.7, $\square$ R/R_2 = 0.8, $\triangle$ R/R_2 = 0.9 with ultrasonic flow meter ($\times$) 76

4.8 Fluid flow normalized streamlines at 300 rpmfor a) 5 bladed impeller 100% flow rate at t_d 15 ms, b) 5 bladed impeller 75% flow rate at t_d 15 ms, c) 7 bladed impeller 100% flow rate at t_d 0 ms, d) 7 bladed impeller 75% flow rate at t_d 0 ms 77

4.9 Normalized mean relative velocity contour to impeller tip speed at the design flow rate for a) 5 bladed impeller, b) 7 bladed impeller c) Keller [24], d) Westra [44], e) Pedersen [33] 79

4.10 Mean normalized primary velocity at : $\diamond$ R/R_2 = 0.5; $\square$ R/R_2 = 0.6; $\triangle$ R/R_2 = 0.7; $\times$ R/R_2 = 0.8; $*$ R/R_2 = 0.9 for a) 5 bladed impeller 100% flow rate, b) 5 bladed impeller 75% flow rate, c) 7 bladed impeller 100% flow rate, d) 7 bladed impeller 75% flow rate 80

4.11 Current study primary velocity results at the design flow rate at a) R/R_2 0.5; b)R/R_2 0.7; c) R/R_2 0.9 and radial velocity obtained by LDV (black line) and PIV (blue line) from Pedersen [33] at the design flow rate for d) R/R_2 0.5; e)R/R_2 0.75; f) R/R_2 0.98 82

4.12 Mean normalized secondary velocity at : $\diamond$ $R/R_2 = 0.5$; $\square$ $R/R_2 = 0.6$; $\triangle$ $R/R_2 = 0.7$; $\times$ $R/R_2 = 0.8$; $*$ $R/R_2 = 0.9$ for a) 5 bladed impeller 100% flow rate, b) 5 bladed impeller 75% flow rate, c) 7 bladed impeller 100% flow rate, d) 7 bladed impeller 75% flow rate 83

4.13 Mean normalized secondary velocity at the design flow from Altaf [3] of a) the inlet of the impeller; b) the outlet of the impeller 85

4.14 Comparison of the head rise of fluid inside the 5 bladed impeller at: $\diamond$ = design flow rate; $\triangle$ = 75% flow rate; $\times$ = 140% flow rate and the 7 bladed impeller at the design flow rate ($\square$) 85

4.15 Comparison of mean normalized primary velocity between the 5 and 7 bladed impellers at the design flow rate obtained. $\diamond$ 5 bladed impeller at $R/R_2 = 0.5$; $\square$ 7 bladed impeller at $R/R_2 = 0.5$; $\triangle$ 5 bladed impeller at $R/R_2 = 0.9$; $\times$ 7 bladed impeller at $R/R_2 = 0.9$ 87

4.16 Comparison of passage geometry between: a. 5 bladed impeller and b. 7 bladed impeller 87

4.17 Fluid flow turbulence intensity inside the impeller passage for a) 5 bladed impeller 100% flow rate, b) 5 bladed impeller 75% flow rate, c) 7 bladed impeller 100% flow rate, d) 7 bladed impeller 75% flow rate 89

4.18 The influence of inlet fluid velocity on the fluid angle at the impeller inlet, a) low velocity; b) high velocity 90

4.19 Fluid angle deviation in the impeller passage for a) 5 bladed impeller 100% flow rate, b) 5 bladed impeller 75% flow rate, c) 7 bladed impeller 100% flow rate, d) 7 bladed impeller 75% flow rate 92

4.20 Fluid flow angle at the design flow rate for a) Altaf [3], b) Pedersen [33], c) Westra [44] 93

4.21 Fluid flow normalized streamlines at 300 rpm for a) 5 bladed impeller 140% flow rate t_d 0 ms, b) 5 bladed impeller 120% flow rate t_d 0 ms, c) 7 bladed impeller 140% flow rate t_d 0 ms, d) 7 bladed impeller 120% flow rate t_d 0 ms 95

4.22 Normalized mean relative velocity contour to impeller tip speed at high flow rate for a) 140% 5 bladed impeller, b) 140% 7 bladed impeller, c) 150% Keller [24], d) 150% Westra [44], ... 96

4.23 Mean normalized primary velocity at : $\diamond$ $R/R_2 = 0.5$; $\square$ $R/R_2 = 0.6$; $\triangle$ $R/R_2 = 0.7$; $\times$ $R/R_2 = 0.8$; $*$ $R/R_2 = 0.9$ for a) 5 bladed impeller 140% flow rate, b) 5 bladed impeller 120% flow rate, c) 7 bladed impeller 140% flow rate, d) 7 bladed impeller 120% flow rate 98

4.24 Mean normalized secondary velocity at $*$ $R/R_2 = 0.9$; $\times$ $R/R_2 = 0.8$; $\triangle$ $R/R_2 = 0.7$, $\square$ $R/R_2 = 0.6$, $\diamond$ $R/R_2 = 0.5$ for a) 5 bladed impeller 140% flow rate, b) 5 bladed impeller 120% flow rate, c) 7 bladed impeller 140% flow rate, d) 7 bladed impeller 120% flow rate 99

4.25 Comparison of Mean normalized primary velocity at 140% flow rate of the 5 bladed impeller at $\diamond$ R/R_2 0.5 and $\square$ R/R_2 0.9 and the 7 bladed impeller at $\triangle$ R/R_2 0.5 and $*$ R/R_2 0.9 101

4.26 Fluid flow turbulence intensity inside the impeller passage for a) 5 bladed impeller 140% flow rate, b) 5 bladed impeller 120% flow rate, c) 7 bladed impeller 140% flow rate, d) 7 bladed impeller 120% flow rate 102

4.27 Normalized turbulence intensity to rotational impeller $k_2^* D$ at 150% flow rate conducted by Keller [23] 103

4.28 Fluid angle deviation in the impeller passage for a) 5 bladed impeller 140% flow rate, b) 5 bladed impeller 120% flow rate, c) 7 bladed impeller 140% flow rate, d) 7 bladed impeller 120% flow rate 104

4.29 Fluid flow normalized streamlines at 300 rpm for a) 5 bladed impeller 50% flow rate at t_d of 15 ms, b) 5 bladed impeller 25% flow rate at t_d of 15 ms, c) 7 bladed impeller 50% flow rate at t_d of 0 ms, d) 7 bladed impeller 25% flow rate at t_d of 0 ms 106

4.30 Oil flow surface of a 7 bladed impeller at 33% flow rate conducted by Murakami *et al.* [32] 107

4.31 Normalized mean relative velocity contour to impeller tip speed at high flow rate for a) 50% 5 bladed impeller, b) 50% 7 bladed impeller, c) 40% Keller [24], d) 40% Westra [44] 108

4.32 Fluid flow instantaneous streamlines at 25% flow rate for a) 5 bladed impeller at t_d of 0 ms, b) 5 bladed impeller at t_d of 15 ms, c) 7 bladed impeller at t_d of 0 ms, d) 7 bladed impeller at t_d of 14 ms 110

4.33 Mean normalized primary velocity at $*$ $R/R_2 = 0.9$; $\times$ $R/R_2 = 0.8$; $\triangle$ $R/R_2 = 0.7$, $\square$ $R/R_2 = 0.6$, $\diamond$ $R/R_2 = 0.5$ for a) 5 bladed impeller 50% flow rate, b) 7 bladed impeller 25% flow rate, c) 7 bladed impeller 50% flow rate, d) 7 bladed impeller 25% flow rate 111

4.34 Mean normalized secondary velocity at $*$ $R/R_2 = 0.9$; $\times$ $R/R_2 = 0.8$; $\triangle$ $R/R_2 = 0.7$, $\square$ $R/R_2 = 0.6$, $\diamond$ $R/R_2 = 0.5$ for a) 5 bladed impeller 50% flow rate, b) 5 bladed impeller 25% flow rate, c) 5 bladed impeller 50% flow rate, d) 7 bladed impeller 25% flow rate 112

4.35 Primary and secondary velocity profile of a 7 bladed impeller at 65% flow rate at the impeller inlet (a) and outlet (b) conducted by Murakami *et al.* [32] 113

4.36 Fluid flow turbulence intensity inside the impeller passage for a) 5 bladed impeller 50% flow rate, b) 5 bladed impeller 25% flow rate, c) 7 bladed impeller 50% flow rate, d) 7 bladed impeller 25% flow rate 116

4.37 Turbulence intensity (TI) at the quarter flow rate obtained by Pedersen [33] 117

4.38 Fluid angle deviation in the impeller passage for a) 5 bladed impeller 50% flow rate, b) 5 bladed impeller 25% flow rate, c) 7 bladed impeller 50% flow rate, d) 7 bladed impeller 25% flow rate 118

4.39 Fluid angle deviation at quarter load design results by Pedersen [33] 119

B.1 WHP Performance curves of the 5 bladed impeller at: $\times$ 500 rpm; $\triangle$ 400 rpm; $\square$ 300 rpm; $\diamond$ 200 rpm and the 7 bladed impeller at :$-$ 500 rpm; $+$ 400 rpm; $\circ$ 300 rpm; $*$ 200 rpm 130

B.2 H-Q Performance curves of the 5 bladed impeller at: $\times$ 500 rpm; $\triangle$ 400 rpm; $\square$ 300 rpm; $\diamond$ 200 rpm and the 7 bladed impeller at :$-$ 500 rpm; $+$ 400 rpm; $\circ$ 300 rpm; $*$ 200 rpm 131

B.3 BHP curves of the 5 bladed impeller at: $\times$ 500 rpm; $\triangle$ 400 rpm; $\square$ 300 rpm; $\diamond$ 200 rpm and the 7 bladed impeller at :$-$ 500 rpm; $+$ 400 rpm; $\circ$ 300 rpm; $*$ 200 rpm 131

B.4 efficiency curves of the 5 bladed impeller at $\diamond$ 200 rpm and the 7 bladed impeller at $*$ 200 rpm 132

B.5 Efficiency curves of the 5 bladed impeller at $\square$ 300 rpm and the 7 bladed impeller at$\circ$ 300 rpm 132

B.6 Efficiency curves of the 5 bladed impeller at△ 400 rpm and the 7 bladed impeller at + 400 rpm 133

B.7 Efficiency curves of the 5 bladed impeller at × 500 rpm and the 7 bladed impeller at − 500 rpm 133

C.1 Fluid flow normalized streamlines for a) 5 bladed impeller 140% flow rate t_d 15 ms, b) 5 bladed impeller 120% flow rate t_d 15 ms, c) 7 bladed impeller 140% flow rate t_d 15 ms, d) 7 bladed impeller 120% flow rate t_d 15 ms . . . 135

C.2 Fluid flow normalized streamlines for a) 5 bladed impeller 100% flow rate t_d 0 ms, b) 5 bladed impeller 75% flow rate t_d 0 ms, c) 7 bladed impeller 100% flow rate t_d 15 ms, d) 7 bladed impeller 75% flow rate t_d 15 ms 136

C.3 Fluid flow normalized streamlines for a) 5 bladed impeller 50% flow rate t_d 0 ms, b) 5 bladed impeller 25% flow rate t_d 0 ms, c) 7 bladed impeller 50% flow rate t_d 15 ms, d) 7 bladed impeller 25% flow rate t_d 15 ms 137

Nomenclature

α	Fluid angle [^{o}]
β	Blade angle [^{o}]
β_1	Inlet blade angle [^{o}]
β_2	Outlet blade angle [^{o}]
β_d	Fluid angle deviation [^{o}]
β_r	Absolute fluid angle [^{o}]
η	Efficiency [%]
$\mathcal{T}$	Torque coefficient [-]
μ	Fluid viscosity [m^2/s]
Φ	Flow coefficient [-]
Ψ	Head coefficient [-]
ρ	Fluid density [kg/m^3]
σ	Slip factor [-]
τ	Pump torque [-]
Θ	Angle between radius r and inlet radius r_i [^{o}]
ξ	Impeller passage dimensionless angle [-]
b_1	Inlet blade height [mm]

b_2	Outlet blade height [mm]
b_s	Inlet shrouded blade height [mm]
D_s	Specific diameter [-]
H	Pressure head [m]
H_{th}	Theoretical head [m]
I	DC motor current [Ampere]
n	Rotational speed [rpm]
n_s	Specific speed [-]
P	Shaft power [Watt]
P_{th}	Theoretical required Power [Watt]
Q	Flow rate $[m^3/h]$
R	Blade radius [m]
R_i	Inlet radius impeller [m] (unless specified)
R_o	Outlet radius impeller [m] (unless specified)
R_s	Inner shrouded radius [m] (unless specified)
t_b	Blade thickness [mm]
t_d	Laser pulse delay time [ms]
t_h	Hub thickness [mm]
t_s	Shroud thickness [mm]
TKE	Turbulence kinetic energy [-]
u_1	Inlet tangential velocity [m/s]
u_2	Outlet tangential velocity [m/s]
V_{DC}	DC motor voltage [Volt]

v_{n2} Inlet meridian velocity [m/s]

v_{n2} Outlet meridian velocity [m/s]

v_{t2} Normal component of inlet absolute velocity [m/s]

v_{t2} Normal component of outlet absolute velocity [m/s]

v'_{t2} Normal component of slip the absolute velocity [m/s]

W_1 Inlet relative velocity [m/s]

W_2 Outlet relative velocity [m/s]

W_p Relative velocity in primary coordinates [m/s]

W_p/u_2 Mean primary relative velocity to outlet rotational impeller velocity [-]

W_s Relative velocity in secondary coordinates [m/s]

W_s/u_2 Mean secondary relative velocity to outlet rotational impeller velocity [-]

BHP Brake horsepower [Watt]

PS Pressure side

SS Suction side

WHP Water horsepower [Watt]

Z Number of blades [-]

Chapter 1

Introduction

Industries that involve fluid in their processes require machines to transfer the energy either to add energy to the fluid or extract energy from the fluid. Particularly, the machines that extract energy from fluid are known as turbines, whereas the machines that add energy to the fluid are known as pumps, compressors and fans (blowers). Pumps are used to add energy to liquids, on the other hand compressors and fans are used to add energy to gases. Pumps are often applied in the critical units in a plant such as a condensate pump in the Rankine cycle. Therefore, pumps have an important role in the process of an industrial plant.

Pumps have been used for a long period to help human life especially in the agricultural sector. Two famous pumps found before in the earlier times are the undershot-bucket waterwheels (*norias*) and Archimedes' screw pump [45]. Then, pumps were developed and improved in design to get better performance and efficiency. However, even though pumps have been studied continuously from the past, many pump problems still occur in term of design, maintenance and operation. Fluid flow inside the pump can be studied in order to improve the design. Engineers want pumps to operate for a long life with minimum maintenance required so the operating costs can be reduced. In addition, engineers want pumps that can be operated safely in a wide range of conditions. Consequently, many researchers are still interested in studying pumps.

Pumps, based on the characteristic of the design, are categorized into positive displacement pumps and dynamic pumps. Specifically, pumps that presses and displaces the fluid in a given volume of liquid are known as positive displacement pumps. By comparison, dynamic pumps means that the volume is not constant; it changes depending on the flow path of the fluid. The detailed classifications of positive displacement pumps are [45]:

- Reciprocating
    1. Piston or Plunger
    2. Diaphragm
- Rotary
    1. single rotor : sliding vane, flexible tube or lining, screw and peristaltic
    2. Multiple rotor : gear, lobe, screw and circumferential piston

The detailed classifications of dynamic or turbomachine pumps are

- Rotary or Centrifugal
    1. Centrifugal or radial exit flow
    2. axial flow
    3. mixed flow
- Special design
    1. Jet pump or ejector pump
    2. Electromagnetic pumps for liquid metals
    3. Fluid-actuated : gas lift or hydraulic ram

Distinctions between the positive displacement and the dynamic pump are shown in figure 1.1.

Dynamic pumps can be operated over a wide range of flow rate at a certain speed but they have poor performance when handling high viscosity fluid. On the other hand, positive displacement pumps can operate at very high pressure at a certain flow rate; the pressure is limited by a pressure relief valve to prevent pump damage. A positive displacement pump has good performance even when it handles high-viscosity fluid. In an application, pumps should be chosen at the suitable range of operation which depends on the pressure and the flow rate of the system. Because centrifugal pumps have a wide range of operational conditions compared to positive displacement, this kind of pump dominates in industrial plants.

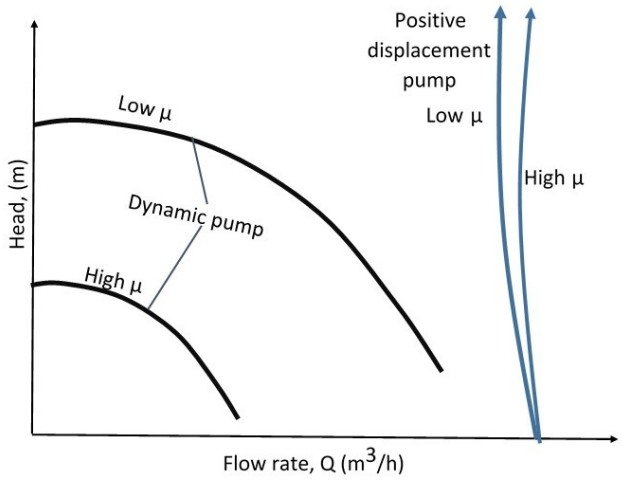

Figure 1.1: Comparison between positive displacement pump and dynamic pump characteristics, where μ = kinematic viscosity in m^2/s. Adapted from [45]

1.1 Centrifugal pump

The classifications of pumps based on the flow direction are radial or centrifugal flow, axial flow and mixed flow. The centrifugal or radial pump type changes the fluid flow direction from horizontal to vertical or radial direction. The flow direction of centrifugal pumps generally changes from axial at the inlet to radial as the fluid moves toward the outlet. The flow direction of the axial type pumps is parallel with the shaft whereas for the mixed flow type pumps, the fluid flows both axially and radially. For axial pumps, the centrifugal effect has no contribution in energy transfer. Pump type selection depends on the operating conditions which is discussed later.

Generally, the main parts of centrifugal or radial pumps are a combination between the rotating parts which are vanes or impeller and shaft, and stationary part which is the diffuser or volute (figure 1.2). The working principle of a centrifugal pump is the liquid axially flows toward impeller inlet through the impeller eye. Then, the rotor rotation causes a pressure drop at the impeller inlet. Consequently, the fluid flows from the reservoir tank toward the impeller inlet. Then, the fluid flows radially outward in the passage to the impeller exit. The fluid kinetic energy increases because it experiences the centrifugal force which is caused by the impeller rotation and radius increase. When the fluid moves toward the impeller outlet, fluid pressure also increases due to the diffuser geometry of

the impeller passage. The fluid then is guided to the discharge through the volute or the diffuser. In the volute, the kinetic energy is converted into fluid pressure also because of the diffuser geometry (figure 1.3).

Based on the casing type, centrifugal pumps can be classified as single volute or double volute. The double volute type is usually designed for reducing the radial load of the pump. However, it is noted that designing a centrifugal pump using a double volute type decreases the efficiency slightly because the double volute casing increases the contact surface area between the fluid and stationary part so the losses increase. Most of the centrifugal pump applications in industry still use the single volute type.

Based on the suction type, the centrifugal pump can be categorized as single suction and double suction pump. The double suction type is designed to reduce the axial thrust of the pump and usually used for high flow rate operating conditions.

The impeller of the centrifugal pumps can be classified as open and closed type impeller based on the mechanical construction. There is no shroud or side wall on the top of the vanes for the open type impeller, whereas the closed type has the shroud. Engineers design the open type impeller for high flow rate and low pressure, whereas the closed type impellers can be used for high pressure and high flow rate. Open type impellers are also designed to deliver very dense liquids.

1.2 Centrifugal pump performance

Engineers identify centrifugal pumps performance through several parameters which are fluid flow rate (Q), head (H), shaft power (P), efficiency (η) and noise generated by the machine (dB). Head is the pressure rise of the centrifugal pump between the suction and the discharge of a pump and it is usually expressed in unit of height. Shaft power is the power required to deliver the required fluid flow rate. Generally, centrifugal pump performance is drawn as seen in figure 1.4. The centrifugal pump performance curve is obtained by doing an experiment (performance tests). Typically, centrifugal pump head decreases as the flow rate increases while the power required increases. Centrifugal pump efficiency has a maximum value at a certain flow rate called Best Efficiency Point (BEP) or it is usually known as rating design of a centrifugal pump.

Rotational speed (n), fluid density (ρ), fluid viscosity (μ) and pump geometry are other parameters which have an influence on centrifugal pump performance. Figure 1.5 shows the effect of the rotational speed and the impeller size on centrifugal pump performance.

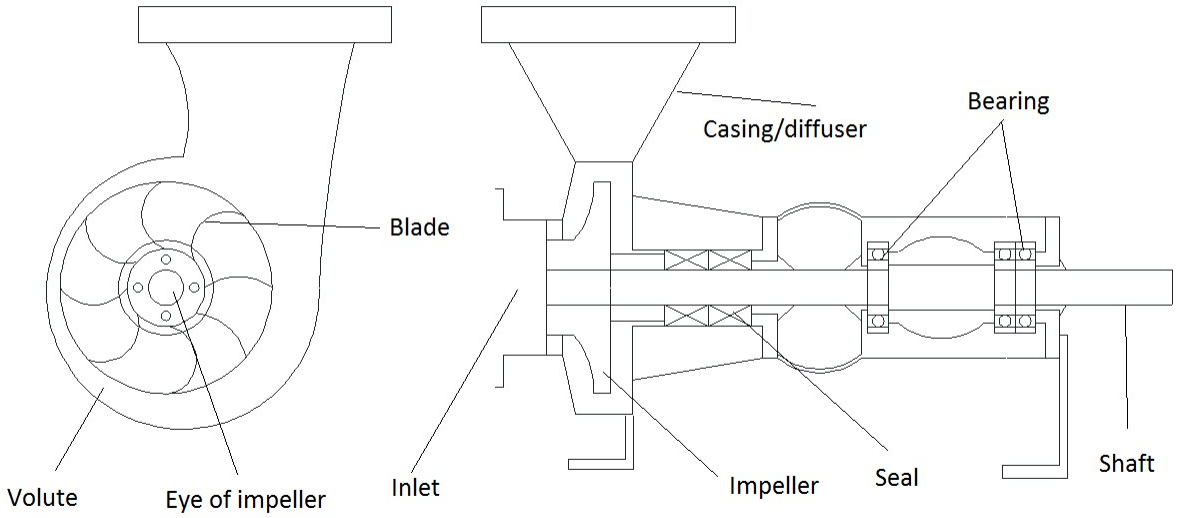

Figure 1.2: Schematic picture of general centrifugal pump

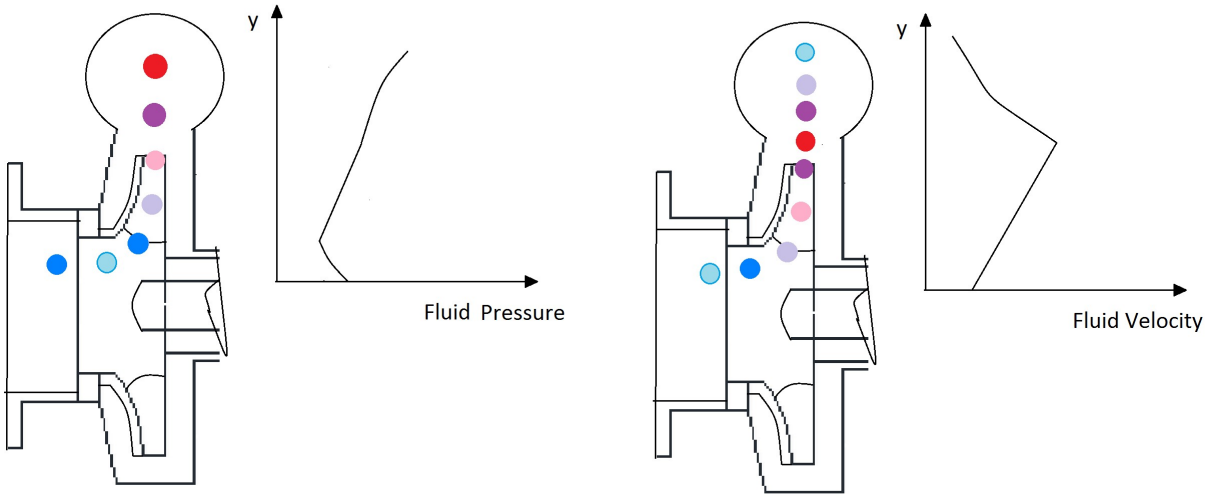

Figure 1.3: Effect of impeller and the diffuser to the fluid in the centrifugal pump. Adapted from [37]

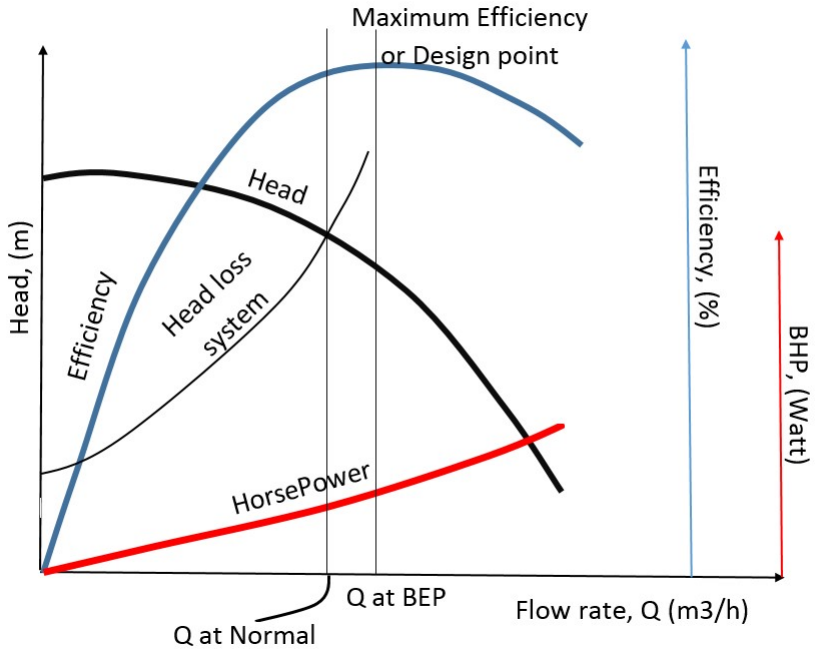

Figure 1.4: Schematic picture of general centrifugal pump. Adapted from [45]

Head and power increase if the speed of the impeller increases and the outlet diameter of the centrifugal pump impeller is larger at a certain flow rate.

Theoretically, centrifugal pump performance can be analyzed through a fixed control volume analysis. The relationship between centrifugal power and head is described in the Euler turbomachine equations as follows [45][15]

$$P_{th} = \rho.Q(u_2 v_{t2} - u_1 v_{t1}) \tag{1.1}$$

$$H_{th} = \frac{(u_2 v_{t2} - u_1 v_{t1})}{g} \tag{1.2}$$

$$Q = v_n 2\pi r b \tag{1.3}$$

The detailed description of the terms in the above equations can be seen in Table 1.1. The Euler turbomachine equation 1.1 and 1.2 above are derived from angular momentum and the velocity triangle built in the impeller inlet and outlet as seen in figure 1.6. The

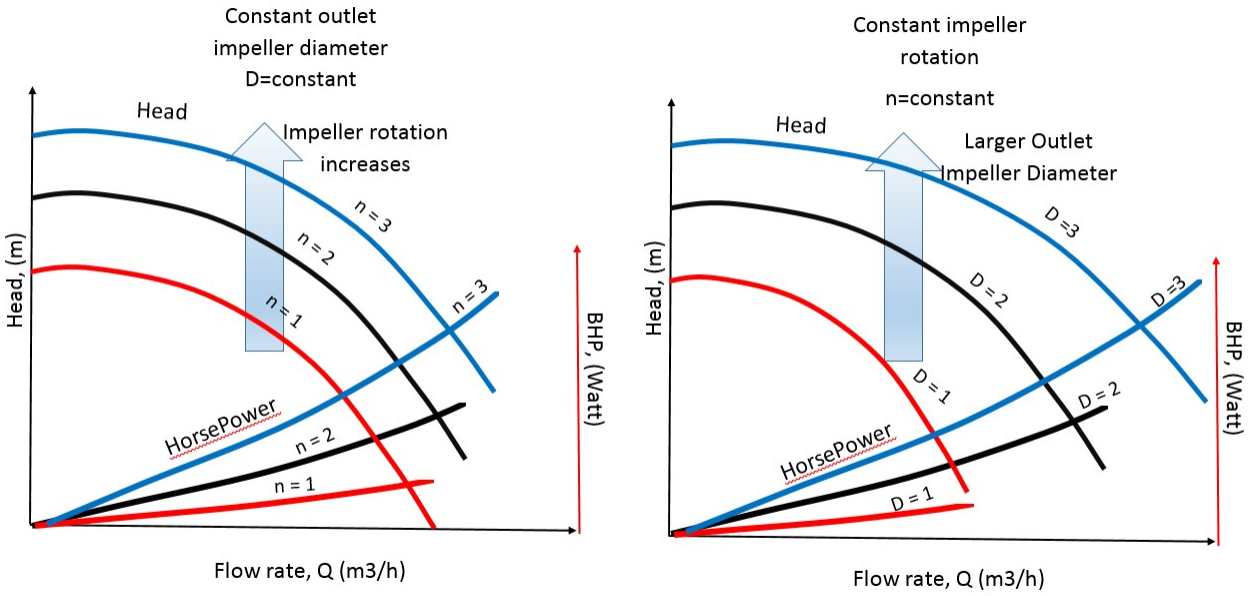

Figure 1.5: a. The centrifugal pump performance at a constant speed b. The centrifugal pump performance at a constant outlet diameter. Adapted from [45]

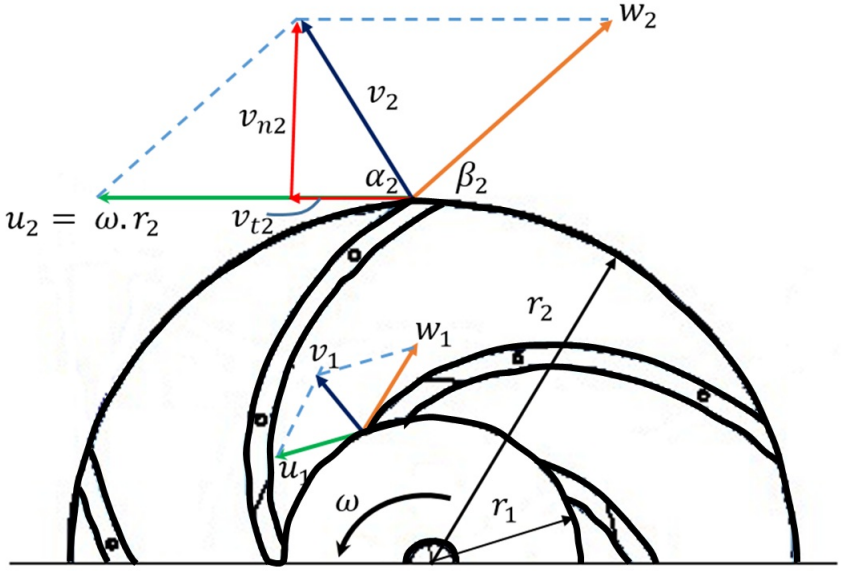

Figure 1.6: Velocity triangles at the impeller inlet and outlet of a centrifugal pump. Adapted from [45]

detailed descriptions of velocities mentioned in figure 1.6 are presented in Table 1.1. The assumption used to derive the equations above are the fluid flow is assumed ideal. Ideal fluid flow means that the fluid flows without any disturbance which might cause separation flow in the impeller, in other words, the fluid flow follows the blade curvature and there are an infinite number of blades.

Table 1.1: Descriptions of fluid velocity inside the impeller passage

P_{th}	Theoretical power of centrifugal pumps
H_{th}	Theoretical head of centrifugal pumps
v	Absolute velocity
u	Rotational velocity (u =ω.R)
W	Relative velocity
v_t	Tangential component of absolute velocity
v_n	Normal / meridional component of absolute velocity
τ	Centrifugal pump torque
α	Angle between absolute velocity ($\mathbf{v}$) and rotational velocity ($\mathbf{u}$)
β	Angle between relative velocity ($\mathbf{W}$) and negative rotational velocity ($\mathbf{u}$)

The v_n is related to the flow rate of the pump, while v_t is related to the pump torque (τ). W is the fluid velocity relative to the impeller which is always parallel to the blade angle (β) in the ideal Euler approach. In summary, ideal performance of a centrifugal pump can be obtained through the fluid and impeller velocity and impeller geometry. However, actual performance of a centrifugal pump still has to be obtained through experiment.

1.3 Dimensionless pump performance

The relation of the physical process to the pump performance is described in the dimensionless parameters of the pump. The dimensionless parameters of a turbomachine are [21]

$$Flow\ Coefficient(\Phi') = \frac{Q}{\omega D^3} \tag{1.4}$$

$$Head\ Coefficient(\Psi') = \frac{gH}{\omega^2 D^2} \tag{1.5}$$

$$Torque\ Coefficient(\mathcal{T}) = \frac{\tau}{\rho D^5 \omega^2} \tag{1.6}$$

The flow coefficient and head coefficient dimensionless relationship above can be modified so that it is more convenient to centrifugal pump analysis which involves the vector velocity analysis.

$$Flow\ Coefficient(\Phi) = \frac{v_{n2}}{u_2} \tag{1.7}$$

$$Head\ Coefficient(\Psi) = \frac{gH}{{u_2}^2} \tag{1.8}$$

Φ and Ψ are preferable when engineers design the centrifugal pump impeller. On the other hand Φ' , Ψ' and $\mathcal{T}$ are used to apply the affinity laws in turbomachines.

The other dimensionless parameter is specific speed (n_s). The specific speed is obtained by eliminating the physical parameter of the impeller diameter from influencing pump performance. The specific speed is often to be used for determining the appropriate type of centrifugal pump in the operating conditions. The specific speed of the centrifugal pump can be seen in relationship as follows

$$Specific\ Speed(n_s) = \frac{\Phi'^{\frac{1}{2}}}{\Psi'^{\frac{3}{4}}} \tag{1.9}$$

$$Specific\ Speed(n_s) = \frac{\omega Q^{\frac{1}{2}}}{(gH)^{\frac{3}{4}}} \tag{1.10}$$

The classification of the centrifugal pump based on n_s at the BEP condition can be seen in figure 1.7. From figure 1.7, it can be inferred that it is better to design an axial type pump

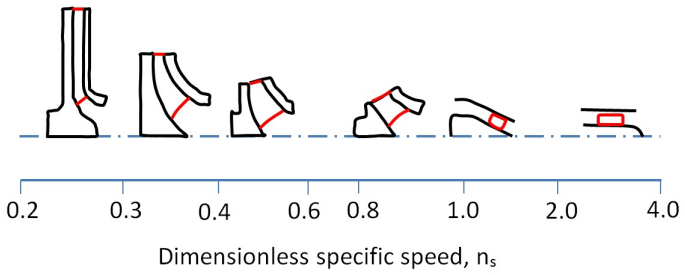

Figure 1.7: The classification of the centrifugal pump. Adapted from [15]

compared to a centrifugal pump at a higher specific speed. The high specific speed means

that the operating condition has more flow rate than the head increase. If the operating condition needs to have high pressure, the radial or centrifugal pump type should be chosen.

The next dimensionless parameter is specific diameter which is obtained by eliminating the speed physical parameter to analyze the pump performance. The relationship of the specific diameter is

$$SpecificDiameter(D_s) = \frac{\Phi'^{\frac{1}{4}}}{\Psi'^{\frac{1}{2}}} \tag{1.11}$$

$$SpecificDiameter(D_s) = \frac{D(gH)^{\frac{3}{4}}}{Q^{\frac{1}{2}}} \tag{1.12}$$

Based on past experiments, researchers plotted a graph representing the optimum efficiency of the turbomachine based on the specific diameter (D_s) and specific speed of impeller (n_s). The plot discussed is the Cordier diagram which is shown in figure 4.4. To obtain best performance of a turbomachine, designers usually refer to the Cordier diagram [21].

1.4 Centrifugal pump efficiency and losses

Similar to other machines, centrifugal pump efficiency is obtained by calculating the ratio between the input power to the output power. The output power is obtained by extracting the power from the fluid energy which is usually known as water horsepower (WHP). The input power is the torque required of the pump to deliver fluid at a certain speed and called brake horsepower (BHP). The centrifugal pump efficiency relation can be seen in equation 1.13 [45].

$$\eta = \frac{WHP}{BHP} = \frac{\rho g Q H}{\tau \omega} \tag{1.13}$$

Several losses affecting centrifugal pump efficiency are impeller circulatory flow losses, turbulence losses and friction losses [37]. The friction loss occurs as a result of the friction between the fluid and passage surfaces. The friction loss increases quadratically when the flow rate is increased since the flow inside the impeller is turbulent [45]. The circulatory flow loss is caused by the slip flow or mismatch flow between the blade and flow inside the impeller passage. At low flow rates, the slip losses are predicted to be higher compared to high flow rates [37]. Turbulence losses occur at low and high flow rates and is a minimum

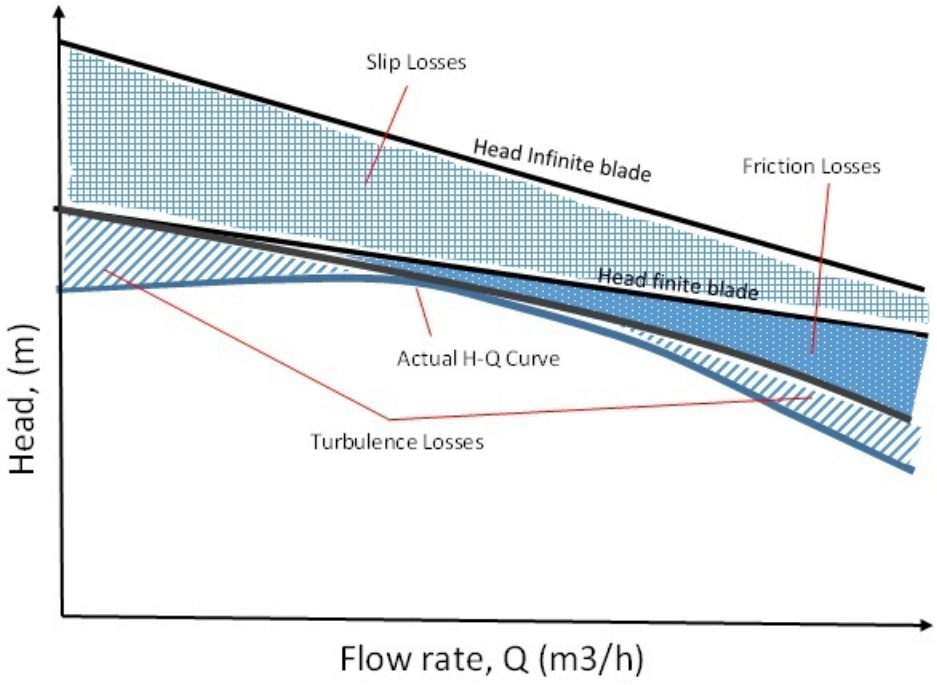

Figure 1.8: The losses occur in the centrifugal pump. Adapted from [21]

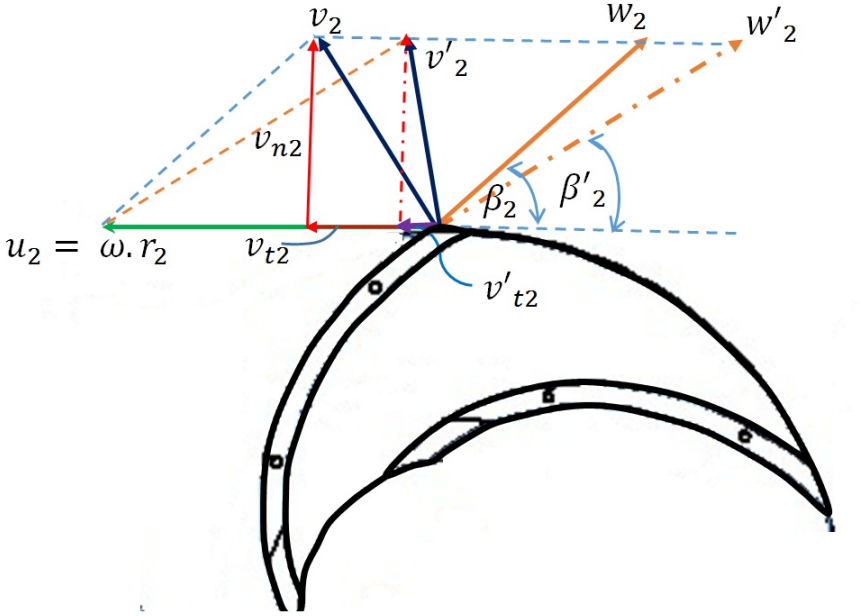

Figure 1.9: The slip model velocity triangle of the backward swept blade. Adapted from [37]

at the design flow rate. Figure 1.8 shows several losses which cause the decreasing of the centrifugal pump performance.

As mentioned previously, in an ideal flow model, flow inside a centrifugal pump follows the blade curvature, so the fluid exit at the discharge is parallel to the exit blade angle. However, past studies modeled fluid flow inside the impeller passage and noted that the outlet fluid relative velocity (W_2) is shifting and creating angle β_2' to the impeller velocity (u_2) which is known as slip (figure 1.9). The slip condition causes the normal component of the absolute velocity decreases to be v_{t2}'. Consequently, the head and power of the centrifugal pump decreases from the ideal condition. The relation between the ideal and the actual normal component of the absolute velocity is defined as the slip factor (equation 1.14) [21].

$$\sigma = \frac{v_{t2}}{v_{t2}'} \tag{1.14}$$

Several approaches have been developed to obtain the slip factor. If the slip factor is defined, it can be used to approximate the actual centrifugal pump performance from impeller geometry. One of the slip factor approaches developed by Weisner [46] is given in equation 1.15,

$$\sigma = \frac{1 - \sqrt{\sin(\beta_2)}}{Z^{0.7}} \tag{1.15}$$

where Z is the number of impeller blades. The correlation of the head and the flow coefficient with the slip factor can be derived as follows [21]

$$\Psi = \sigma - \Phi \cot(\beta_2) \tag{1.16}$$

1.5 Fluid flow inside the impeller passage

Fluid flow inside the impeller is very complex because it is generally turbulent, three-dimensional flow, highly geometry-dependent and unsteady [33]. Since centrifugal pumps are used in many applications, engineers try to determine the fluid flow inside the centrifugal pump to enhance centrifugal pump performance. It has already been mentioned that based on the Euler prediction or the one-dimensional (1D) analysis, the fluid flow follows the blade curvature from the inlet to the impeller outlet because it is assumed that the number of the blade is infinite. Then, inviscid and finite number of blades analysis was developed to predict the fluid flow inside the impeller. The analysis results showed that

the flow inside the impeller passage will not follow the blade curvature [33] [37]. The mean fluid streamline, however, bends toward the suction side close to the inlet, then it flows toward the pressure side at the exit of the impeller so the mean streamline shifts to angle β_2' (figure 1.9). The visualization of the inviscid and finite number blades analysis of the fluid inside the impeller can be seen in figure 1.10. The dotted line in figure 1.10 is the prediction of the mean fluid flow streamline for an infinite number of the blades, while the continuous line is the mean fluid flow streamline for a finite number of blades inside the impeller.

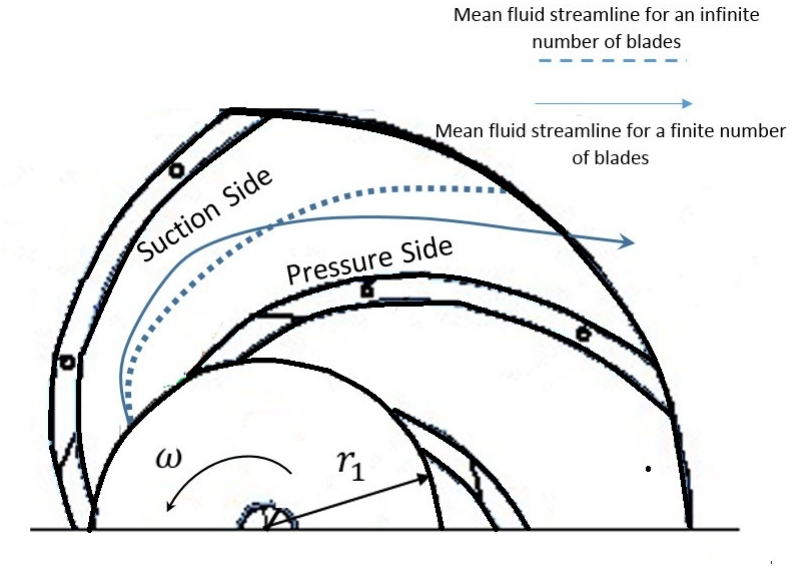

Figure 1.10: The prediction of infinite and finite number of blades flow inside the impeller. Adapted from [33]

The two-dimensional (2D) analysis of the fluid in the passage of the impeller was introduced to solve more complex fluid flow inside the rotating passage. Assuming steady and inviscid flow, the forces balance of the fluid inside the impeller are shown in figure 1.11. It can be seen on the figure that along the streamline (coordinate s), forces that influence fluid flow are inertia ($W\frac{\partial W}{\partial s}$) and centrifugal effect ($\omega^2 r\cos\beta$) as implied in equations 1.17. By comparison, across the passage (coordinate n), as implied in equation 1.18, the forces that influence the flow are centrifugal force due to streamline curvature ($\frac{W^2}{R_n}$), centrifugal ($\omega^2 r\sin\beta$) and Coriolis forces ($2\omega W\sin\sigma$) because of impeller rotation. Since the value of $sin\beta$ is very small and the value of curvature R_n is very large, increasing pressure gradient of the fluid flow across the passage (coordinate n) is dominantly caused by the fluid Coriolis

force in the impeller ($2\omega W \sin\sigma$) [33]. It also can be inferred that the pressure increases from the suction side to the pressure side across the passage . The force balance at the meridional section (equation 1.19) concludes that the pressure gradient increases from the shroud to the hub since usually the W_t is very small. It also can be said that theoretically, the relative velocity increases from the pressure side to suction side of the impeller and from the hub to the shroud of the impeller.

$$\frac{1}{\rho}\frac{\partial p}{\partial s} = -W\frac{\partial W}{\partial s} + \omega^2 r\cos\beta \tag{1.17}$$

$$\frac{1}{\rho}\frac{\partial p}{\partial n} = \frac{W^2}{R_n} - \omega^2 r\sin\beta - 2\omega W\sin\sigma \tag{1.18}$$

$$\frac{1}{\rho}\frac{\partial p}{\partial n_m} = \frac{W_t^2}{r}\cos\sigma - \frac{W^2}{R_m} \tag{1.19}$$

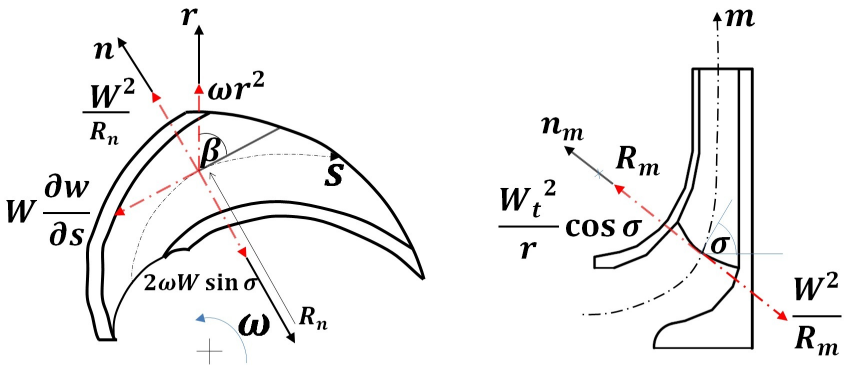

Figure 1.11: 2D inviscid forces of fluid inside the impeller passage. Adapted from [33]

2D analysis was then developed to model the potential flow of the inviscid fluid inside the impeller [33]. The potential flow of the fluid is actually a combination between the relative eddy where the fluid rotates in the entire passage of the impeller and the fluid flow toward the exit of the impeller. Figure 1.12 shows the illustration of the potential flow inside the impeller. Past study noted that the primary fluid flow, which the direction

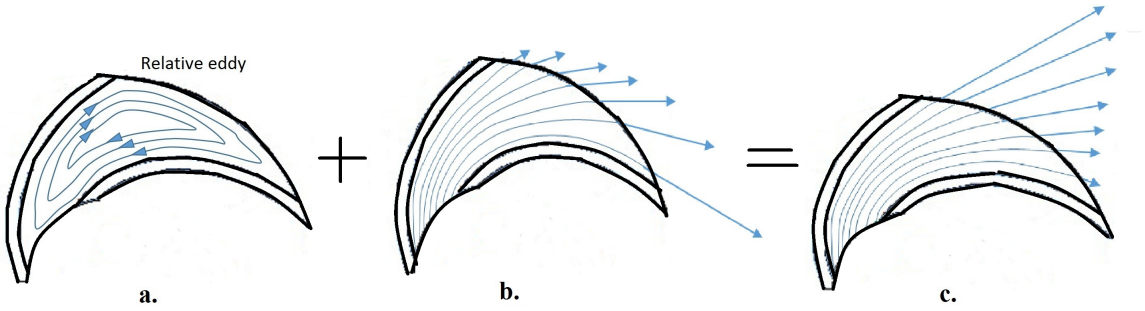

Figure 1.12: The prediction of the inviscid potential flow of fluid inside the impeller; a. the relative eddy through out the passage; b. the fluid flows inside the channel of the stationary blade; c. the sum of a and b flows. Adapted from [33]

is parallel to the passage center line of the impeller, was influenced by Coriolis effects, viscous effects, the passage geometry and the secondary flow. However the influence of the secondary flow is much less than others [1]. The secondary flow which the direction is perpendicular to the passage center line is affected more by the viscous effect. Moreover, the secondary flow affects the orientation of the vortices developed inside the impeller.

Considering a complex three dimensional flow pattern, a fluid flow model inside the passage of the rotating impeller can be divided into two regions. One region of flow which is close to the suction surface side creates a viscous low velocity wake region, whereas the other region, at the pressure surface side, the potential jet occurs at the exit of the impeller. The term for the flow at the exit of the impeller is known as "jet-wake" structure [33]. The jet-wake structure inside the impeller can be seen in figure 1.13. However, many past studies defined a wake structure is just a drop of the fluid velocity on the blade suction side instead of the back-flow that usually occurs in the wake region as shown in figure 1.13 [23][33]. Pedersen [33] mentioned that the jet-wake structure is believed to occur because the secondary flows and the boundary layer growth in the impeller cause fluid separation on the suction side of the impeller and Coriolis effect.

The jet-wake structure often can be found in the compressor impeller, but the jet-wake structure sometimes cannot be found at the exit of centrifugal pump impellers [33]. The jet-wake structure was reported to exist in the centrifugal pump experiment conducted by Hamkins and Flack [17]. They found that the fluid relative velocity that created the jet structure was higher for the shroud type impeller compared to the open type impeller [17]. Other studies that found the jet-wake structure in the centrifugal pump experiment were shown in the experiment conducted by Hajem et. al. [16], and Akhras et. al [2]. However, several studies could not find the evidence of the jet-wake structure in their

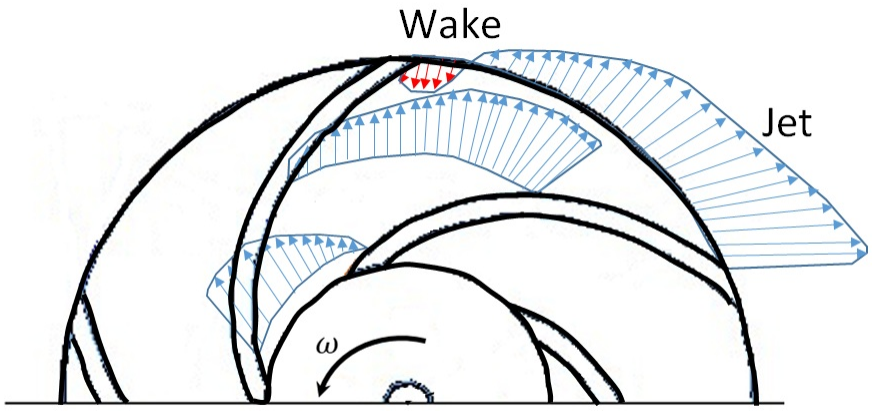

Figure 1.13: Jet-wake structure in the rotating impeller. Adapted from [33]

experiment [1][3]. Abramian and Howard [1] also mentioned that the jet-wake structure in the centrifugal pump is influenced by length and width of the impeller passage and the blade number [1].

1.6 Influence of impeller geometry on centrifugal flow behaviour

It is widely known that fluid flow inside the centrifugal pump is very complex and the geometry of the impeller has an important role in centrifugal pump performance. It can be inferred from the theoretical Euler prediction, see eq.1.2, that the head of the pump increases if the exit blade angle is larger because the larger exit blade angle causes the larger value of the tangential component of absolute velocity. Figure 1.14 shows the influence of the impeller shape on the centrifugal pump head. However, the characteristic of the centrifugal pump shown in figure 1.14 only occurs if an infinite blade number and inviscid flow are assumed. To verify the theory, many studies were conducted to investigate the influence of the impeller geometry on the centrifugal pump behavior. Past research conducted by Susanta [11] studied the effect of the blade shape on the pump performance. In the study, the author utilized performance analysis of the centrifugal pump of three different designed blade shapes which are radial, forward curved and backward curved impeller. The experiments were conducted at a constant rotational speed and a constant resistance curve. Susanta [11] found that the radial and forward curved resulted in a higher head

pressure compared to the backward curved impeller. Consequently, the water horsepower of the radial and forward curved impeller is higher than backward curved impeller. However, there was an instability in the flow at low flow rate. The instability flow is shown in a head fluctuation at low flow rates as presented in figure 1.15. The instability flow at low flow rate for the radial and forward curved design is the main reason that backward curved impeller are used in many applications in industry.

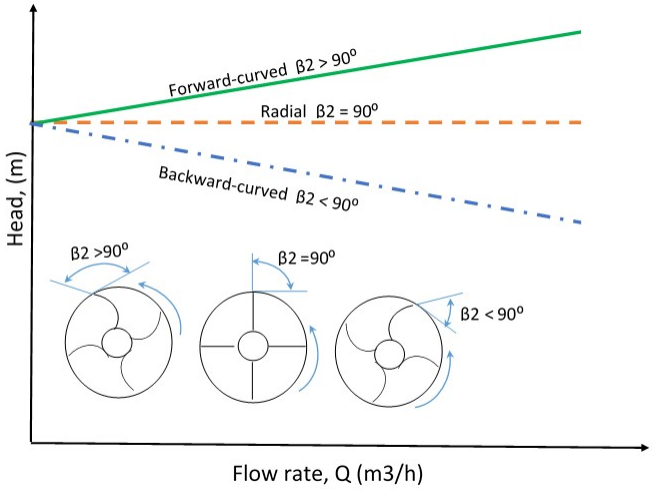

Figure 1.14: Influence of the blade shape to the theoretical head of the impeller based on Euler turbomachine equation 1.2

The blade shape discussed above actually is categorized in accordance with the exit blade angle. Many studies observed the influence of the blade exit angle on the centrifugal pump behavior particular to the backward curved impeller [27][38][4][39]. Generally, studies conducted either experimentally and numerically found that the larger exit blade angle resulted in an increasing head of the centrifugal pump. However, there was no significant relation between the efficiency and the blade exit angle. Li [27] believed that the skin friction factor of the impeller was the main reason that there was no relation between the exit blade angle with the efficiency. Fluid skin friction on the impeller surface generated part of the hydraulic losses of the pump. In low flow rate circumstances, the skin friction factor was higher for a large blade exit angle. However, at high flow rates, the skin friction was higher for the small blade exit angle. Li [26] also observed the fluid behavior of the different blade angle of impellers which can be shown in figure 1.16. For larger exit blade angle ($\beta_2 = 44^o$), fluid separation occurred even at the design flow rate, whereas at the small exit blade angle ($\beta_2 = 20^o$) separation was not seen at the design flow rate. The

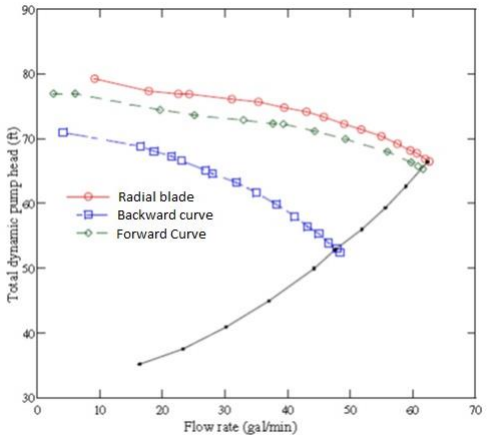

Figure 1.15: Influence of the blade shape to the pump performance [11]

study also revealed that there was pressure fluctuation when the blade was parallel to the tongue of the centrifugal pump. Therefore, there is a connection between the fluctuation pressure with the number of blades and the rotation of the impeller. Larger blade exit angle of impellers propagated more pressure and velocity head fluctuation than a smaller blade exit angle.

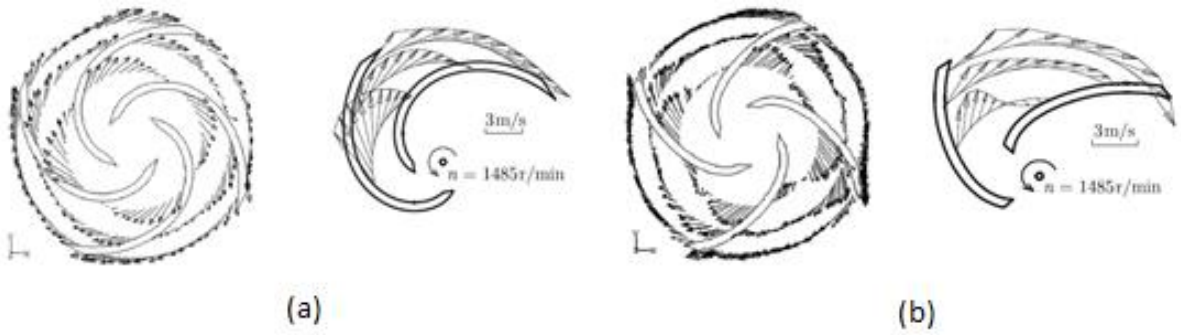

Figure 1.16: Flow structure inside the impeller (a). impeller blade exit angle (β_2) = 20^o, (b) Impeller blade exit angle (β_2) = 44^o [26]

The number of blades becomes one of the factors contributing to centrifugal pump performance. Several studies observed the influence of blade numbers on the flow structure inside the impeller and the centrifugal pump performance. An initial study about the influence of the number of blades on the pump performance has been conducted experi-

mentally by Varley [42]. The influence of the number of blades on the centrifugal pump performance can be seen in figure 1.17. It can be inferred from figure 1.17 that the more blades on the impeller, the higher head that the impeller could achieve, but there was no particular correlation between the number of blades on centrifugal pump efficiency [42]. However, based on the experiment, it can be said that the number of blades in the range of 4-8 is the peak of the centrifugal pump efficiency. Li [25] also conducted an experiment to observe the centrifugal pump performance of several impellers with different blades number and several fluid viscosities . The result was for fluid which has low viscosity, the number of blades has an important role in the centrifugal pump performance. However, when the viscosity of the pump increased, the influence on the performance became unclear.

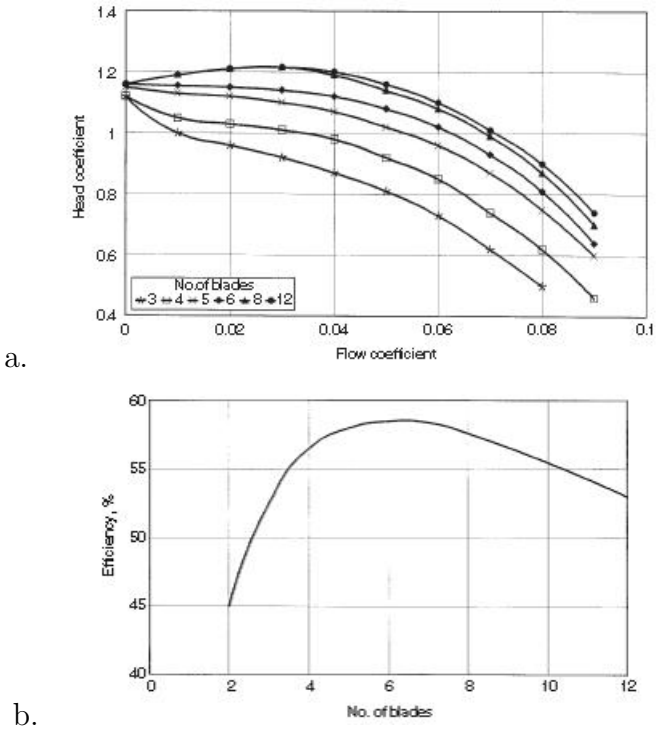

Figure 1.17: The centrifugal pump performance a. H-Q curve; b. maximum efficiency curve; as a result of changing blade numbers [37]

Murakami *et al.* [32] conducted an experiment to observe the flow structure inside the 3 and 7 blades of a centrifugal pump impeller. This experiment used a three-hole yaw probe to obtain the pressure and velocity distribution inside the impeller. Moreover, they also conducted oil visualization to verify the fluid structure obtained by the yaw probe

pressure measurement. From this experiment, they explained that the flow structure for the 7 blade impeller showed a well behaved structure at the design flow rate. Close to the inlet of the impeller, high secondary flow was observed due to flow direction change from the axial to radial flow inside the impeller. The secondary flow disappeared at the middle of the passage. It is also noticed that the radial flow was higher at the suction side of the impeller inlet, but it was higher at the blade pressure side close to impeller exit. At low flow rate, the fluid flow inside the 7 bladed impeller changed drastically compared to the design flow rate. The radial velocity close to the inlet reduced greatly, meaning that separation flow occurred at the suction side close to the impeller inlet. In addition, separation flow was also occurred at the pressure side close to the exit of the impeller. For the 3 bladed impeller, at the inlet of the impeller, there was a back flow at the blade pressure side close to the shroud at the design flow rate. Murakami *et al.* [32] explained that the back flow appeared because there was not enough blade to guide the inlet flow so the fluid at the pressure side flowed back to the inlet. At low flow rate, the flow inside the 7 bladed impeller created 3 wake regions which were on the blade suction region, blade pressure side near impeller exit and the tip of the blade suction side. By comparison, the fluid inside the 3 bladed impeller created a wake region almost half of the passage at the inlet section. The separation flow which occurred at the pressure side close to the impeller exit and suction side of the 7 bladed impeller were not appeared for the 3 bladed impeller. The velocity profile close to the impeller inlet for the 3 and 7 bladed impellers are shown in figure 1.18.

Hesse and Howard [18] conducted an experiment to observe the fluid behavior and blade loading for impellers which have 16 and 8 blades. Blade loading in the impeller is the subtraction of pressure between the pressure side and the suction side of a passage [1]. When the value of the blade loading is positive, energy is added to the fluid from the impeller rotation. The sign of positive blade loading can be seen if the relative velocity increases from the pressure side to the suction side of impeller on the normal coordinate passage of the impeller. Hesse and Howard [18] found that for the 16 bladed impeller, the fluid at the inlet followed the potential flow theory where positive blade loading occurred. However, in the middle of the passage, non-potential flow started to occur. This phenomena was reported to occur because the fluid was strongly influenced by rapidly growing boundary layer at the suction side of impeller [18]. The researches also noticed that for the 16 bladed impeller, only a large single vortex pattern of secondary flow occurred at the inlet of the impeller. As the fluid moved to the exit, the secondary flow developed to a double vortex pattern. For the 8 bladed impeller, fluid flow inside the impeller almost followed the potential flow theory because the radial velocity increased from pressure side to suction side of the impeller. The researchers also noticed that because there was not

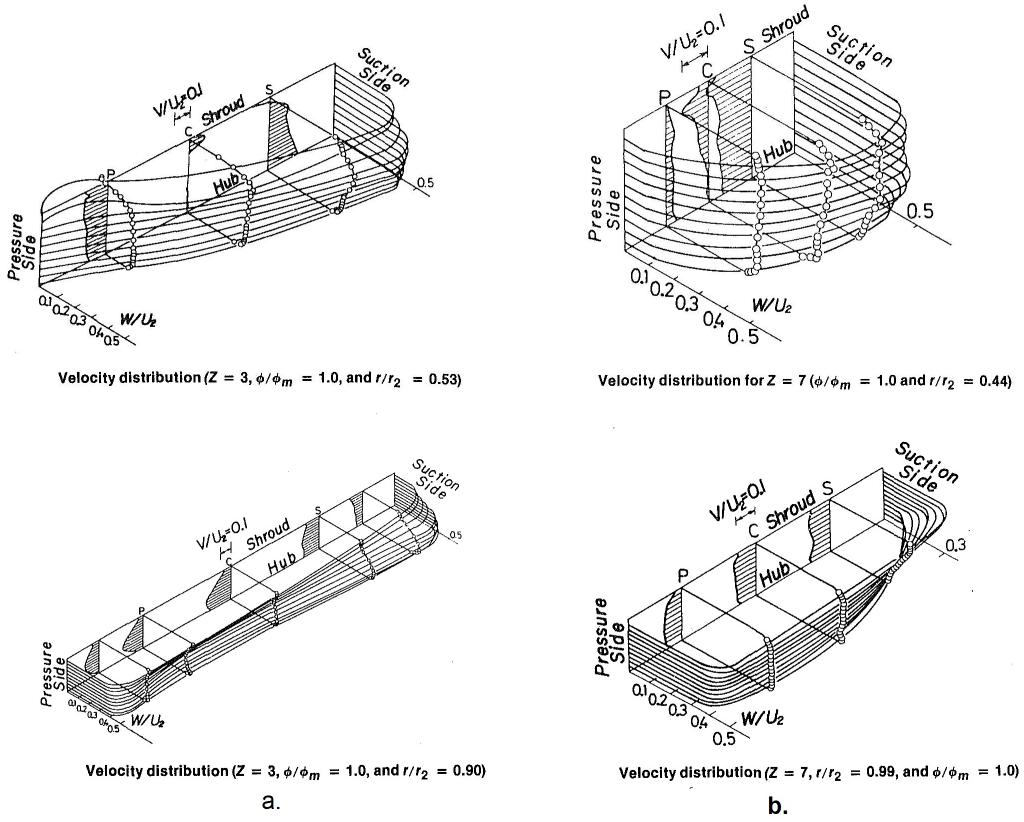

Figure 1.18: Velocity profile radial and tangential velocity near inlet (top) and outlet (bottom) of a) 3 bladed impeller and b) 7 bladed impeller [32]

enough blade to constraint flow entering the passages, the secondary flow which represented by the bulk flow occurred at the impeller inlet. The bulk secondary flow resulted in a superimposed vortex pattern at the inlet of the impeller and formed double side to side vortex. The researchers also mentioned that the turbulence intensity generally for both impellers decreased as the fluid flows to the exit of the impeller.

Researchers also used numerical modeling to observe the fluid structure of different number of blades [19][7]. Research done by Houlin *et al.* [19] confirmed that from numerical and experimental studies, head increased by increasing the number of blades on the impeller . The numerical study found that the static pressure increased if the number of blades was increased. The addition of blades, however, caused the flow in the volute to become more non uniform. Houlin *et al.* [19] also noticed that there was a jet-wake phenomenon

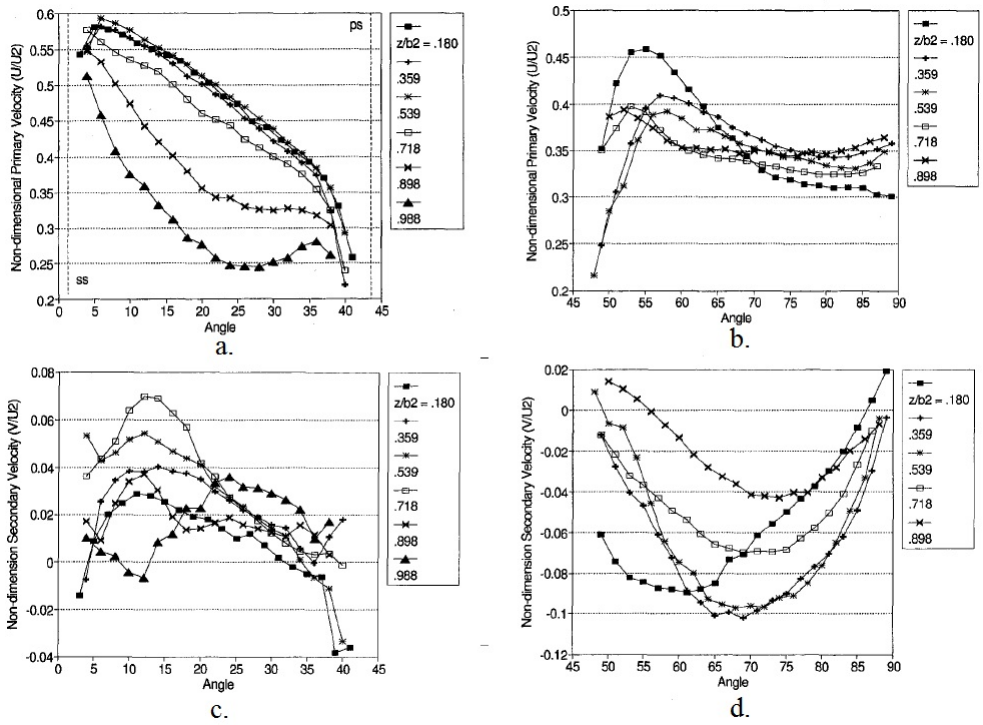

Figure 1.19: Mean normalized primary velocity (top) at: a) inlet and b) outlet and secondary velocity (bottom) at: c) inlet and d) outlet and at the design flow rate of the 8 bladed impeller obtained by Hesse and Howard [18]

for smaller number of blades but it gradually disappeared when increasing the number of blades.

1.7 Objective

Studies and experiments of pump performance and fluid behavior of a different number of blades on a centrifugal pump have been conducted by several researchers. However, their studies did not reveal the fluid structure in the entire passage of the impeller. The new methodology of measurement of fluid velocity using Particle Image Velocimetry (PIV) will allow a study of fluid behavior inside the entire passage with a different number of blades. PIV measurement will be discussed in more detail in the next section. With PIV measurements, the fluid structure can be obtained in a short time with good accuracy.

Therefore, the objective of this study is to observe the flow structure inside the impeller which has 5 and 7 backward facing curved blades using PIV measurement. The flow structure of 100% and 75% Q_d are observed to understand the flow structure of new designed impellers. Furthermore, this study also plans to understand the flow behavior of high flow rates (140 % and 120% of Q_d) and low flow rates (50 % Q_d and 25 % Q_d) of each impeller. In addition, the impeller performance parameters such as head, flow, efficiency and power are measured to understand the performance characteristic of the new design impeller. The analysis of the research is expected to improve understanding of the fluid behavior inside the impeller at different operating conditions and different number of blades.

Chapter 2

Particle Image Velocimetry

2.1 Introduction

Particle Image Velocimetry (PIV) is a laser based measurement technique which can obtain two or three component velocities in a plane [35]. The basic principle of PIV measurement is measuring the velocity of seeding particles by tracking the particle's movement to obtain the particles displacement over a certain time. Hence, PIV measurement requires a device to record the image of particle movement. A pulsed laser is used to freeze the particles so that a camera can record the particle location in a plane. A laser is used because it is coherent, collimated, concentrated, monochromatic and high energy [35]. PIV is known as a small-intervention velocity component measurement techniques in the flow. The only intervention is the seeding particles which are inserted to the flow.

The typical set up of the PIV measurement is shown in figure 2.1. A laser beam is emitted through a cylindrical optic lens to form a laser sheet. A CCD or CMOS camera is used to capture an image of illuminated particles. Figure 2.2 is an example image captured by a camera. The red dots are the particles at a specific time, t (first capture), whereas the blue dots are the particles at $t + \Delta$ t (second capture). It can be concluded that the fluid particles are captured in the interval time (Δt) and the particles have moved some distance (Δs). The velocity is then defined as the actual particle displacement divided by the interval time (Δs/Δt). The image particle distance is corrected by multiplying by the image scale factor (M) so that the actual particle velocity (V) is defined as:

$$V = M(\frac{\Delta S}{\Delta t}) \tag{2.1}$$

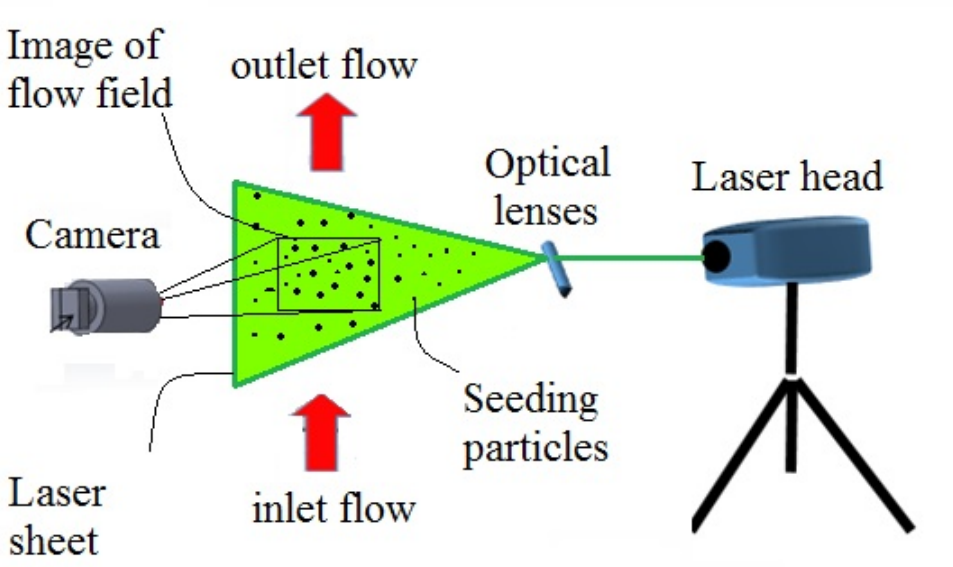

Figure 2.1: General set up of the PIV measurement. Adapted from [3]

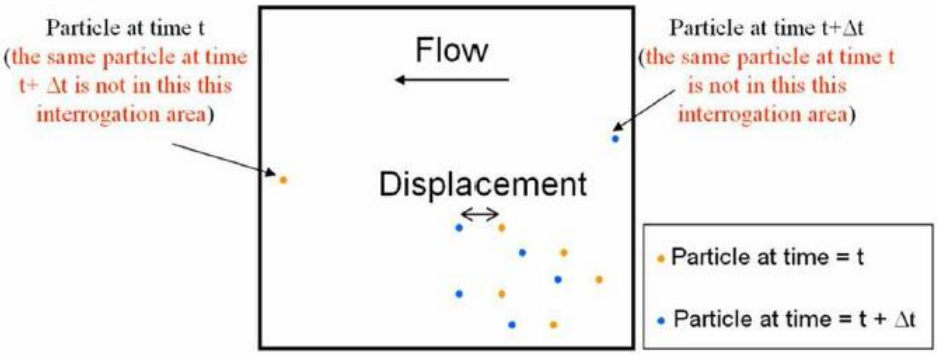

Figure 2.2: Particles shown in the plane or Image of flow field. Adapted from [3]

The PIV measurement is based on several process steps which are

- Tracer Particle Seeding
- Laser Illumination
- Recording the Image
- Synchronization and Image Processing
- Validation

The steps will be discussed in more detail later in this section.

2.2 Traced particle seeding

Particles used for fluid flow marking should be chosen properly. To obtain accurate fluid structure results, the particles should have similar movement to the fluid flow. The relative Reynolds number of the particle in the flow is defined in equation 2.2,

$$Re_p = \left(\frac{\rho_f \left| V_f - V_p \right| d_p}{\mu_f} \right) \tag{2.2}$$

where V_f is the fluid velocity, V_p is the particle velocity, ρ_f is the fluid density, d_p is the particle diameter and μ_f is the absolute fluid viscosity. $|V_f - V_p|$ is defined as the particle slip velocity. Since the particles are supposed to have a similar motion to the fluid, the slip velocity is hopefully very small.

To understand more detail about the physical properties of the particles which affect the fluid motion, first assume the particle is spherical and the $Re_p << 1$. Then, it can be assumed that the drag dominates other forces. For $Re_p << 1$, the drag force is only due to the stokes drag (see equation 2.5).

$$Dragforcesphere(\overrightarrow{F_D}) = DragForceStokes(\overrightarrow{F_D}) \tag{2.3}$$

$$3\pi\mu_f \left| V_f - V_p \right| d_p = \frac{\pi}{6}\rho_p d_p^3 \frac{d\overrightarrow{V_p}}{dt} \tag{2.4}$$

$$\frac{\rho_p d_p^2}{18\mu_f}\frac{dV_p}{dt} + V_p = V_f \tag{2.5}$$

From equation 2.5 it can be concluded that if there is a step change in the fluid velocity, it effects a time delay in particle response [35]. The time delay is given by the relaxation time or the response time correlation $\tau = \frac{\rho_p d_p^2}{18\mu_f}$. Therefore, to prevent a long time delay, it is necessary to choose small diameter particles (d_p) to be inserted in the flow. Smaller diameter particles will follow the flow well. Measuring turbulence and constant change of velocity using particle tracking requires very small particles so that the turbulence flow characteristic can be captured as shown in figure 2.3.

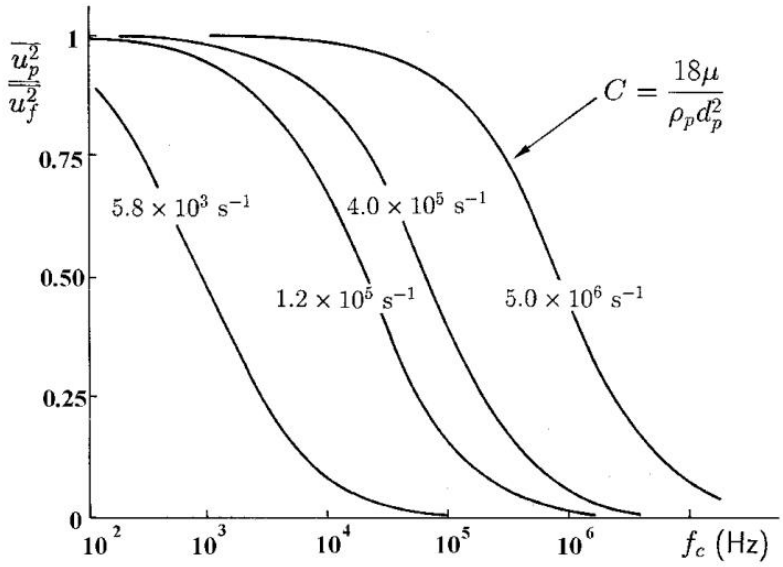

Figure 2.3: Seeding particle response in turbulent flow. Adapted from [29]

Although it is said that small particles are best for turbulent flow, small particles also have limitations when involved in PIV measurements; the smaller particle is more difficult for the camera to capture the particle. The difficulty to record small particles is caused by the reduction light scattering. Many researchers have noted that the light scattering of the particles is influenced by the particle size and shape and the orientation of the light [36]. Rayleigh scattering occurs when the light collides with a very small particle ($d_p < \frac{\lambda}{15}$) whereas Mie scattering occurs when light collides with a large particle (1-10 μm). It can be seen in figure 2.4 that the larger particle has the higher light intensity with Mie scattering. To achieve maximum light intensity, the light detector must be located away from the incident light and particle.

It is also noted that the index of refraction of the particles to the surrounding medium

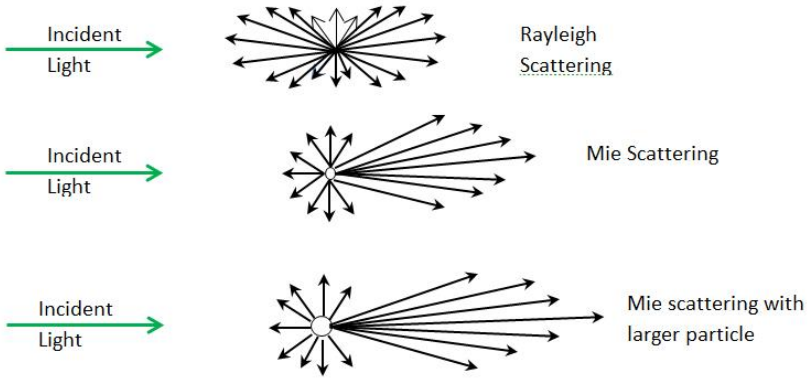

Figure 2.4: Rayleigh scattering and mie scattering light of particle. Adapted from [35]

affects the light scattering. The light scattering capability of the tracer particles is influenced by both the total scattered power (P_s) and the laser intensity (I_0) at the scattering cross section (C_s) [29]. Figure 2.5 shows that the scattering cross section is wider if the particle size is larger. Therefore, the particle size should be chosen as small as possible for low velocity and turbulent flow, but still large enough to have good light scattering characteristics.

Another consideration in choosing the particles is the buoyancy effect of the particles in the flow. It requires that the particles behavior is similar to the fluid meaning that the particles neither sink nor float. Similar assumptions to derive the drag force in equation 2.5 are also used to derive the buoyancy effect to the particle in the flow as seen in equations 2.6 -2.8.

$$\textit{Buoyancy Force Sphere}(\overrightarrow{F_{bouyant}}) = \textit{Drag Force Sphere}(\overrightarrow{F_D}) \tag{2.6}$$

$$\frac{\pi}{6}\left(\rho_p - \rho_f\right) d_p^2 g = 3\pi\mu_f \left|V_f - V_p\right| d_p \tag{2.7}$$

$$\textit{Fluid particle velocity due to gravity}(|V_f - V_p|) = (\frac{\rho_p - \rho_f)d_p^3}{18\mu_f} g \tag{2.8}$$

From equation 2.8 it can be concluded that the particles will follow the fluid flow ($|V_f - V_p| = 0$), if the ρ_f and ρ_p are equal. It means that the particle used in the PIV measurement should be neutrally buoyant within the fluid medium. In summary, PIV measurement results will be more accurate if the particles are small and have neutrally buoyant characteristic to the fluid. In this study, Pliolite VT particles in water were used. The particles is

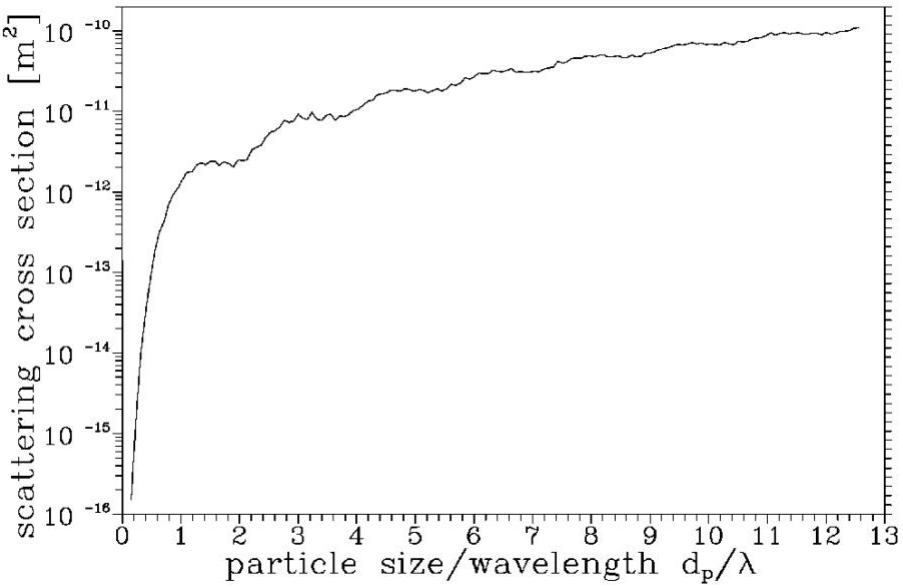

Figure 2.5: Effect of particle diameter on the light scattering in the flow. Adapted from [29]

good neutrally buoyant characteristics with water. More detailed about size and quantity of particles will be discussed in Chapter 3.

2.3 Illumination Step

As mentioned before, a laser is chosen for PIV measurement because this light is coherent, collimated, concentrated, monochromatic and has high energy characteristics. Nd:YAG lasers can generally produce laser energy from 100 - 400 mJ/pulse and with a pulse width of 5 ns. Usually the wavelength of the Nd:Yag laser is halved from (λ) 1064 nm to 532 nm by frequency doubling. This laser is good enough for measuring turbulent velocities because with 2 lasers in one unit, this system can give very fast repetition pulse rate. Because Nd:YAG lasers in pairs can produce a fast repetition rate and high enough energy to illuminate the particles so that The laser is suitable for this study.

A typical layout of the double cavity laser is shown in figure 2.6. The pulse time of the first and second cavities is controlled by the Q-switch so that it can pulse alternately and keep the high power output of the light beam. The time between pulses must be set

appropriately to the flow velocity. The typical timing diagram is presented in figure 2.7. Initially, the camera opens the shutter. After an interval of a few micro seconds, the first laser is pulsed to freeze the particle in the flow. Afterwards, the camera shuts the shutter and then it opens again instantaneously. The second laser is pulsed to obtain the second image in the interval time which is controlled in accordance with the flow velocity.

In conclusion the particle illumination process should consider several points. First, the single laser pulse duration should be short enough so that it can 'freeze' the particles properly during illumination. Secondly, the time between pulses must be controlled precisely so that it can trace the particle appropriately. Lastly, the intensity of the laser must be high enough to create a good scattered light the particle.

2.4 Recording the image

For conventional 2D PIV measurements, a camera is used to record two images consisting of illuminated particles. From both images, the displacement of the particles can be processed to get the velocity vector of the flow. The camera which is usually used in the PIV measurement is a Charge Couple Device camera (CCD) or Complementary Metal-oxide-semiconductor (CMOS). Both of the cameras have the capability to capture many images in a short interval.

It should be noted that to get good velocity data, the existence of the particles in the image should be dense enough. However, a high density of particles in the image makes it more difficult to process individual velocities. Therefore, in order to process the dense particle images, the area of the image is divided into several interrogation areas (IA). Usually the interrogation region can be 16 x 16 pixels, 32 x 32 pixels or 64 x 64 pixels. The image captured from CCD and CMOS camera is comprised of arrays of pixels. It is also noted that the smaller interrogation regions means better spatial resolution, but the total error will increase. The better spatial resolution means that velocity vectors resulting from particle images are more detailed. Choosing the interrogation region also depends on the relative flow velocity. The error of the PIV measurement will be discussed later.

2.5 Post-Processing

To process the image to obtain velocity data, many techniques can be used. The autocorrelation is one PIV technique to obtain the particle displacement that was developed when

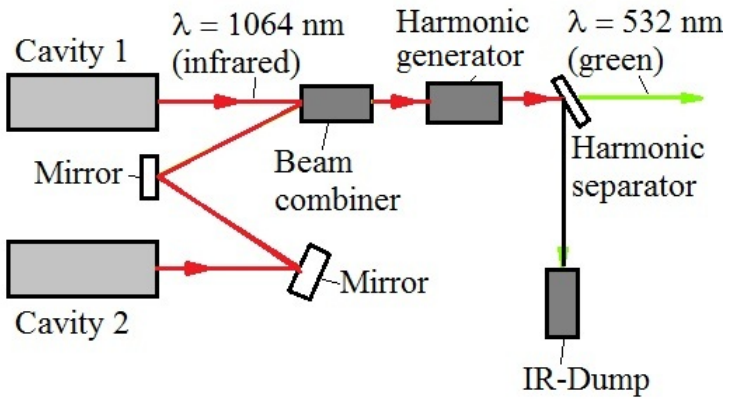

Figure 2.6: General layout of the double cavity Nd:YAG laser configuration. Adapted from [40]

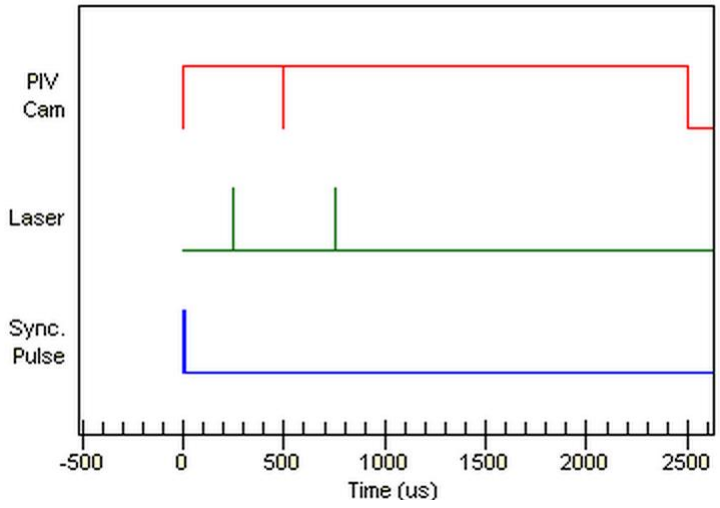

Figure 2.7: Typical timing diagram of PIV measurement. Adapted from [35]

camera technology was not able to store images very fast. More detail about this method can be seen in the pump research paper published by Dong *et al.* [12]. The other technique that can be used is the cross-correlation technique. The peak displacement in a correlation plane of each interrogation area for this method is obtained using cross correlation function that is presented in equation 2.9 [35][33].

$$R(m,n) = \sum_{i=1}^{M-m} \sum_{j=1}^{N-n} I_1(i,j) \quad I_2(1+m, j+n) \tag{2.9}$$

Where M is the vertical pixel width of the interrogation region, N is the horizontal width of the interrogation region, m is the vertical pixel width, n is the horizontal pixel width, i and j is the first and second image. Many researchers use 50% overlap to process the cross correlation to obtain optimum results.

In this study, analysis used the adaptive PIV method. This method can select the appropriate size and shape of interrogation area (IA) based on particle images and flow velocity gradient [40]. The method calculates the IA iteratively and select the size in the range pixel size that is determined. The method also gives an option to apply window functions and frequency filtering which are performed using Fast Fourier Transforms (FFT). In addition, adaptive PIV allows velocity validation. Validation of the vector will be discussed in more detail later.

2.6 Validation

In the present thesis, validation is considered to be part of a calibration process. Thus, the purpose of validation in the PIV measurement is to obtain higher quality velocity data. The basic principle of validation is to remove or replace the spurious vectors which usually do not represent the fluid movement by other vectors based on the validation technique used. There are 3 validation methods which can be found in the Dantec Studio Software [40] software which are peak, moving average and velocity range validation.

The peak validation is a method that validates the spurious vectors based on the peak height of the particle displacement in the correlation plane. In this method, users can set the lowest acceptable value of peak height, peak height ratio and S/N ratio [40]. As a result, the outlier vectors and the noise peak existing in the correlation plane will be removed. The area that contains the removed vector will be replaced with zero or will be left empty. The zero replacement vector might be given more inaccurate result than the actual result.

Therefore, it is required to consider a method to compare the neighboring vectors using the universal outliers detection algorithm to obtain a good result. The principal purpose of the algorithm is substituting the vectors which are very different from their surroundings by the median vector of vectors close to the replacement area. The software gives users the option to whether the spurious vector is just removed or the vector is removed and replaced by the calculated vector.

The moving average validation is a method which validates the spurious vectors in the defined vector maps by comparing each neighbor vector. In this method, users must first set the acceptance factor which is a parameter to determine the spurious vectors in the averaging area. The spurious vector is replaced by a reasonable estimated vector resulting from an interpolation which is calculated by conducting some iterations.

Lastly, velocity range validation is a method that can validate the spurious vectors by defining a reasonable velocity in the vector maps. In this method, users can define the maximum and minimum velocity in the vector maps. The prediction of a spurious vector which has a value outside the range will be eliminated.

2.7 Error in PIV

Measurement error is the deviation between the measurement value and the actual value. There are 2 kind of errors in the measurement which are precision error and bias error. Precision error is usually known as random error because this error cannot be entirely controlled by the experiment system. Precision error is defined as the difference between the individual and mean of a measurement value. In comparison, bias error is the difference between the mean and the actual value of the measurements. Precision error always occurs in each measurement but it lacks repeatability. In contrast, bias error is a repeatable, fixed and systematic error which occurs in the measurements. The actual value of a measurement is unknown, so uncertainty measurements which quantify the probability error in the sample mean are introduced. In this section, the possible errors which contribute to the uncertainty in the PIV measurement especially in centrifugal pump applications will be discussed.

The particles which are used as fluid markers have an important role in the PIV measurement. It is said that the particle size should be chosen so that it follows the flow movement and can be captured by the camera. Error which is caused by too small particle size is called pixel locking error. Past research has shown that if the particle has a minimum diameter of about 1-2 pixels it can reduce the pixel locking error [41]. Another error

associated with the particles is error due to too few particles in the interrogation area; this error is usually known as the peak locking error. However, if there are too many particles in the interrogation area, the particles can overlap in the interrogation area which also causes error. Past research has shown that 8 particles in the interrogation area will keep the uncertainty to about 1 % when using the auto-correlation method [12][13]. The Dantec dynamic manual [40] notes that the 'rule of thumb' for particles in the interrogation area is 8-10 particles. Other research noticed that 8 particles in each interrogation area will result in less than a 4% error [3].

It is also evident that seeded particles must be bright enough to obtain a good quality image. Moreover, the contrast between particles and the background must be high enough because the light reflection from the background can add noise at which can result in error. The ratio of the brightness of the particles to the brightness of the background is defined as the signal to noise ratio (SNR). The noise can be reduced by reducing the light intensity of the environment and increasing the contrast between the particle and the background. In the validation steps which have already been discussed before, the user can set the SNR ratio so that it can remove the background noise.

Since the PIV measurement records the fluid motion in the interrogation area, the particles are expected to be captured in both of the image pairs. However, sometimes the fluid does not flow parallel to the light sheet and this causes the particles to move out of the plane when collecting data. The loss of particles due to out of plane motion can cause measurement error. The loss of a particle can also be caused by the inappropriate laser pulsation interval which should be set based on the flow velocity. Particles that move perpendicular to the light sheet in the measurement volume result in the particles seeming to not be moving can also cause error. This error is known as parallax error. Past study noted that this error can be reduced when a two dimensional designed impeller is used [24].

PIV measurements only obtain the velocity of the fluid flow within a given period of time. Hence, the acceleration of the fluid during the collecting of data in the interval time cannot be resolved, meaning that the flow acceleration does not appear in the velocity results. This error is known as acceleration error. In addition, PIV measurements only count the average velocity at a certain interrogation area. Therefore, if there is a velocity gradient in the interrogation area, the PIV measurement will neglect it. The error discussed is known as the velocity gradient error. The velocity gradient error can be reduced by reducing the size of the interrogation area.

Error associated with the recording step is known as recording error. One of the examples of this error is caused by a camera that cannot capture uniform light intensity

is categorized in this error. Another recording error also can be caused by the error when quantifying the discrete value of light intensity.

In summary, error in PIV measurements cannot be eliminated, but it can be reduced by using a good size and quantity of particles and conducting the measurements as procedure. Therefore, uncertainty of the measurements can be kept in low level. Uncertainty is discussed in more detail in Appendix A.

2.8 PIV measurements of the fluid inside a centrifugal pump impeller

PIV technology was introduced in the 1980s [12]. Then, researchers brought PIV technology to use as a quantitative visualization technique in centrifugal pump experiments. Dong *et al.* [12][13] were the leaders that adapted the PIV technology to conduct an experiment in a centrifugal pump which focused on the flow characteristic within the volute of the centrifugal pump. At that time, the technology of PIV had not been established yet, so to conduct the PIV measurements, they used a video recording camera instead of a CCD or CMOS camera. This study used a Nd:YAG laser to illuminate the particles. Auto correlation was used to determine the peak of the particle displacement in the correlation plane. Figure 2.8 shows an example of particles displacement peak of fluid flow in the volute for one of their interrogation region. In order to verify the visualization result of the flow in the centrifugal pump, Dong *et al.* [12] referred to the laser velocimeter result of an experiment conducted by Miner *et al.* [31]. The results of the PIV experiment showed agreement with the laser velocimeter experiment. The value of tangential velocity fluctuated at the point close to the impeller and the fluctuation disipated when the measurements were conducted further from the impeller. Furthermore, the result showed that the value of tangential velocity in the center of the volute dropped as the flow rate decreased. Further observation was conducted inside the impeller. The result showed that the value of velocity in the radial direction was low at the suction side of the impeller exit and and it increased as the point of observation moved to the pressure side, indicating the jet-wake pattern occurred at the exit of the impeller.

Pedersen *et al.* [33] [34] conducted research to compare the fluid flow behavior obtained by LDV to the PIV results inside the centrifugal impeller. The study used a six bladed backward curve impeller. The result showed that a well behaved flow structure in the impeller passages at the design condition. However, only the inlet region which about two thirds of the passage agreed with the potential flow theory. The failure to follow potential

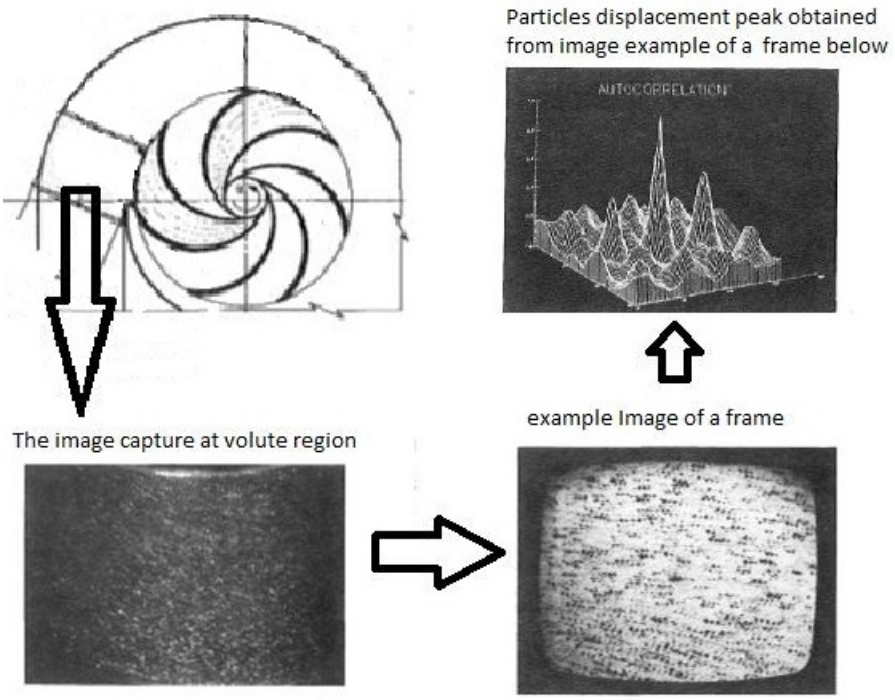

Figure 2.8: The example of particles displacement peak obtained by cross correlation [12][13]

flow was caused by the Coriolis force which pushed the fluid from the blade suction side to the blade pressure side. The Coriolis effect increased as the fluid moved toward the impeller exit. Hence, close to the impeller outlet, the relative velocity increased toward the pressure side. At the quarter of design flow rate, the stalled and unstalled passages known as two-channel phenomenon was shown in the flow structure obtained by both PIV and LDV measurements. The stalled passage contained the fluid that blocked the passage while the unstalled passage contained a well behaved fluid structure like the fluid structure at the design flow rate. The two-channel phenomenon was reported to be steady and non rotating because the even number of blades which is shown in figure 2.9b. The relative velocity obtained at the design flow rate and off design flow rate was shown in figure 2.9. The results also presented the fluid angle deviation (β_d) that was obtained using equation 3.20. At the design flow rate, a high positive value of fluid angle deviation was shown at the impeller inlet which was a sign of an existence of swirl component generated by impeller rotation. In addition, a zero contour line which was a separation line between the ineffective slip region (inner part) and effective slip region (outer part) was presented. The

inner part region was called the 'true channel' region. Furthermore, the velocity fluctuation that was represented by turbulence kinetic energy (TKE) was high near the blade suction surface where the high velocity was located.

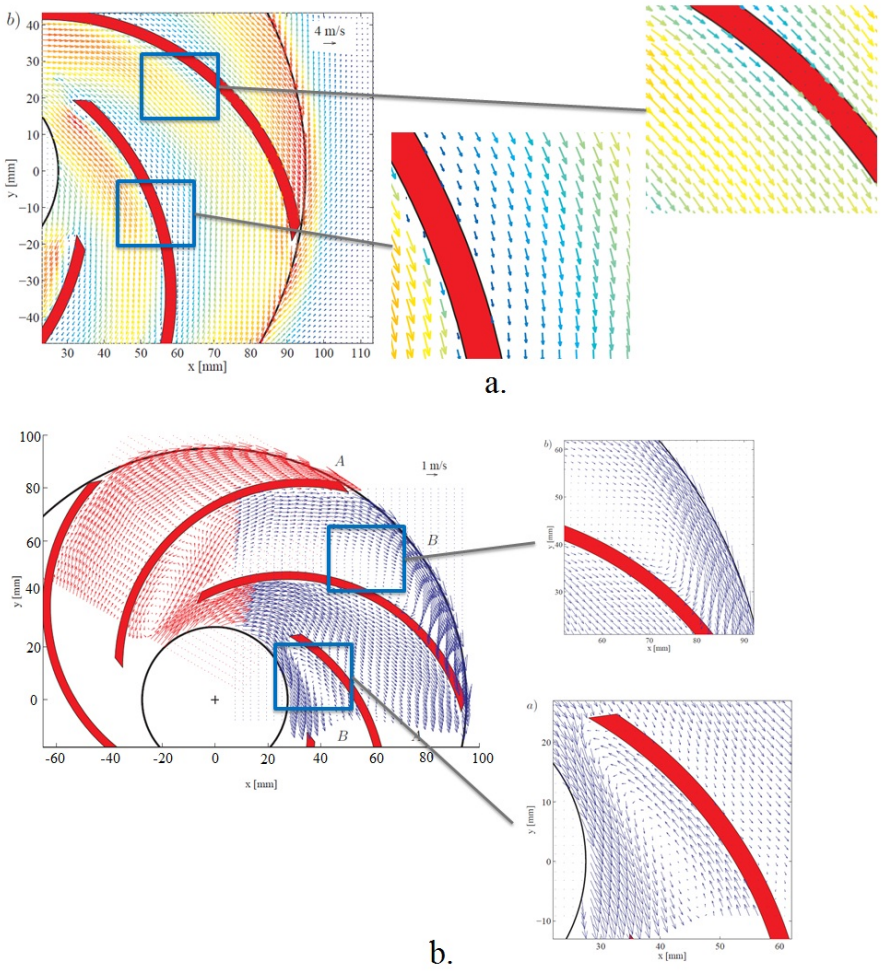

Figure 2.9: Vector maps of relative velocity fluid inside the passages of a centrifugal pump impeller from Pedersen [33] a). at the design flow Q/Qd b). at 0.25 Q/Qd

Altaf [3] conducted research to observe the fluid behavior inside the centrifugal pump impeller at several flow rates using PIV measurements. An 8 bladed backward curved impeller with an outside diameter of 496 mm was built to conduct the experiment. Two regions of fluid flow in the inlet and outlet were observed. The results showed that at

the design flow rate, the fluid structure inside the impeller established a well behaved flow with no separation. Moreover, unlike the results obtained by Pedersen, along the impeller passage, the flow followed the potential flow theory. the primary relative velocity component increased from the pressure side to suction side. The separation flow started to occur at 50% flow rate which blocked a small part region of the passage. The stalled passage was established at 30% and 25% of design flow rate which blocked the whole passage. The two-channel phenomenon or stalled and unstalled between passages was not clearly shown in the experiment. This study also presented fluid turbulence intensity (TI) which was normalized fluid fluctuation with local fluid velocity. The results noted that the high TI contour which was proposed as the fluid separation region was started on the blade suction side then it moved to the mid passage when the flow rate was decreased from the design flow rate. The other results also showed that there was high fluid angle deviation (β_d) at the impeller inlet because the flow was influenced by bulk flow.

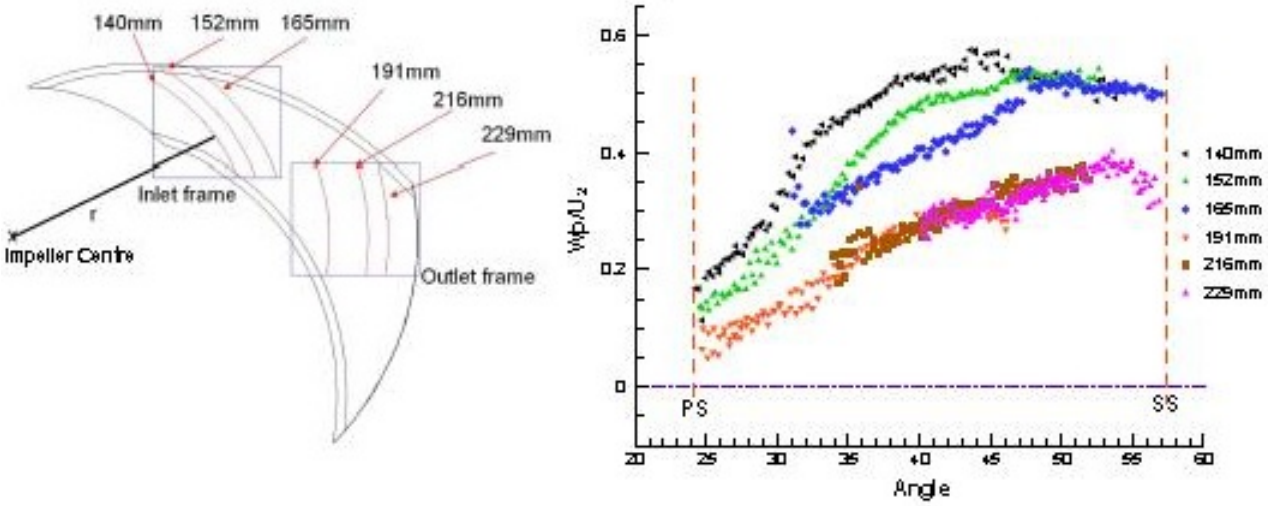

Figure 2.10: The field of fiew of PIV measurement in passage of impeller and the mean primary velocity along the passage of the impeller showing no jet-wake pattern at the design flow rate [3]

Study of the internal flow in a low specific speed impeller was also conducted by Cui and Dong [10]. They investigated the internal flow of low specific speed pump in the z direction (along the width of the impeller) and at several flow rates. The images were captured at 6 different angular positions. One result of this research showed that when the blade was aligned with the tongue, low velocity appeared in the blade suction side of the impeller passage and slowly dissipated when the passage moved further from the tongue.

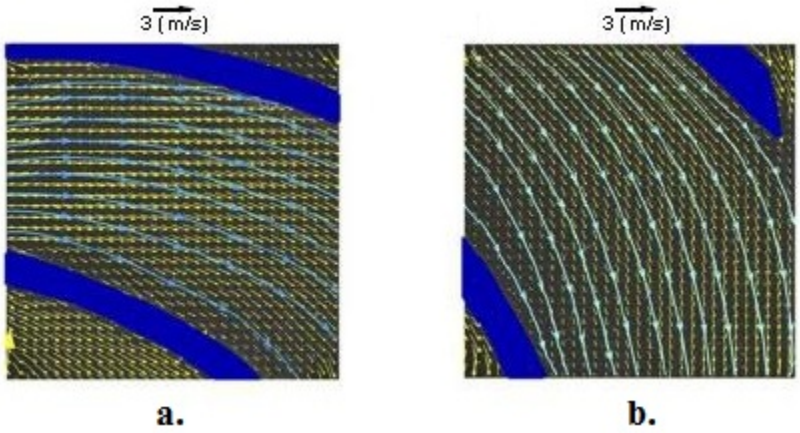

Figure 2.11: The streamlines of fluid flow inside the channel of impeller at the design flow rate of a. Inlet region and b. Outlet region from [3]

The results also showed that when the flow rate was increased, the relative velocity near the blade pressure side increased, but close to blade suction side, it decreased. At high flow rates, 1.2-1.4 Q_d, a jet-wake pattern was found at the outlet of the impeller when the passage passed through the tongue. It could be seen from the curve of relative velocity that it decreased from the suction side reaching a minimum value before increasing at the pressure side of the impeller. The other results were along the impeller width, the relative velocity increased from the shroud to the hub. The minimum value shifted toward blade suction side.

Westra *et al.* [44] conducted experiments and numerical studies to understand the secondary flow inside the centrifugal impeller pump passages using PIV measurements. In order to model the secondary flow inside the passages of the impeller, they measured the velocity of the fluid across the passages. The measurements were conducted at a position close to the hub and close to the shroud. The measurements were conducted at 80%, 100% and 120% flow rate. The results showed that the CFD and experiment results showed agreement at the design and close to the design flow rates. The results of magnitude of relative velocity (W/u_2) revealed that the relative velocity increased when the flow rate was increased. In addition, when the fluid moved toward the impeller outlet, the relative velocity increased near the suction side, but then it decreased near the pressure side. At the position close to the hub, the fluid behavior along the passages confirmed potential flow theory; the relative velocity increased from the pressure side to the suction side of the blades as shown in figure 2.12a. However, at the position close to the shroud, the potential flow patterns started to change at the middle of the passage because of viscous effects. At

the exit of the passage, fluid flow at the shroud created a jet-wake pattern. Westra [43] also observed the absolute fluid angle (β_r) of fluid flow that is defined in equation 3.19 near the hub and shroud numerically and experimentally. The results showed that the magnitude of the flow angle that resulted from PIV measurements was smaller than the computed results. It indicated that actually, the fluid tended to move toward the pressure side as a result of the existence of wake at the exit of blades suction side.

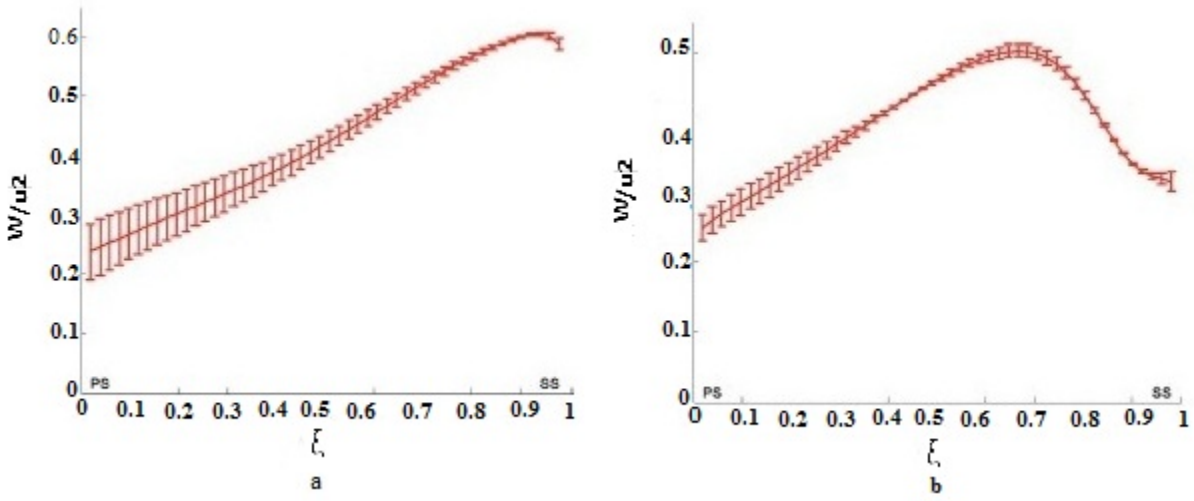

Figure 2.12: Dimensionless average relative velocity (W/u_2) inside the impeller at the design flow rate and r/R2= 0.8 a.) At Hub b.) At Shroud [44]; ξ pressure to suction side

Keller *et al.* [24] using PIV measurements observed a flow structure and a dynamic interaction of the unsteady flow at the gap between the tongue and the impeller which strongly caused the harmonic blade-passing frequency at a high flow rate. The study noticed that the bias error was reduced because the particles diameter were large and dense enough so that the pixel and peak locking effects could be neglected. In addition, the impeller was designed using two dimensional approach which helped to reduce the out of plane movement so it reduced measurement error. The research found that at high flow rates, the impeller flow outlet created a jet-wake pattern. At high flow rates, the fluid in the passage of the impeller tended to flow toward the exit duct instead of flowing through the volute as shown in figure 2.13. The Turbulence Kinetic Energy (TKE) was high at the middle of the impeller channel and formed an elliptical pattern. This confirmed that the flow separated from the pressure side of the inlet impeller. The magnified field of view results showed that the highest value of TKE was on the trailing edge of the blade and

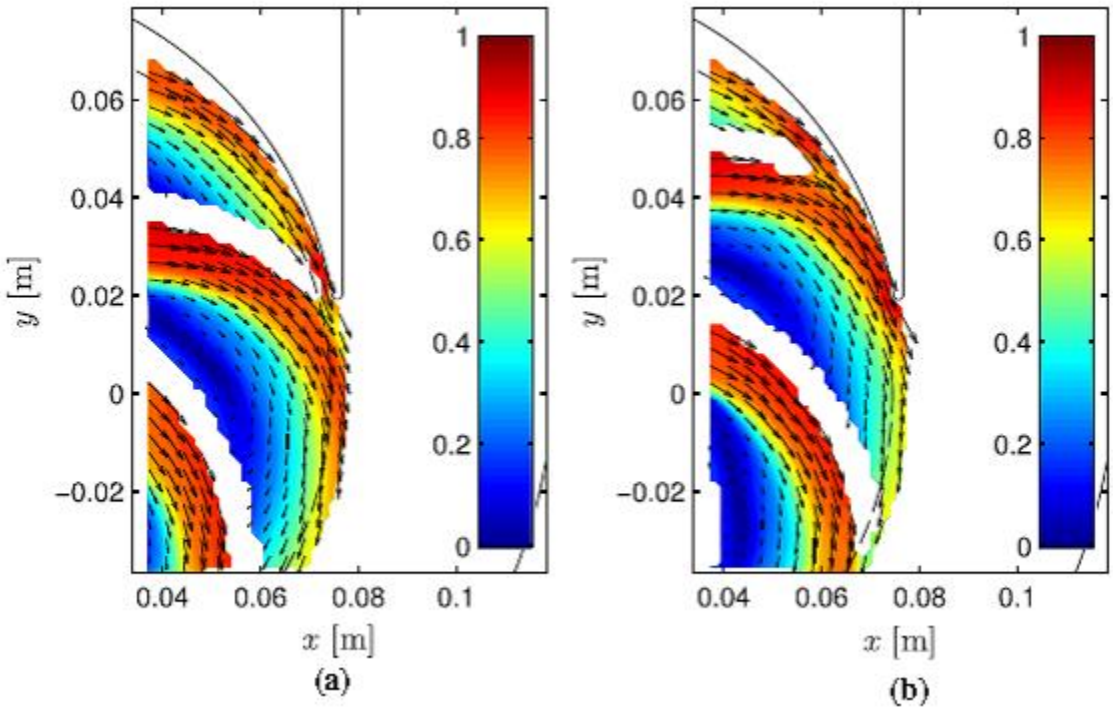

Figure 2.13: Average relative velocity flow inside the impeller at high flow rate [23]

when the gap between the blade and the tongue was minimum. The high value of the TKE prevented the fluid in the volute to leak to the outlet duct.

Many studies have been completed about the flow inside a centrifugal pump as discussed above. However, comparison of the fluid structure inside impellers that have a different number of blades has not been studied using PIV measurements yet. Using PIV measurements, a fluid structure along the passage of the impeller can be obtained without a time consuming and produce a small errors. Therefore, in this study, the fluid structure inside the 5 and 7 bladed impellers are observed using PIV measurements to understand the behavior of the fluid flow at high flow rates, the design flow rate and low flow rates.

Chapter 3

Experimental Methodology

The experimental methodology is discussed in this chapter. It consists of experimental apparatus, designing and manufacturing the laboratory impellers, impeller performance measurements and PIV measurements set up.

3.1 Experimental test apparatus

In order to conduct the experiment, a new test rig was built because the previous pump test rig in the turbulent flow laboratory at the University of Waterloo was not suitable to use for the present study. However, several parts from the old rig were taken and utilized in the new pump test rig. A closed circuit system was designed for the test pump rig so that it saves water and particle usage. The total capacity of the system was approximately 0.3 m^3. An ABS inlet pipe was connected between the reservoir and the pressurized tank. The inlet diameter and the total length of the inlet pipe were 101.6 mm and 15 times of the pipe diameter (15D), respectively. Two 50.8 mm ABS pipes were connected between the reservoir and the pressurized tank as the return channel. The length, width, and height of the PVC reservoir tank was 625 mm, 450 mm and 625 mm, respectively. The pressurized tank was made of 12.7 mm thick acrylic and has a length, width and height of 625 mm, 130 mm and 625 mm, respectively. The reason that transparent acrylic material was used for the pressurized tank was to facilitate the penetration of a laser light for PIV measurements.

The back of the pressurized tank was equipped with a window which could be removed together with the impeller and shaft assembly. A shaft seal housing was also mounted on the window. The shaft seal used the double-lip wipers type built using Buna-N material.

The shaft seal prevented the water from leaking from the gap between the shaft and the window to the atmosphere. The static seal between the window and pressurized tank surfaces used O-ring built using Viton material. The shaft was made of aluminum, 50.8 mm diameter with a length of 600 mm. Moreover, a total of two 15.875 mm shaft size bearings were used to support the shaft. In order to allow the impeller to rotate freely and to prevent fluid leakage from the pressurized tank to the inlet suction impeller, a small clearance between the stationary ring and rotary ring was allowed. The stationary ring is the wearing ring while the rotating ring is the sealing ring.

To control the flow rate, a 101.6 mm globe valve was installed in the inlet pipe close to the reservoir. Since the outlet flow from the globe valve is known to be unsteady, a flow straightener was installed after the globe valve. The dimension of the flow straightener can be seen in figure 3.3. In total 35 holes were drilled on 27 mm thickness of an acrylic sheet. The specific location of the flow straightener and globe valve on the inlet pipe are presented in section 3.3.1.

A variable speed DC motor manufactured by Baldor was used to rotate the shaft and the impeller. The DC motor was a permanent magnet type motor. The speed controller was Ratiotrol controllers Beta II series single phase adjustable speed manufactured by Boston Gear. The complete specifications of motors and the controller can be seen in Table 3.1. To connect the shaft and motor, a jaw coupling manufactured by Love Joy was used.

Table 3.1: DC motor specification

Motor		Controller	
Manufacture	Baldor/Boston Gear	Manufacture	Boston Gear
Model	PM 9100ATF-B	Model	RB A3
Power Rating	1 HP	Input Voltage	115 ±10%
Base Speed	1750 Rpm	Rating Current	10 A
		Load Change	0.5 %
		Output Voltage change	1 %
		Speed Range	200:1

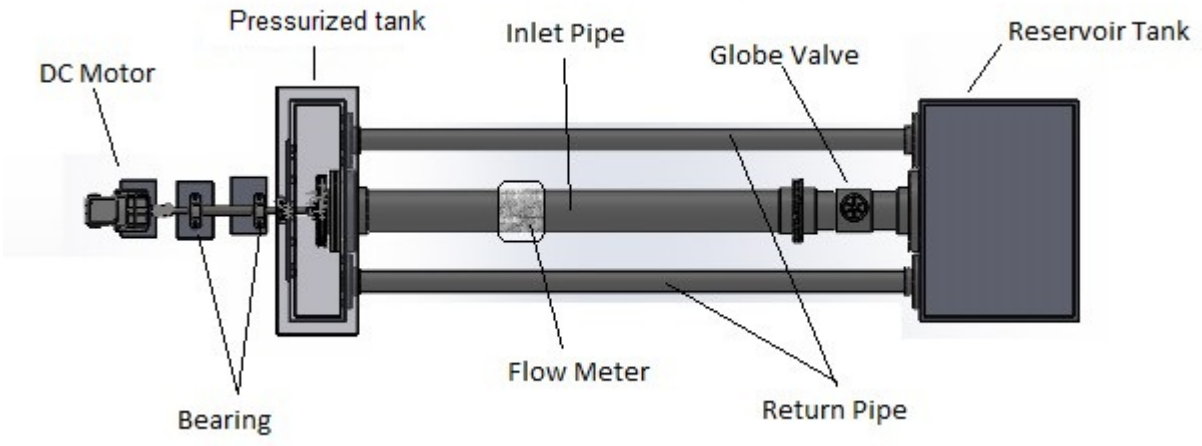

Figure 3.1: Experimental pump testing rig top view

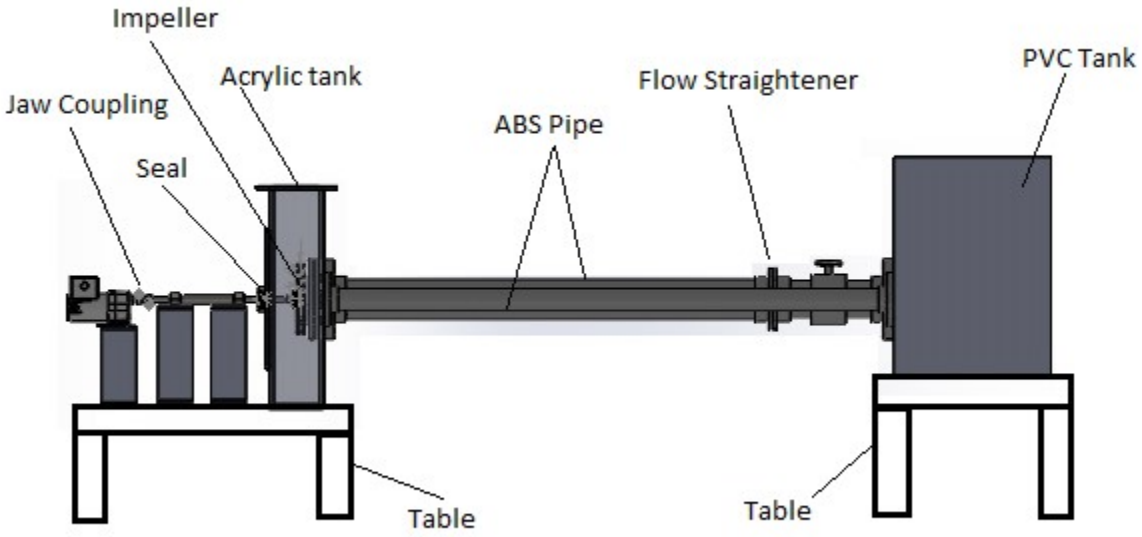

Figure 3.2: Experimental pump testing rig side view

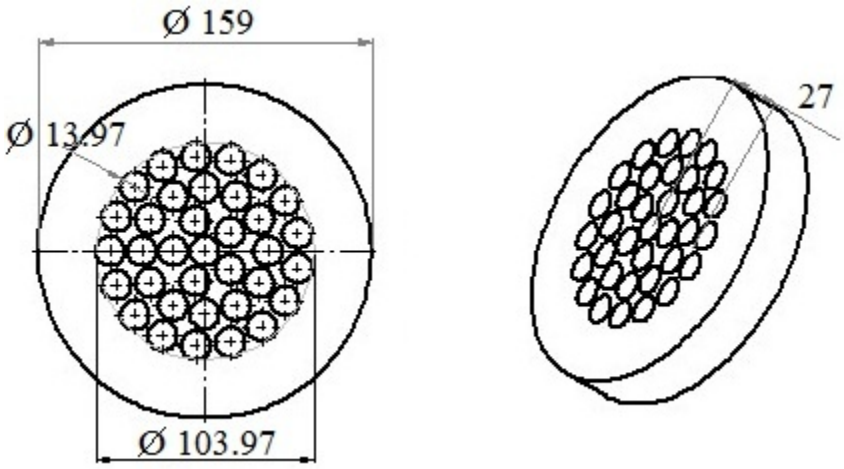

Figure 3.3: Flow straightener installed downstream of the globe valve (dimensions : mm)

3.2 Designing and manufacturing laboratory impeller

3.2.1 Impeller design

Two impellers, one with 5 blades and one with 7 blades were manufactured using acrylic material in order to conduct PIV measurements. Similar to the pressurized tank, the impellers were built using acrylic so a laser light could penetrate the blades and a camera could capture the particle movement. The impellers were designed to be two dimensional (2D) in order to simplify the manufacturing process. The 2D impeller also has the benefit of reducing the axial movement of the particles so the out of plane error can be reduced. The blade was designed to have a constant blade angle of 30°. To obtain the blade curvature, the log spiral blade profile, which was introduced by Pfleiderer [37] was utilized. The log spiral profile equation is shown in equation 3.1.

$$\Theta = 99.1217 \ln(\frac{R}{R_i}) \tag{3.1}$$

The Θ is the angle between the blade radius R and the inlet blade radius R_i. The detailed geometry of the impellers can be seen in Table 3.2. Since the inlet flow of the impeller changes from axial to radial, it was necessary to install a flow conditioner at the center of the impeller (see figure 3.5) so that the fluid entered into the impeller smoothly.

Because a flow conditioner was utilized, the inlet shroud diameter was designed to be bigger than the calculated size.

Table 3.2: Impeller and blade specific geometry

Inlet radius (R_i)	82 mm
Outlet radius (R_o)	200 mm
Shrouded inner radius (R_s)	102 mm
Inlet blade height (b_1)	12.5 mm
Outlet blade height (b_2)	11 mm
Inlet shrouded blade heigth (b_s)	12.25 mm
Blade thickness (t_b)	6 mm
Number of blades (Z)	5 and 7
Inlet blade angle (β_1)	30^o
Outlet blade angle (β_2)	30^o
Blade rake	0^o
Hub Thickness (t_h)	6 mm
Shroud Thickness (t_s)	11.5 mm

3.2.2 Impeller manufacturing

The impeller drawings are shown in figures 3.4 and 3.5; it was drawn in the Solid Works CAD program. For manufacturing, the draft was converted to a CNC program called MasterCam. Each impeller required 2 pieces of acrylic sheet. A transparent acrylic sheet with a thickness of 25.4 mm was manufactured into the hub part and another acrylic sheet of similar width was used for the shroud part.

Manufacturing of the impeller assemblies was done with a 5 axis CNC machine; the acrylic sheet for the hub part was cut and the only materials left were 6 mm thickness, t_h, of the blade plate and 5 or 7 blades. The inlet blade height was set to 12.5 mm and the outlet blade height was set to 11 mm. For ease of manufacturing, the blade height was cut straight from the inlet to the outlet along the passage. Moreover, as mentioned in the previous section the impeller was designed to be 2D so the blade was also straight across the passage and tapered along the passage.

The shroud part included grooves for the blades slots and the sealing ring. One side of the acrylic sheet was cut for the inclined grooves and the other side was cut to build

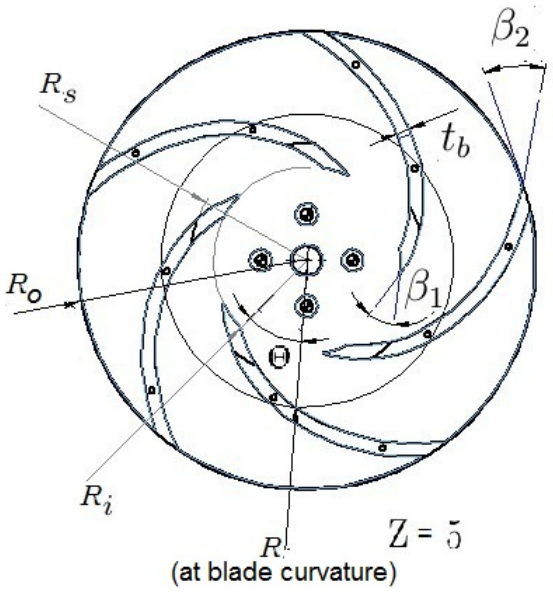

Figure 3.4: Blade geometry and notation for number of blades Z=5

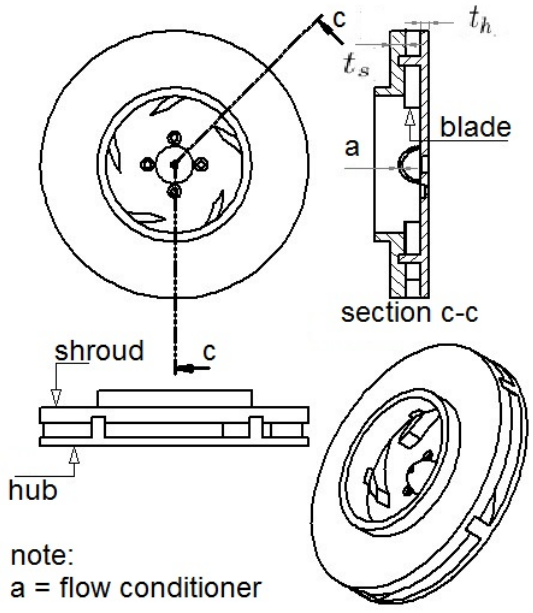

Figure 3.5: Cross section and impeller assembly for number of blades Z= 5

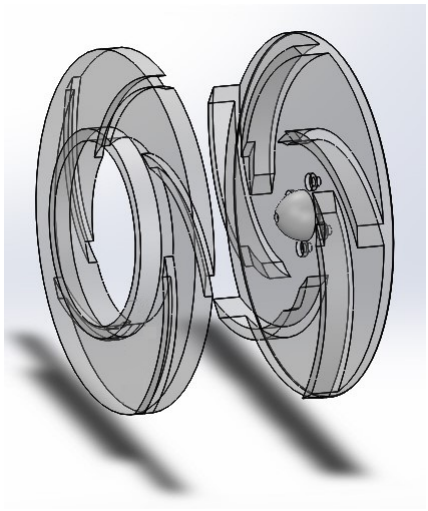

Figure 3.6: Hub and shroud parts picture drawn in $Solidworks^{Tm}$ program

the sealing ring. The sealing ring was cut so that the clearance between the sealing ring and the wearing ring was set to 0.50 mm. To mount the hub part to the shroud part, two countersunk bolts were utilized on each blade to tighten both pieces. To transfer the rotation of the shaft to the impeller, it required a bushing. The bushing was mounted to the impeller assembly by four countersunk bolts while the bushing was tightened to the shaft by three setscrews.

3.3 Impeller performance measurement

Since the impellers used in this experiment are newly designed impellers, the performance measurement must be conducted to know the impeller characteristics. Performance measurements were taken at several impeller speeds (200-500 rpm). The performance parameters which were obtained from the measurement are:

- Flow rate of the closed loop system (Q)
- Fluid head rise through the impeller (H)
- DC motor power (P) as the brake horsepower (BHP)

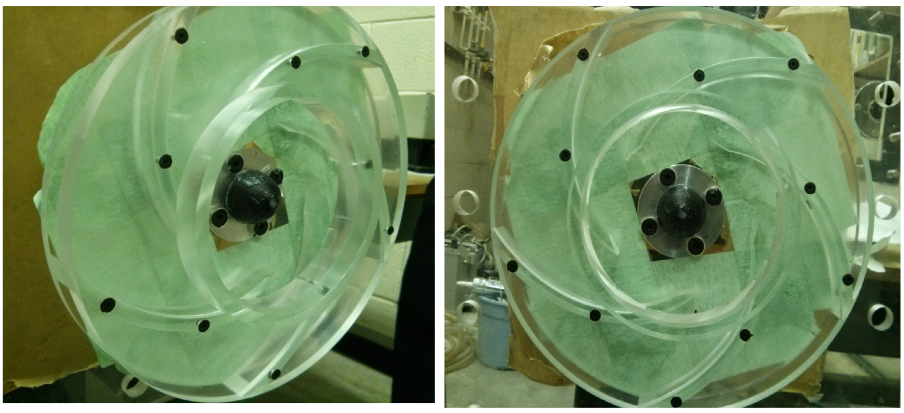

Figure 3.7: Pictures of 5 bladed impeller assembly

Generally, to calculate the efficiency, equation 1.13 was used. However, a modification must be made so that the efficiency calculation obtained was really the impeller efficiency. In addition, because the efficiency of the variable speed DC motor was very poor at low speeds, this problem can cause absurd results. Mechanical loss which can affect the efficiency calculations must be ruled out. Therefore, the efficiency calculation for this study is shown in equation 3.2.

$$\eta = \frac{WHP}{BHP} = \frac{\rho g Q H}{\text{DC motor power} - \text{DC motor tare power}} \tag{3.2}$$

Where η is pump efficiency, ρ is fluid density, H is head rise and Q is system flow rate.

The DC motor tare power was obtained by measuring the power of the motor when the pump was pumping air. Therefore, the DC motor tare power consists of the torque to rotate the impeller, bearings, shaft seal and the motor itself. In addition, the impeller, bearing, shaft seal and motor shaft torque were assumed constant for different loads. The DC motor power was obtained using equation 3.3.

$$\text{Power DC Motor } (P) = \text{Voltage } (V_{DC}) \times \text{Current } (I) \tag{3.3}$$

Dimensionless performance parameters such as flow coefficient (Φ), Head coefficient (Ψ) and specific speed (n_s) were obtained using equations 1.7, 1.8 and 1.10.

3.3.1 Flow rate measurement

In this study, the ultrasonic flow meter System 990N Uniflow was utilized to obtain the flow rate. The System 990N Uniflow complies with NEMA 4X and NEMA 7 standard for Clamp-on Transit-Time Ultrasonic Flow meters [9]. The benefit of this type of measurement is that no instrument penetration was required, it was easy to use, very effective and accurate for many applications of flow rate measurements. It is mentioned in the manual that the accuracy of this flow meter is ± 1/2% of actual flow possible with zero flow calibration or ± 1% to 3% if the flow is measured under standard application conditions. The basic principle of the ultrasonic measurement is based on the fact that an ultrasound wave will have different transit time depending on the direction and the velocity of the fluid motion when it penetrates the fluid motion. In order to obtain accurate flow rate measurement, two transducer are installed on the known pipe size in upstream and downstream configuration (figure 3.8) so that each wave experiences different transit time because of the flow direction. The transit time difference of each transducer, then, will be used to calculate the fluid velocity. The fluid velocity together with the known pipe data can be used to obtain the flow rate. It is also mentioned in the field manual that the flow sensitivity is 0.003 m/sec even at shut off condition and the drift stability is better than 0.0091 m/sec in most applications meaning that this system 990N Uniflow can be utilized to measure any low flow rate [9].

The Ultrasonic flow meter has three main parts which are:

- Flow display computer which consists of
    1. power supply
    2. data processor
    3. hand held control
    4. display units
- Transducer
- Mounting track

There are two types of transducer mounting configurations which are reflect and direct configurations. The configuration is chosen based on the size and material of the pipe. In this study, since the transducers were mounted on the ABS material that is categorized as plastic, the direct transducer configuration was applied. The location to put the transducers should not be close to a fitting or valve because it can influence the fluid velocity

profile. Hence, it can affect the reading. However, the field manual does not state the specific length from the fitting or valve to the transducers. Therefore, to obtain the flow rate measurements that has a measurement uncertainty around 2% at high flow rate, the ultrasound flow meter was located 13D from the custom built flow straightener. The full layout of the inlet pipe can be seen in figure 3.8.

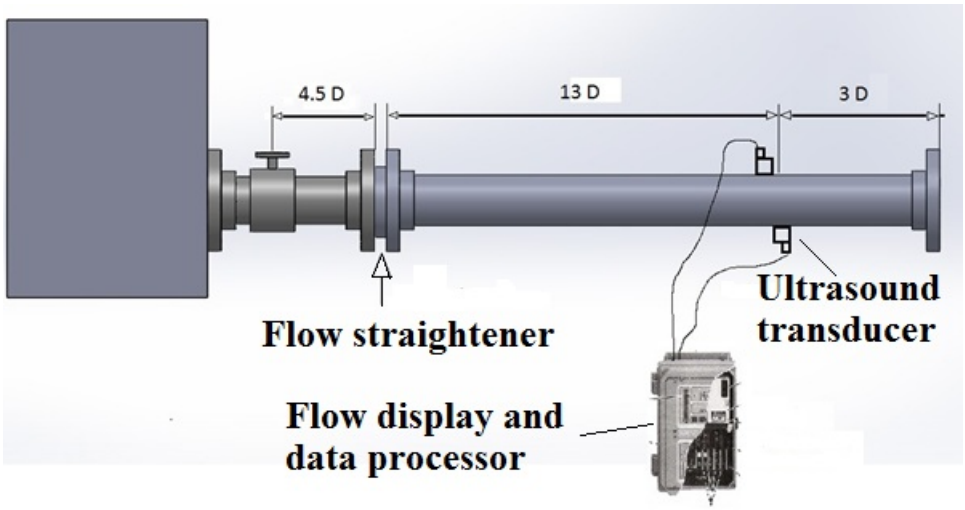

Figure 3.8: Layout of the straight run pipe for the ultrasound flow meter

The contact surface of the transducers must be clean and free from debris. The manufacturer suggests to install the transducers horizontally because often fluid debris are collected in the bottom of the pipe. The pipe must have ultrasonic gel applied to amplify the transducers signal. In this study, Flex RTV 7500 industrial silicone was used as the ultrasonic gel. In order to obtain a good result in the flow reading, it is important to input data correctly. The input data is presented in Table 3.3.

In order to obtain good accuracy of the measurements, the zero flow calibration set was conducted. The output reading was converted into 4 - 20 mA signal . Since the minimum and maximum output range in the present were set to $-5\ m^3/hour$ and $50\ m^3/hour$, the equation to obtain the flow rate in $m^3/hour$ is

$$\text{Flow Rate } (m^3/hour) = 3.4375\ \text{X} - 18.75 \tag{3.4}$$

, where X is the output signal in mA.

Table 3.3: Input data of experimental set up to the System 990N Uniflow

Pipe Material	ABS
Pipe outsie diameter	4.5 inch
Pipe wall thickness	0.237 inch
Liquid use	Water (default)
Liquid temperature	20 C (default)
Sound velocity in ABS	90000 in/sec
Sound velocity in water	1500 m/s

3.3.2 Head rise measurement

The head rise between the suction and discharge of the impeller was measured by subtracting the inlet and exit of the impeller stagnation pressure. Two Kiel probes were utilized to measure the stagnation pressure. The position of the Kiel probe in the inlet pipe was set in the middle of the pipe where the highest stagnation pressure was achieved. The exit Kiel probe was set at the exit which was at the same level to the inlet probe. It was also placed in the mid section of the passage height.

The valydine differential pressure transducer which has a 6.89 kN/m^2 range was utilized to collect the pressure rise of the impeller. The main parts of this pressure transducer are coils and a diaphragm as seen in figure 3.9. The basic principle of the pressure transducer used in the present based on the fact that when the diaphragm moves to one side of the cavity, it causes the coils to induces electricity. The electricity signal then is amplified to the value which is proportional to the voltage requirement of the data acquisition system which was set in the range of $0 \pm 10V_{DC}$.

A static water column in a container was set at a certain level to know the static pressure. The known static pressure was used to calibrate the pressure transducer. The illustration of the pressure calibration process is presented in figure 3.10. The result of the calibration pressure transducer process is presented in figure 3.11.

3.3.3 Brake horsepower measurement

The electrical power measurement of a DC Motor was calculated by multiplying the voltage and the current of the motor. A simple electrical circuit was utilized to measure voltage and current. The current measurement used a 0.2 ohm resistor (Resistor Coils Delaylines,

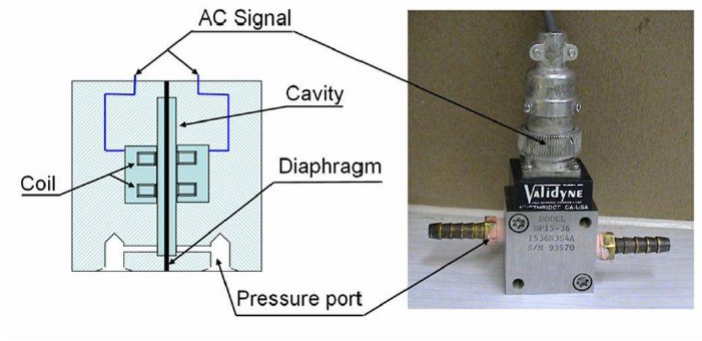

Figure 3.9: Schematic diagram and picture of a Validyne pressure transducer [3]

RCD) which was an accurate shunt resistor. The accuracy of the resistor was about 1%. The shunt resistor was connected in series with the motor DC electric circuit. The basic principle of the shunt resistor is when it is connected in series with the DC motor circuit, the voltage across the shunt resistor drops. The voltage drop signal was connected to Digital Multimeter (DMM) and Data Acquisition module. The voltage drop was then utilized to calculate the current by dividing with the voltage drop with the specific value of the resistor. Circuit wiring was connected in parallel to the DC motor circuit to measure the voltage of the motor. The illustration of the electrical circuit is presented in figure 3.12. To verify the accuracy of the current shunt measurement, a multimeter (Fluke 87) which the accuracy of is $\pm 0.2\% readings + 2$ when measuring the DC current was installed. The current resulted from shunt measurements and the current reading by a multimeter were similar.

3.4 Pump performance data acquisition

To collect the pump performance data, a Keithley Model 2700 Multimeter equipped with a module multiplexer card 7000-20 channel was used. Module 7000 multiplexer is a mechanical data acquisition system which provides 22 channels to collect electrical inputs. The maximum DC voltage and current that this module can handle are 300 VDC and 3 Amp. To measure a voltage signal, channels input 1-20 can be used whereas channels 21 and 22 are used to measure current. More detail about the Digital Multimeter and the module can be found in the Model 2700 Multimeter/switch system user's manual [20].

To read or scan the signals, a Microsoft windows computer with Xlink software installed

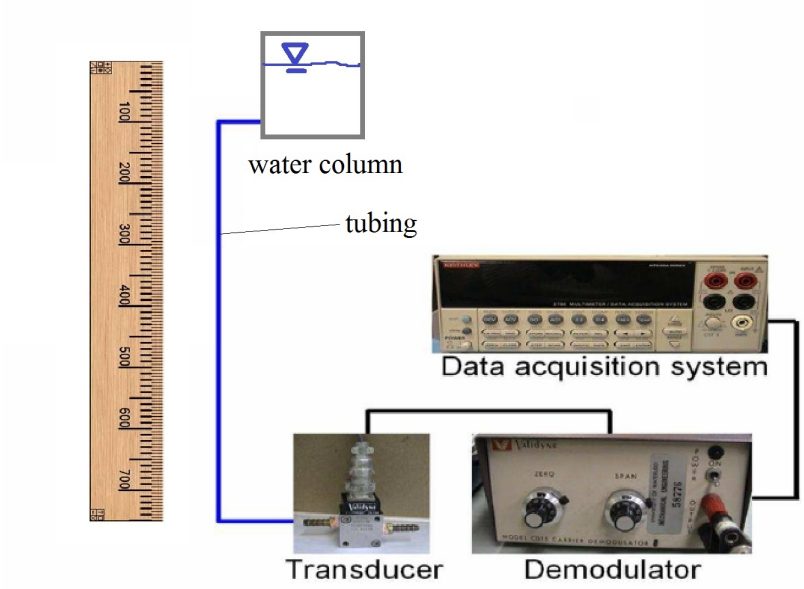

Figure 3.10: The layout of calibration of the pressure transducer conducted in the present

was used. The DMM was connected with the computer through RS-232 connection cable. When scanning the data, the time delay was set to 1 second. A 0-10 VDC signal obtained from the pressure transducer was connected to channel 1. The voltage signal from the electrical DC motor circuit was connected to channel 4 and the voltage drop signal to measure the current circuit was connected to channel 6. The 4-20 mA signal for measuring the flow meter was connected to channel 21. In total, 100 data of each parameter were recorded to obtain pump performance at a certain flow rate.

3.5 PIV measurement

This section discusses about the PIV measurement setup in this research. It includes the details of the camera, laser, particles, calibration tool and field of view of the image, velocity vector and turbulence intensity (TI) and fluid angle deviation (β_d) calculations.

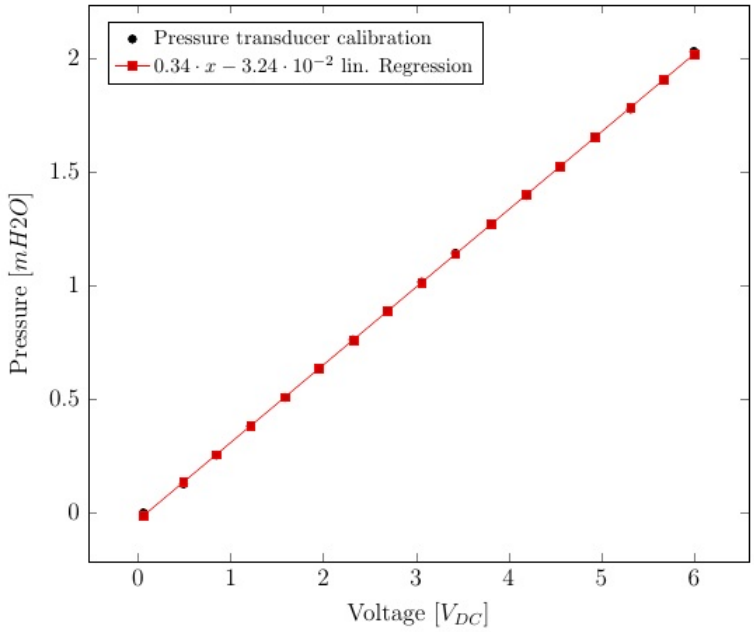

Figure 3.11: the calibration result of the 34.47 Kpa pressure transducer

3.5.1 Camera for recording images

In the present, the Dantec Dynamics FlowSense EO 4M CCD camera together with Nikkor 1:28 D lens were used. In addition, a Kento Pro 1D UV (W) filter was used. The resolution of the camera was 2048 x 2048 $pixels^2$. The camera was mounted on a bracket which allowed the camera to move parallel to the impeller surface. The camera was located 420 mm from the back surface of the impeller and focused at the middle of the passage. The field of view of the image was around 70 x 70 mm^2 which the scale factor was around 6.4. It was noted that the limiting number of the images that could be recorded during each process was 437 image pairs. Hence, in order to obtain 1000 images, the experiments was repeated 3 times.

3.5.2 Gemini laser system

The Gemini Solo II PIV 15Hz Nd:YAG laser from New Wave Research was used in the present. The Gemini laser system was known as a compact dual laser system consisting

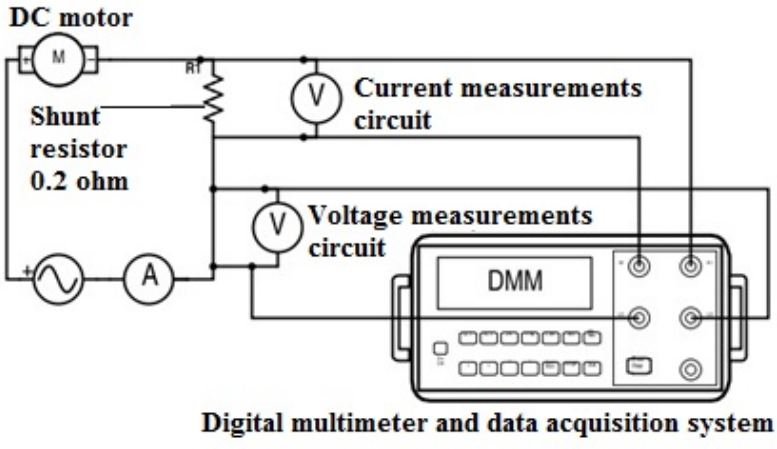

Figure 3.12: Diagram of electrical circuit used to measure current and voltage of the motor

of one power supply unit and one laser head unit. The power supply unit has a cooling system for laser because this laser is categorized as a Class 4 laser. The laser head emits light with actually a wavelength of 1064 nm, but since most of camera is best when capture green and red light, the light frequency is doubled to a wavelength of 532 nm. This system can produce 30 mJ of laser energy and it can be adjusted based on research needs. A knob and a digital screen are utilized in the power supply unit to control and display the laser energy. The value of the display can be adjusted from 0 to 999. In the present, 250-260 was set for laser energy. This energy level was chosen because in this range value, it was enough for the camera to capture the light reflected from the particles but it was less light reflection from the impeller parts.

As mentioned in the previous chapter, to obtain minimum measurement error, the laser sheet was adjusted so that it has 1 mm thickness at the location of interest. Hence, the laser head and the cylindrical lens were placed 1000 mm and 500 mm, respectively from the region of the interest to obtain 1 mm laser width. The experimental set up for the present is shown in figure 3.13.

The unit consists of 2 laser that can produce light with maximum hight repetition rate. In this research, the laser and camera were synchronized to capture the similar impeller passage. An electric trigger signal was used to trigger the laser and camera to start firing and recording the image. A notch plate and H21A1 photo-transistor optical interrupter were used to obtain the trigger signal. The sensor sent 5 VDC signal to the timer box 80N77 when the plate interrupts the optical sensor. However, when the notch plate was

parallel to the sensor, the signal switched to 0 VDC and the laser and camera started firing and recording the image.

Moreover, it has also been mentioned previously that the time between pulses of the laser has to be set so that the particles have enough displacement and only a small error because the lost of particles from the interrogation area. "The rule of thumb" for setting the timing of laser pulses is that the time should be set so that the displacement of the seeding particles is close to a quarter width of an interrogation area (IA) [33][43]. However, for the centrifugal pump application, the impeller rotation much faster than the fluid velocity. In the present, a small experiment was conducted to determine the appropriate time between pulses. 150 pair images at 100 % and 25 % rate flow were captured for time between pulses 50, 100, 175 and 250 μs. The results can be seen in figures 3.14 and 3.15.

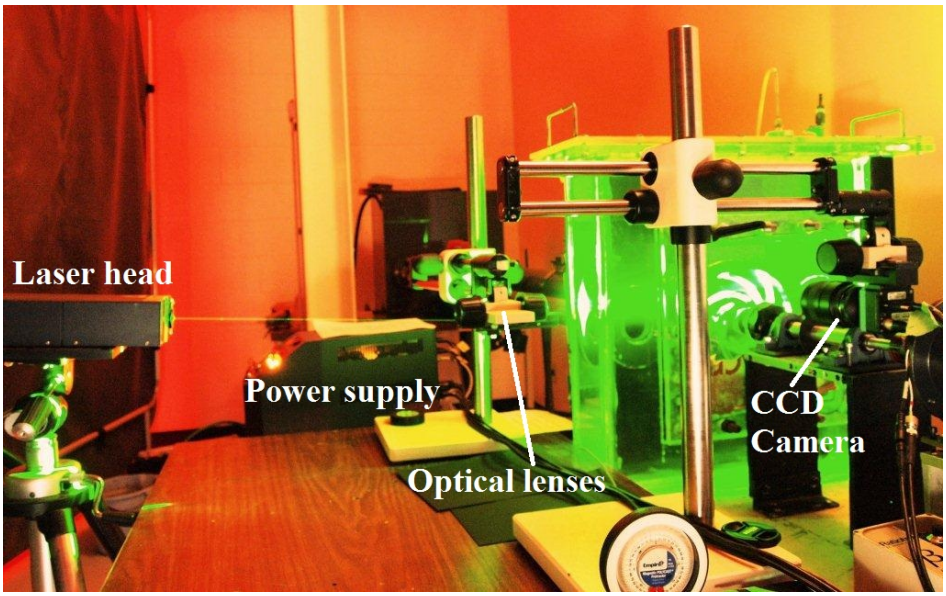

Figure 3.13: A picture of the experimental set up of PIV measurements

The results showed that the value of the mean normalized velocity (W_p/u_2) was about similar if the time between pulses was changed from 50 to 175 μs (figure 3.14). However, it started to deviate when the time between pulses was adjusted to 250 μs. The PIV measurements result which is presented in figure 3.15 shows that the delay of the laser pulses causes the vortices in the passage to be weakened. In the present, the time between pulses was chosen in the range of 50 to 75 μs because the particles were seen have enough displacement and it captured good flow behavior at low flow rate which will be discussed later.

3.5.3 Seeding particles

The seeding particles used in the present were Pliolite VT which were supplied by Eliokem Inc. (now the company is taken over by Omnova Solution Inc.). This particle was chosen because it has almost similar density with the medium of the experiment (water) and it was noted that this particle has good signal to noise ratio [3]. The specific gravity of the particles is 1.03. To obtain the required particle diameter, particles were sieved so that only particles which have diameter of 50-75 μm were used. About 1 g of the particles were inserted to the water so that in average of 10 particles were captured in each interrogation area. Stirring water in the reservoir was necessary so that the particles spread evenly.

3.5.4 Calibration tool and shifting x and y position

To obtain the actual dimensions of the image, a two point detection method was utilized similar to Altaf [3]. However, instead of marking the back impeller surface, this research used a tool. This method is believed to be more accurate to Altaf's [3] because in the past, the camera was focused on the back impeller surface, but in the present, camera was focused on the tool surface that was located at the middle of the impeller. However, the accuracy depends on the manufacturing of the tool. A calibration tool was built for each impeller which is presented in figure 3.16. Each tool has 2 reference points with a known dimension. The length between two points (A and B) became the input data to calculate the scale factor which was done with the Dantec Dynamic Studio software. The software, then, determined the location of the points relative to the image in x and y coordinates (A_x, B_x, A_y and B_y). The Dantec Dynamic Studio software also determined the width (w) and the length (l) of the picture. Then, all of input dimension data and output data of the points location were processed to get the new position of x and y of the image from the center of impeller using the trigonometry formula. The illustration of the image to the center of the impeller is shown in figure 3.17. The input and output data of the 5 and 7 bladed impellers are shown in Table 3.5.4.

3.5.5 Image processing

To process the pair of particle images, the PIV adaptive technique which is based on the cross-correlation method was used [40]. The benefit of this technique is that it can choose the appropriate shape of the interrogation area based on the velocity gradient in the flow field. The technique also picked the appropriate size of interrogation area

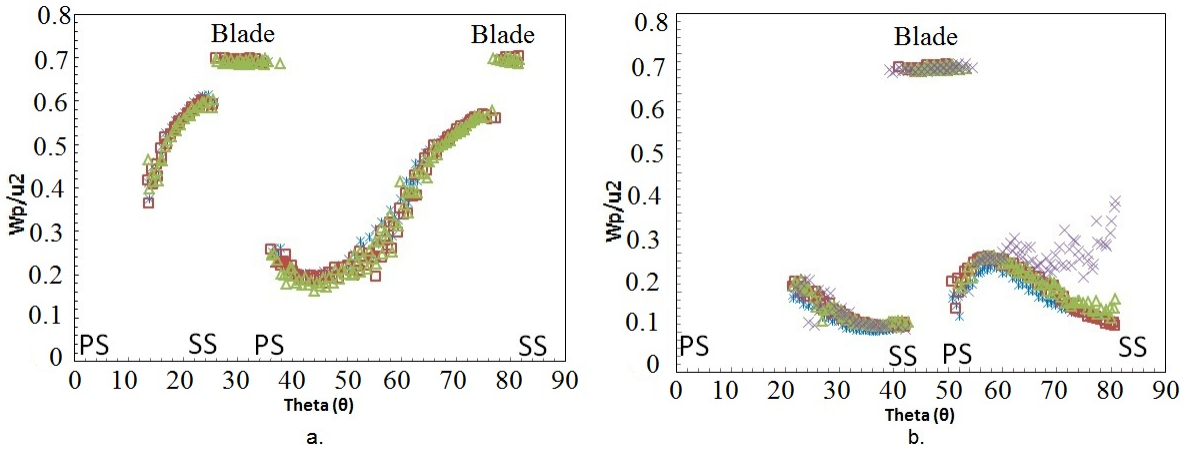

Figure 3.14: Wp/u_2 - θ chart in different time between pulses at a. 100 % flow rate and R/R2=0.8, b. 25 % rate flow amd R/R2=0.7 mm, the time between pulses $*$ is 50 ms, $\square$ is 100 ms, $\triangle$ is 175 ms and $\times$ is 250 ms

Table 3.4: The input dimensions and the output data from The Dantec Studio software to calculate the new coordinate of the images for figure 3.17

Dimension (in mm)	5 blades	7 blades
a	90	90
b	60	60
c	70	60
W	71.32	70.65
L	71.32	70.65
Ax	1.572	7.061
Ay	28.25	38.16
Bx	69.66	66.19
By	44.48	48.36
x_{new}	6.44	10.44
y_{new}	87.23	95.55

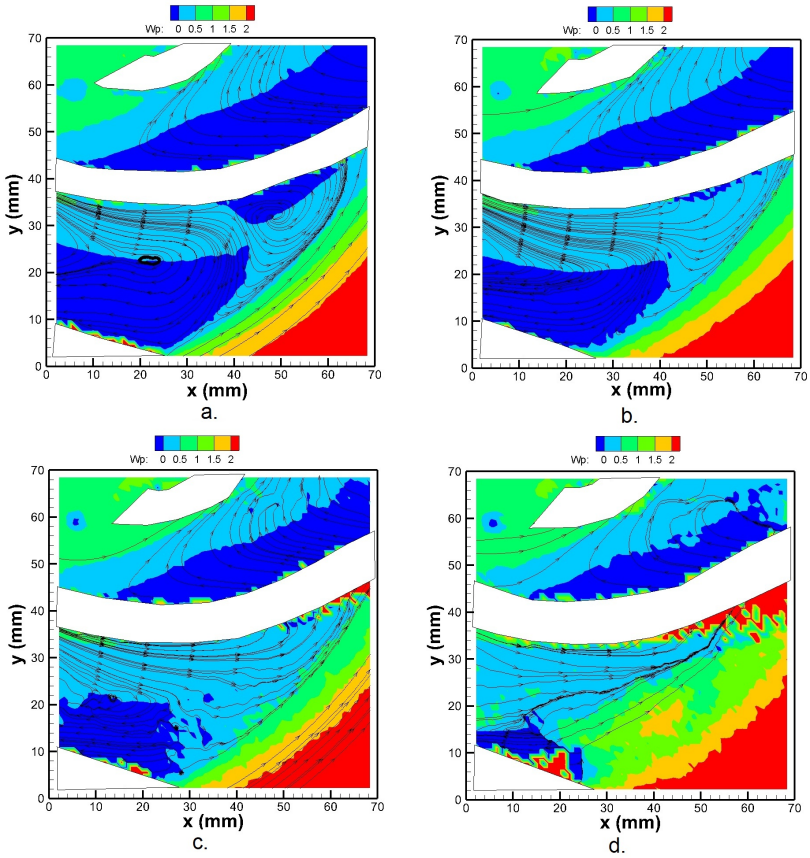

Figure 3.15: Flow visualization of 25 % flow rate at a passage of impeller for several times between pulses a. 50 μs, b. 100 μs, c. 175 μs, d. 250 μs.

based on the desired number of particles. In the present, the iteration to calculate the particles displacement started from maximum interrogation area (IA) size of 128 pixels to minimum IA size of 32 pixels, where the grid step size was chosen as 32 pixels. To keep the error less than 4%, the desired number of particles in an interrogation area was set to be 8 particles [3]. The PIV adaptive method offers an option to apply window function and frequency filtering features which are also based on cross-correlation method. The windowing feature will determine the best interrogation area shape whereas the filtering feature filters the unwanted frequencies. In the present, the window was set to a Gaussian function and the value of k was 0.75 (default). Similar to a window function, the filter function was set to No-DC (default). Moreover, the adaptive PIV method validated the

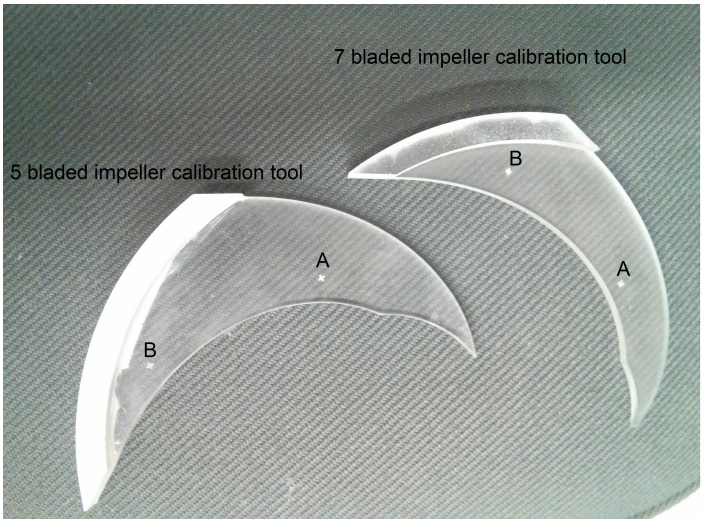

Figure 3.16: A picture of calibration tools for the 5 and 7 bladed impellers

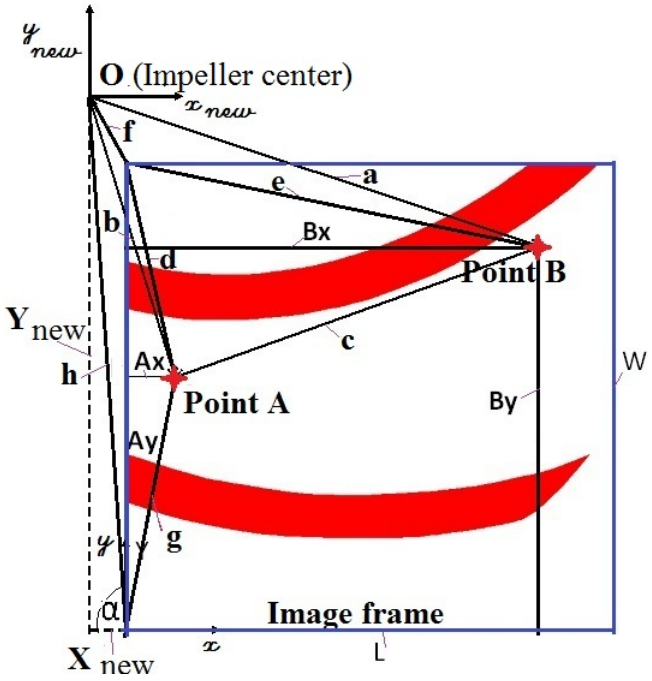

Figure 3.17: Illustration to calculate the new coordinate of the picture to the center of the impeller

velocity measurements by initially applying peak validation, then comparing each vector to the nearest neighbors vector using a universal outliers detection algorithm. In this research, the local neighborhood to validate the vector was chosen in the size of 3 x 3 IA. The image post processing resulted in 3722 vectors for each pair of images. The vectors that were displayed in the adaptive PIV result were the absolute velocity ($\mathbf{v}$) of the particles.

3.5.6 Calculating relative velocity

It has been mentioned in subsection 3.5.5 that the velocity that was obtained from the PIV results is absolute velocity ($\mathbf{v}$). In order to understand the relative fluid motion, it is necessary to determine the relative velocity. Figure 3.18 outlines the possible vectors of an interrogation area. It is clear that the absolute velocity is a summation of the rotational velocity ($\mathbf{u}$) and the relative velocity (equation 3.5). Then, the absolute velocity in the x and y coordinates are derived as shown in equation 3.6 and 3.7, respectively.

$$v = u + W \tag{3.5}$$
$$v_x = u_x + W_x \tag{3.6}$$
$$v_y = u_y + W_y \tag{3.7}$$

where the rotational velocity was calculated by multiplying the angular velocity (ω) and the local radius of vectors (R) (equation 3.8). If the rotational velocity is derived in x and y coordinates, the rotational velocity can be expressed in equation 3.9 and 3.10.

$$u_r = \omega \times R \tag{3.8}$$
$$u_y = \omega \times x_{new} \tag{3.9}$$
$$u_x = \omega \times y_{new} \tag{3.10}$$

After obtaining the relative velocity in the x and y coordinates then equation 3.13 and 3.14 were derived to get the relative velocity in radial (r) and tangential (t) coordinates.

$$w_r = w_x \cos\theta - w_y \cos\alpha \tag{3.11}$$
$$w_r = w_x \frac{x_{new}}{R} - w_y \frac{y_{new}}{R} \tag{3.12}$$
$$w_t = w_x \cos\alpha + w_y \cos\theta \tag{3.13}$$
$$w_t = w_x \frac{y_{new}}{R} + w_y \frac{x_{new}}{R} \tag{3.14}$$

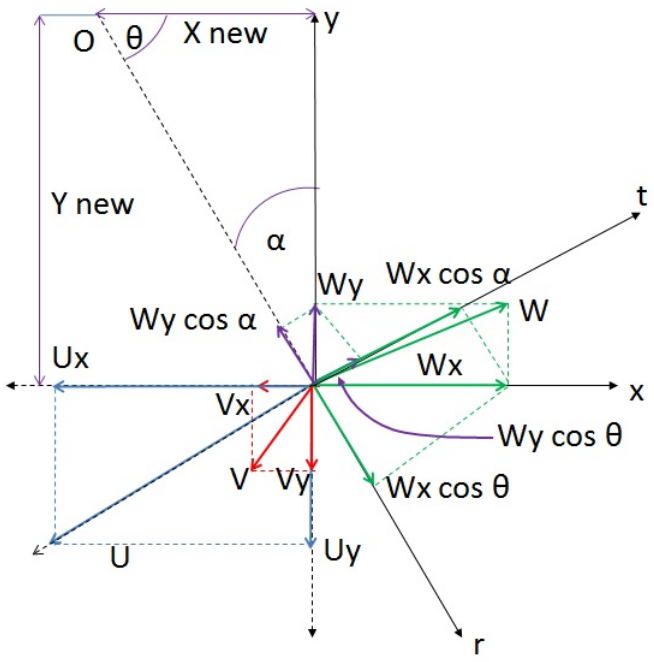

Figure 3.18: Outlined of vectors of an interrogation region with respect to x, y and r, θ coordinate system

For further analyzing purposes, it is necessary to get the relative velocity in primary and secondary coordinates. The primary coordinate is always parallel and follows the blade curvature. On the other hand, the secondary coordinate is perpendicular to the blade curvature. The blade curvature was determined to be 30^o to the tangential coordinate so the primary and secondary vectors is outlined as shown in figure 3.19. The primary and secondary relative velocity can be

$$w_p = w_t \cos 30^o + w_r \sin 30^o \tag{3.15}$$

$$w_t = w_t \sin 30^o + w_r \cos 30^o \tag{3.16}$$

The mean normalized relative velocity was calculated from 1000 velocity results of PIV measurements. All of the data were processed in Microsoft Excel to obtain the relative velocity in all of the coordinates. In addition, the flow field visualization which showed the possible streamlines of the flow inside the impeller passage was done in Tecplot.

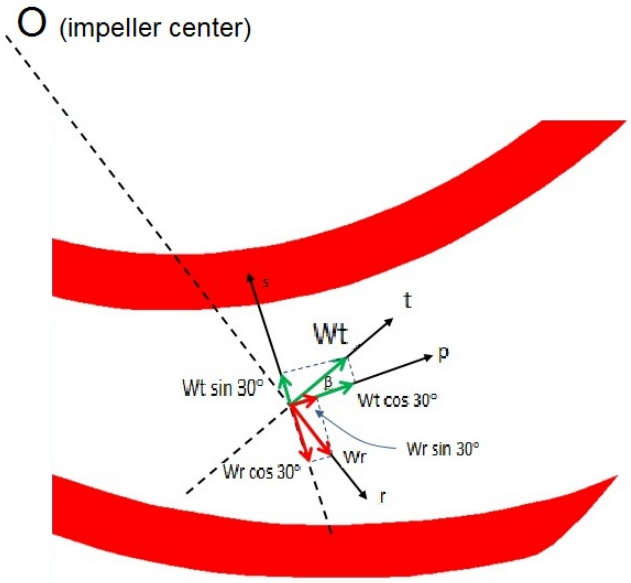

Figure 3.19: Outline of vectors at primary and secondary coordinate with respect to the primary (p) and secondary (s) coordinates

3.5.7 Image and field of view

The camera was placed so that it could capture from the inlet to the outlet diameter of the impeller. However, because the space available was so limited to place the camera and blade was so curved, the image could not capture a whole of the impeller passage. In order to obtain the flow structure of a passage, the measurements were conducted at several locations by controlling the delay times. For the 5 bladed impeller, the delay times (t_d) were 0 and 15 ms whereas for the 7 bladed impeller, the delay times (t_d) were 0, 14 and 30 ms. The Dantec Studio software [40] allowed users to set the delay time. The illustration of the field of view of the 7 bladed impeller that was taken at several delay times is shown in figure 3.20. Figure 3.21 shows an example of an particles image obtained by the camera during the experiment.

As mentioned in the previous sub section that the post processing used adaptive PIV technique. In this study, the measurements of the primary and secondary relative velocity were taken at 5 different locations which are at R/R_2 0.5, 0.6, 0.7, 0.8, 0.9. The illustration of the location is shown in figure 3.20.

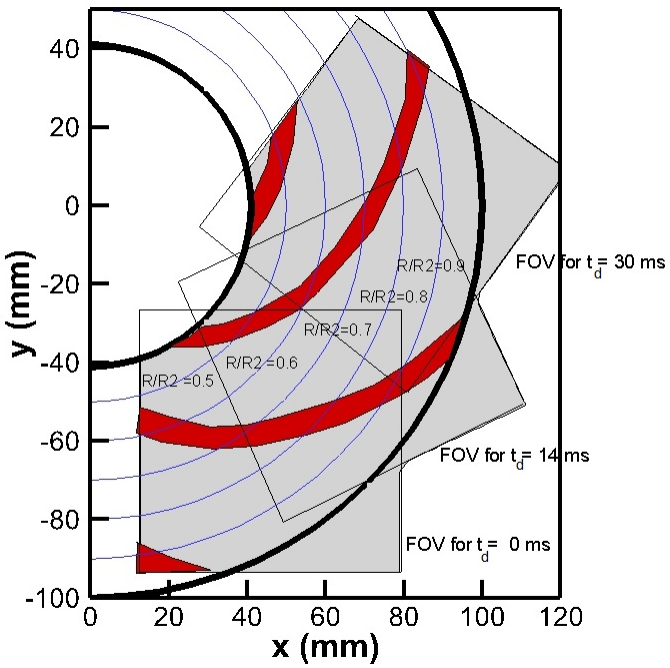

Figure 3.20: Illustration of 5 location measurements of the primary and secondary relative velocity for the 7 bladed impeller

3.5.8 PIV measurements result calculation

In the Results section, the mean normalized relative velocity charts with respect to primary and secondary coordinates (W_p/u_2 and W_s/u_2) is presented. Uncertainty of the mean normalized primary relative velocity is presented in Appendix A. It should be noted that the mean normalized primary and secondary velocity profile for the 5 bladed impeller is plotted from a combination of the results of images at time delay (t_d) 0 and 15 ms whereas for the 7 bladed impeller, it is plotted from a combination of the results of images at delay time (t_d) 0 and 14 ms. The example of W_p/u_2 plots are presented in figure 3.14. At the x axis, θ is the angle between the impeller center and measurement point. In the results section, the x axis is represented by dimensionless angle, ξ, that the minimum value is in the location of the blade pressure side and the maximum value is in the location of the blade suction side for all of point measurements in the circular arc (R/R_2).

Based on equations 3.15 and 3.16, when the primary velocity has a positive value, it means that the fluid most likely flows toward the outlet of the channel. However, when the primary velocity has a value close to zero or negative, the fluid might be stationary at

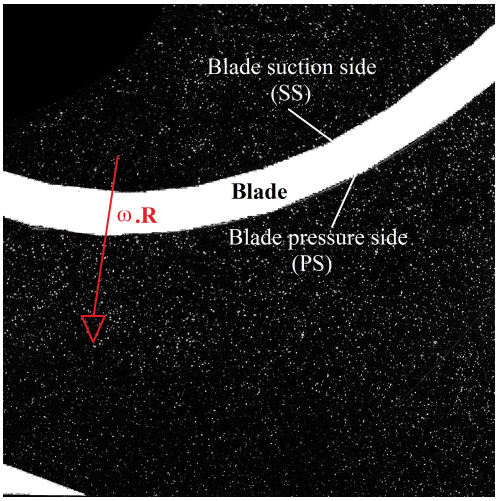

Figure 3.21: A picture of an image particles of the 5 bladed impeller at t_d = 15 ms

that location or it might move toward the inlet so that detailed observation is necessary to decide the flow structure. When the secondary relative velocity has a positive value, this means that the fluid most likely moves toward the blade pressure side. Alternatively, a negative value of the secondary velocity means that the fluid moves toward the suction side.

The results of PIV measurements allow presentation of the two dimensional streamlines of the fluid inside the impeller. Streamlines of fluid represent the direction of the fluid in the impeller passage which was obtained based on the value of the relative velocity (**W**).

PIV measurements also allow the calculation turbulence kinetic energy (TKE). TKE shows the fluctuation of fluid velocity. The relation of the TKE is presented in equation 3.17. Because in this study, the rotational velocity is constant at each point measurement, the fluid fluctuation (W') is similar to absolute velocity fluctuation. In this study, the flow fluctuation is represented by Turbulence Intensity (TI) which is normalized by the fluid local mean speed. If the value of TI is high, it explicitly means that the velocity is low or the fluid experiences high fluctuation. The relationship of TI and TKE is presented in equation 3.17 and 3.18. TI contours are presented in the present study for the 5 bladed impeller is a combination from results of images at t_d of 0 and 15 ms but for the 7 bladed impeller, the contour is from combination of images at t_d of 0, 14 and 30 ms.

$$TKE = \frac{\overline{W_x'^2} + \overline{W_y'^2}}{2} \tag{3.17}$$

$$TI = \sqrt{\frac{TKE}{\overline{W_x^2} + \overline{W_y^2}}} \tag{3.18}$$

Another result that can be obtained from the PIV measurements in this study is the fluid angle deviation (β_d). The relationship of β_d can be seen in equation 3.19 and 3.20

$$\beta_r = arctan\frac{W_r}{W_t} \tag{3.19}$$

$$\beta_d = \beta_r - \beta_2 \tag{3.20}$$

, where the β_r is local fluid angle and β_2 is blade angle which is 30^o. From above relationships, it can be inferred that if β_d has a value of zero it means that the fluid follows the blade curvature. If the value of β_d is less than 0^o, the fluid moves to the blade pressure side, whereas if the value of β_d is positive, the fluid moves to the suction side. Similar to primary and secondary velocity profile and TKE contours, the contours of β_d presented in this study are a combination from results of images at t_d of 0 and 15 ms for the 5 bladed impeller and 0, 14 and 30 ms for the 7 bladed impeller.

Chapter 4

Results and Discussion

This chapter discusses results that were achieved from this research. It includes performance results of the 5 and 7 bladed impellers and PIV results to understand the flow behavior inside the impellers. Since this study used a new experiment rig to test new designed impellers, it is necessary to conduct experiments at several impeller speeds to get the similarity data of the impeller. The comparisons are presented of performance results and flow structure obtained by PIV measurements of a 5 bladed impeller and a 7 bladed impeller. In the PIV measurements, plots and contours of the primary and secondary velocity components, turbulence intensity, fluid angle deviation and streamlines are presented to determine the fluid flow structure inside the passage of the 5 and 7 bladed impellers. Finally, the flow behavior between the 5 bladed and the 7 bladed impeller is compared at 25 %-140 % flow rates.

4.1 Performance results of the impellers

4.1.1 Results of performance measurements for 5 and 7 bladed impellers

To understand the performance of the impellers which are designed to deliver fluid at 300 rpm, the pump performance parameters such as head, flow rate, head coefficient, flow coefficient and efficiency are obtained. The experiment was also conducted to find the BEP of the impellers. The head and flow rate curve of the 5 bladed impeller for 300 rpm is presented in figure 4.1. It can be seen from the H-Q curve that the head of the impeller

Table 4.1: Performance parameters of a 5 bladed impeller at 300 rpm

H (m)	Q (m^3/s)	WHP (Watt)	BHP (Watt)	η (%)	Ψ'	ϕ'	n_s	Ds
0.183	0.00362	6.48	11.91	54.4	0.0454	0.0144	1.22	3.84
0.184	0.00359	6.49	11.83	54.9	0.0458	0.0143	1.20	3.87
0.191	0.00351	6.56	11.74	55.9	0.0474	0.0139	1.16	3.95
0.197	0.00341	6.58	11.40	57.7	0.0490	0.0136	1.12	4.04
0.206	0.00336	6.77	10.64	63.6	0.0511	0.0134	1.07	4.11
0.220	0.00323	7.00	10.91	64.1	0.0548	0.0129	1.00	4.26
0.244	0.00280	6.70	10.25	65.4	0.0606	0.0112	0.86	4.69
0.268	0.00256	6.72	10.16	66.1	0.0665	0.0102	0.77	5.03
0.290	0.00213	6.07	10.16	59.7	0.0721	0.0085	0.66	5.62
0.327	0.00158	5.09	8.22	61.9	0.0813	0.0063	0.52	6.72
0.351	0.00112	3.86	6.45	59.9	0.0872	0.0045	0.42	8.12
0.368	0.00061	2.22	4.69	47.3	0.0915	0.0024	0.29	11.124
0.366	0.00043	1.56	2.86	54.4	0.0911	0.0017	0.25	13.24

decreases when the flow rate is increased as expected. At this impeller speed, the BEP is about at 0.0026 m^3/s and 0.27 m. Efficiency of the 5 bladed impeller at BEP is about 66%. It is also apparent that the efficiency is low at low flow rates and approaches zero at the shut off condition. At very high flow rates, the impeller efficiency decreases when the flow rate is increased. In conclusion, the impeller performance agrees with the typical centrifugal pump performance which is shown in figure 1.4.

Overall performance results for the 5 bladed impeller at 300 rpm are presented in Table 4.1. It can be seen from Table 4.1 that at the design flow rate, the n_s, Ψ' and ϕ' are about 0.7, 0.06 and 0.010, respectively. In other words, this pump is categorized as radial pump close to mixed flow pump (see figure 1.7 and 4.4). There are two ways to make the pump closer to a low n_s centrifugal pump which would be narrowing the impeller width or making the outlet radius larger. However, since this study only focuses on the change of blade number in a centrifugal pump, there is no reason to manufacture another new impeller.

In order to understand the characteristics of the new designed impellers and the new experimental pump rig, measurements were conducted to validate the impellers similarity relations. The performance measurements are conducted at several impeller speeds which are 200, 300, 400 and 500 rpm for both of the impellers. The performance results of the 5 bladed impeller at several impeller speeds are presented in figure 4.2. As expected, increasing the impeller speed results in an increasing head and flow rate. Consequently,

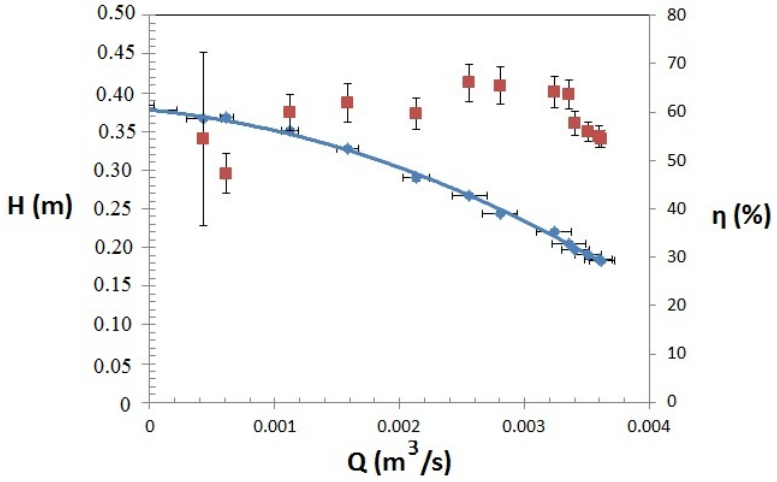

Figure 4.1: Head (⋄) and efficiency (□) curves for several flow rates of a 5 bladed impeller at 300 rpm

the power which is represented by WHP shown in figure 4.2 also increases. To validate the scaling relationship of a pump, the performance analysis was compiled in dimensionless analysis. Figure 4.3 shows plots of head coefficient (Ψ') and efficiency (η) to flow coefficient (ϕ'). The figure shows that all of the results lie in almost one line. Therefore, it can be concluded that the impeller follows the similarity laws. The maximum calculated efficiency was 65-66 %. The deviation of the efficiency value was believed because of the measurement error. The uncertainty of head, flow rate and efficiency at the design flow rate for the 5 bladed impeller at 300 rpm is about 1.1%, 5.4% and 5.8 % respectively. The uncertainty increases when the flow rate is decreased. The uncertainty of the head, flow rate and efficiency at 25% for the 5 bladed impeller at 300 rpm flow rate is about 0.7%, 32% and 32%. The high uncertainty at low flow rates had been expected because of high flow fluctuation at low flow rate. More details about uncertainty analysis which was stated and plotted in this chapter is discussed in Appendix B. The uncertainty is dominated by the flow measurement. It can be reduced by collecting more data but it will take much time. Because the uncertainty level in this study is still acceptable especially at high flow rates, there is no need to take more data.

To compare the new designed impellers to other impellers, it can be conducted by plotting the point of n_s and D_s at the design flow rate to the Cordier diagram. Figure 4.4 shows a plot of point n_s and D_s of the impellers in this study and other past research impellers from Altaf [3] and Pedersen [33]. It can be seen from figure 4.4 that even though the n_s of the new designed impeller is higher, D_s is also high. As a result, the plotted point

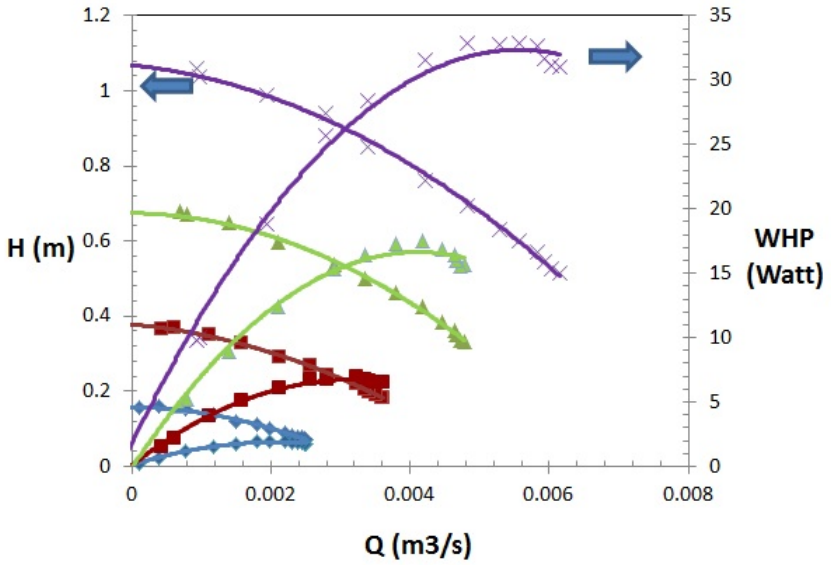

Figure 4.2: H-Q and WHP-Q Performance curves of a 5 bladed impeller at : × 500 rpm; △ 400 rpm; □ 300 rpm; ⋄ 200 rpm

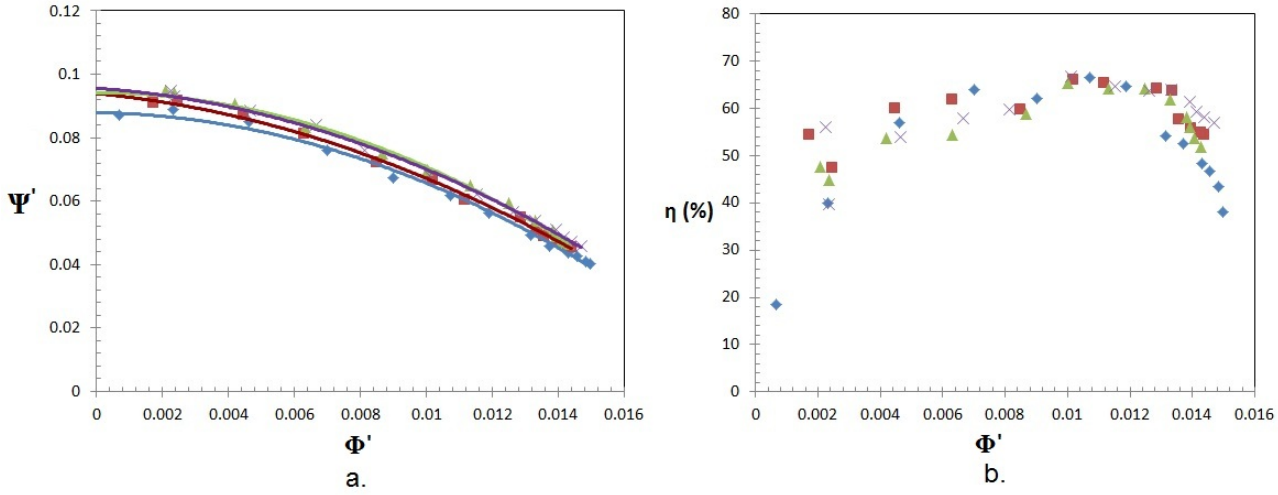

Figure 4.3: Ψ' - ϕ' and η - ϕ' performance curves of a 5 bladed impeller at : × 500 rpm; △ 400 rpm; □ 300 rpm; ⋄ 200 rpm

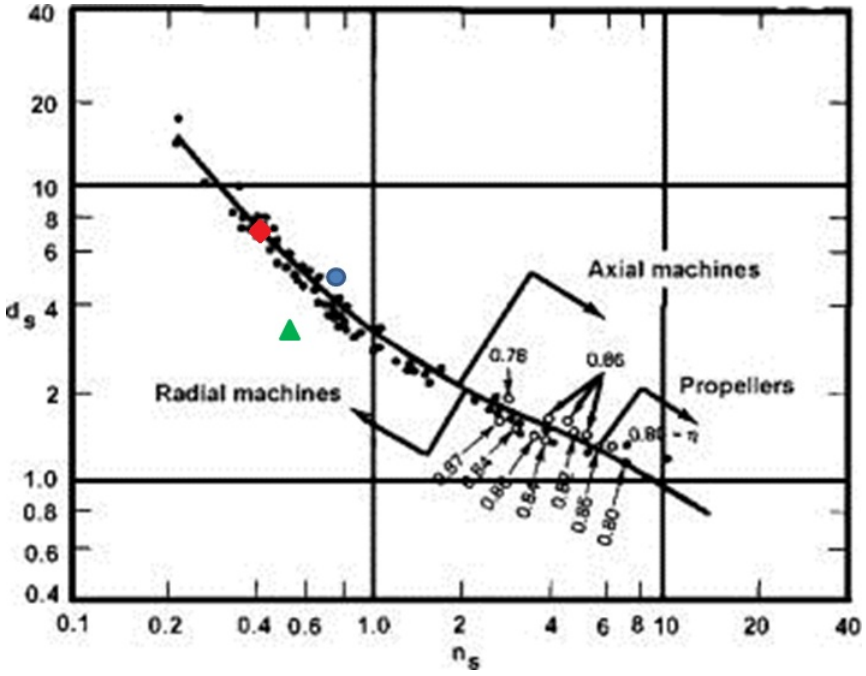

Figure 4.4: The Cordier diagram [5] and points of n_s and D_s in comparison with other impellers; ◇ Altaf [3]; △ Pedersen [33]; ○ This study

is still close to the Cordier curve. This is the reason that the impeller efficiency between this study and past impellers is not too different. The Altaf [3] designed impeller efficiency was about 64.8 % and Pedersen [33] designed impeller efficiency was about 58%.

Figure 4.5 shows the comparison of head and flow coefficient between the 5 and 7 bladed impellers. It can be seen that the head coefficient of the 5 bladed impeller is below the head coefficient curve of the 7 bladed impeller. This means that the fluid inside the 7 bladed impeller has higher energy transfer compared to the 5 bladed impeller. The results show similarity with past studies conducted by Varley [37], Houlin *et al.* [19] and Chakraborty and Pandev [7]. However, the maximum efficiency seems not to be significantly different between the 5 and 7 bladed impellers as shown in Table 4.2. The reason is that indeed the 7 bladed impeller transfers higher energy but the losses also seem to be higher. As a result, the 7 bladed impeller efficiency is about similar to the 5 bladed impeller. The other charts that show performance of the impellers are presented in Appendix B. It can be seen from the efficiency curves that at low flow rates, the 7 bladed impeller has a lower efficiency compared to the 5 bladed impeller at 300 rpm. It is believed to be caused by the 7 bladed impeller produces higher losses because it has a larger friction surface in contact

with the fluid. The losses will be discussed later in the PIV results which reveal the fluid behavior inside the impeller.

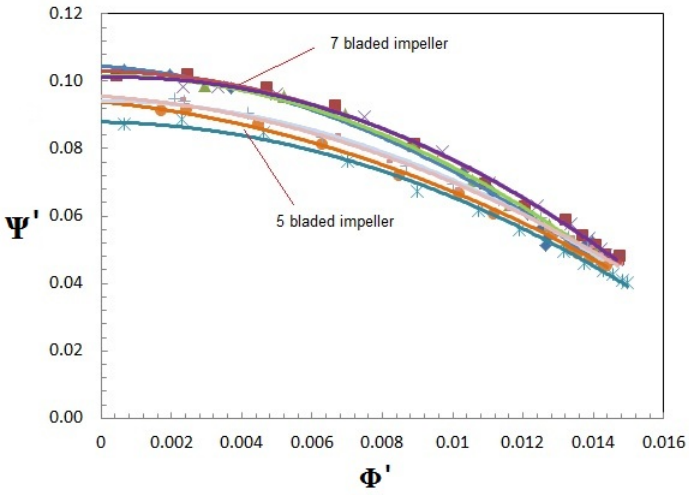

Figure 4.5: Ψ' - ϕ' performance curves of the 5 bladed impeller at : $\times$ 500 rpm; $\triangle$ 400 rpm; $\square$ 300 rpm; $\diamond$ 200 rpm and the 7 bladed impeller at :$-$ 500 rpm; $+$ 400 rpm; $\circ$ 300 rpm; $*$ 200 rpm

The plots of theoretical Euler, slip prediction and experiment head and flow coefficient (Ψ and ϕ) are presented in figure 4.6. The theoretical Euler plot are obtained when the blade was assumed infinite. Slip prediction plots of head and flow coefficient are obtained using equation 1.16. in addition, the slip prediction model was developed to predict finite blade impeller performance when pumping under inviscid flow conditions. It models that the fluid does not follow the blade curvature, as a result, the energy transfer which is represented by head reduces. Moreover, the experimental Ψ and ϕ results were lower compared to slip Ψ and ϕ prediction. This is caused by losses not modeled by slip including turbulence and friction losses as discussed in Chapter 1. The friction losses increase quadratically when the flow rate is increased [37][45]. In addition, the turbulence loss is minimum at the design flow rate and it increases when the flow rate is increased or decreased. The turbulence losses will be discussed later in the turbulence intensity subsection. It is also shown that the 7 bladed impeller has a higher head coefficient curve. It is because the 7 bladed impeller guides the fluid more from inlet to the impeller outlet so it results in a lower slip factor as implied in equation 1.15. Consequently, the absolute velocity in the tangential direction increases leading to the head impeller rise. Li [28] noted that numerically, the computed inviscid head of centrifugal pump was very close to the

head which was obtained using a slip prediction.

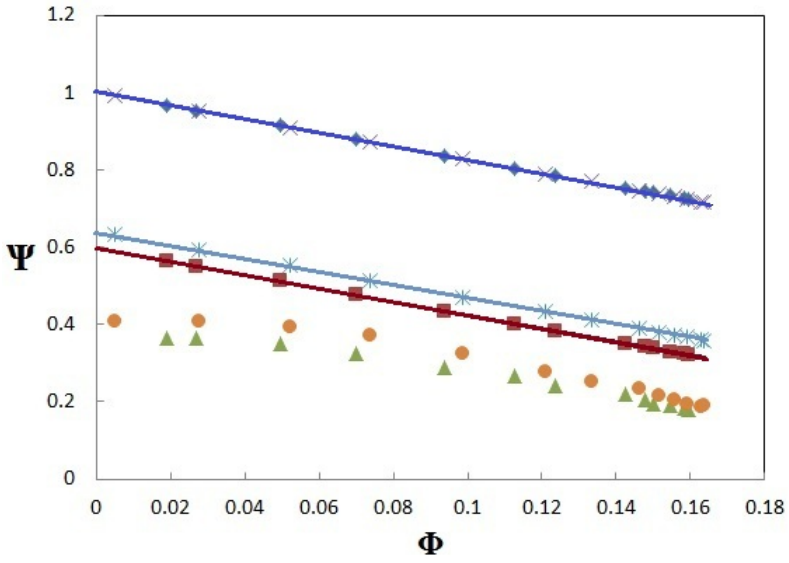

Figure 4.6: Comparison of theoretical Euler and slip with experimental results on head and flow coefficient curve; $\times$ 7 blades theoretical head; $\diamond$ 5 blades theoretical head; $*$ 7 blades slip model head; $\square$ 5 blades slip model head; $\square$ 7 blades experimental head; $\triangle$ 5 blades experimental head

4.1.2 Summary of performance results

In this study, an experiment to obtain the performance of the 5 and 7 bladed impellers was conducted. The results showed that the head increased when the flow rate was decreased which was identical to the performance of a backward curved pump impeller that is discussed in Chapter 1. Head, flow rate and efficiency at the design flow rate for a 5 bladed impeller at 300 rpm are 0.27 m, 0.0026 m^3/h and 66%, respectively. Head, flow rate and efficiency at the design flow rate for the 7 bladed impeller at 300 rpm are 0.28 m, 0.0026 m^3/h and 67%. This study also examined the performance data of the impeller at several impeller speeds to validate the results with the similarity laws. The results showed that experimental performance results agreed with the similarity laws.

Lastly, 5 and 7 bladed impellers had a similar characteristic performance to the typical centrifugal impeller. Both of the impellers agreed with the similarity laws. The results

showed that the plot of Ψ' - ϕ' and efficiency for several impeller speeds curves lay almost in one line. The 7 bladed impeller transfered higher energy to the fluid but it produced more losses which caused the efficiency between both of the designed impellers to be the same.

4.2 PIV results

4.2.1 Introduction

This section analyzes the flow behavior that was recorded through PIV measurements at several flow rates. Moreover, the comparison of flow structures between the 5 and 7 bladed impellers are discussed in this section. It has been mentioned that the results of PIV measurements were absolute velocity (**v**) in the vector map. Then, calculation is made to obtain the relative velocity (**W**) which was the velocity of the fluid inside the impeller. The relation between the absolute and relative velocity can be seen in equations that are presented in section 3.5.6. To understand the flow behavior of fluid inside the 5 and 7 bladed impellers at several flow rates, the flow streamlines, primary and secondary relative velocity profile, fluid angle deviation (β_d) and turbulence intensity (TI) will be discussed in this section.

4.2.2 Mass balance calculation

To evaluate the results of PIV measurements, a mass balance calculation was performed and compared to the results of ultrasonic flow rate measurements. In this study, the mass balance calculation was performed at the design flow rate of the 5 bladed impeller. The equation to obtain the flow rate can be

$$Q = ((W_r)_{average} \times A) \times 5 \text{ channels} \tag{4.1}$$

, where W_r is the fluid relative velocity in radial coordinate, A is the circumference area in a circular arc (R/R_2) which is the blade width (b) at R/R_2 multiply by 2π R.

The results can be seen in figure 4.7. The flow rates at $R/R_2 = 0.7$, $R/R_2 = 0.8$, $R/R_2 = 0.9$ are 0.002502 m^3/s, 0.002271 m^3/s and 0.002519 m^3/s, respectively. This means that the conservation mass of fluid flow inside the 5 bladed impeller is preserved. The ultrasonic flow meter at the design flow rate is 0.00256 m^3/s. The deviation flow rate between the PIV calculation and the ultrasonic flow rate measurement is about 2-11 % but

the uncertainty of flow rate using PIV measurements about 11 -13 %. Therefore, it can be concluded that the PIV measurements agrees with the ultrasonic flow rate measurements.

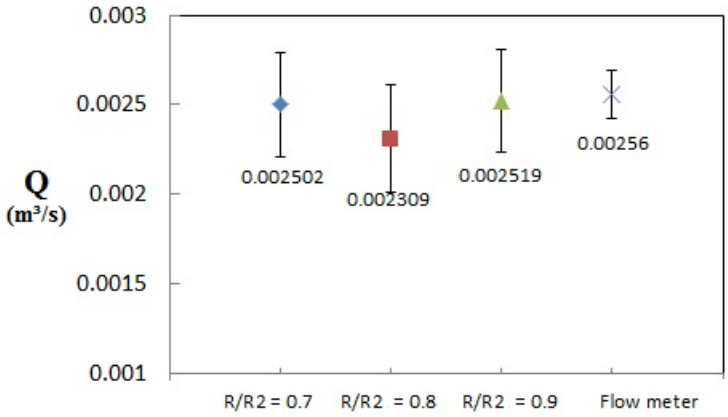

Figure 4.7: Comparison of flow rate calculation from PIV measurements at: $\diamond$ $R/R_2 = 0.7$, $\square$ $R/R_2 = 0.8$, $\triangle$ $R/R_2 = 0.9$ with ultrasonic flow meter ($\times$)

4.2.3 Flow behavior at the design and 75 % flow rates

Fluid flow streamlines at the design and 75 % flow rates

The streamlines throughout the passage at the design and 75% flow rates for the 5 and 7 bladed impellers using the averaged 1000 instantaneous images are presented in figure 4.8. The streamlines that are presented in this section are the results of images at position of a delay time (t_d) 15 ms for the 5 bladed impeller and 0 ms for the 7 bladed impeller. The other streamline results can be seen in Appendix C.

The fluid flow at the design flow rate for the 5 bladed impeller shows a well behaved flow structure as shown in figure 4.8a. There is no fluid separation that occurs at the inlet and outlet of the impeller. There is a small flow distortion at the middle of the passage but overall, the flow follows the blade curvature. When the flow is decreased to 75% flow rate, very small vortex appears on the blade pressure side (see figure 4.8b). The cause of the separation flow will be discussed in more detail later. Similar well behaved flow structures at the design flow rate were also found in experiments conducted by Altaf [3] and Pedersen [33] as shown in figures 2.11 and 2.9.

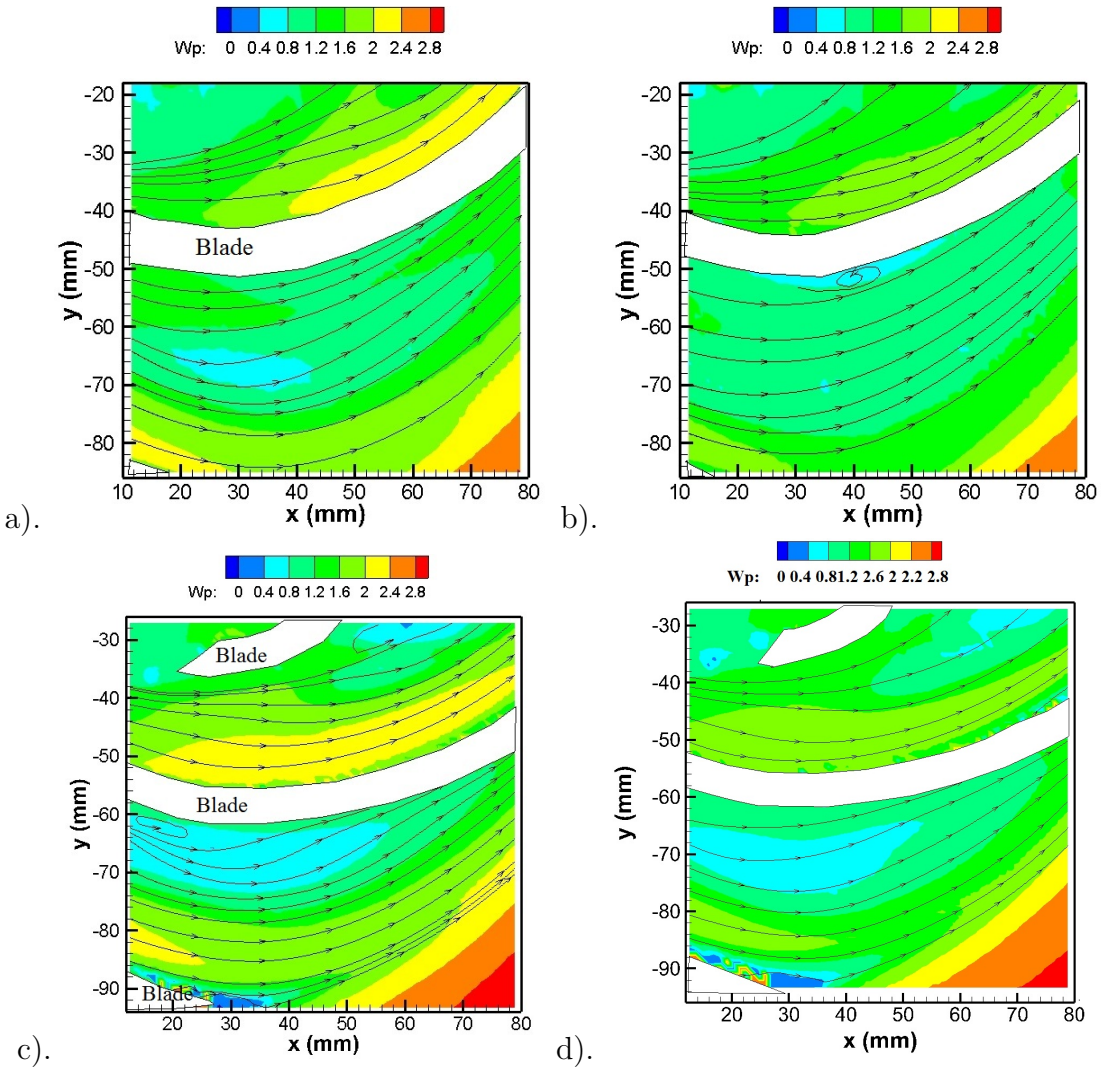

Figure 4.8: Fluid flow normalized streamlines at 300 rpmfor a) 5 bladed impeller 100% flow rate at t_d 15 ms, b) 5 bladed impeller 75% flow rate at t_d 15 ms, c) 7 bladed impeller 100% flow rate at t_d 0 ms, d) 7 bladed impeller 75% flow rate at t_d 0 ms

For the 7 bladed impeller, separation flow occurs on the blade pressure side near the impeller inlet. The separation flow might be caused by the high inlet velocity and high fluid 'angle of attack'. Detailed discussion about separation flow at the blade pressure side of the 7 bladed impeller will be presented later. A similar flow structure to this study was found in an experiment conducted by Keller [23]. Figure 4.9c shows that at the design flow rate, a separation flow also appears on the blade pressure side where the low relative velocity is attached.

Pictures of the normalized mean relative velocity contour to tip blade velocity (W/u_2) at the design flow rate are presented in figure 4.9. The current study and past studies conducted by Pedersen [33], Westra [43] and Keller [23] show that the high magnitude of fluid relative velocity lies from inlet of the blade suction side and it ends at the impeller outlet of the blade pressure side. In addition, all of the results show that a low magnitude relative velocity attaches the blade pressure side except for the 5 bladed impeller in this study. The number of blades applied in Keller [23], Westra [43] and Pedersen [33] was 6 blades. It can be implied that from the perspectives of streamlines and relative velocity results, the number of blades influences the fluid behavior inside the passage of the impeller.

Mean normalized primary and secondary velocity at Design and 75 % flow rates

The dimensionless parameter, mean primary relative velocity to outlet rotational impeller velocity (W_p/u_2) for the 5 and 7 bladed impellers at the design flow rate are presented in figures 4.10a and 4.10c, respectively. Generally, it can be seen that the mean normalized W_p increases from the blade pressure side to the blade suction side especially at the inlet of the impeller (R/R_2 = 0.5, 0.6 and 0.7). Hence, as explained in Chapter 1, the flow structure follows the potential flow theory at the impeller inlet. The potential flow pattern at the inlet can be seen in figure 4.11a. The potential flow then becomes distorted as the flow moves toward the impeller outlet as shown in figure 4.11b. The flow close to the impeller exit disagrees with the potential flow theory; the value of W_p decreases from the blade suction side, a reaching minimum at the middle of the passages before increasing again to the blade pressure side (R/R_2 = 0.8 and 0.9). It can be shown that a small jet is created on the blade pressure side at the impeller exit. The small jet pattern in this study can be seen in the velocity profile presented in figure 4.11c. However, no wake is found at the blade suction side because the fluid still has high W_p magnitude.

Similar fluid relative velocity pattern that follows the potential theory at the impeller inlet but then, the potential flow pattern diminishes at the impeller exit was found in experiments conducted by Murakami *et al.* [32], Hesse and Howard [18], Pedersen [33],

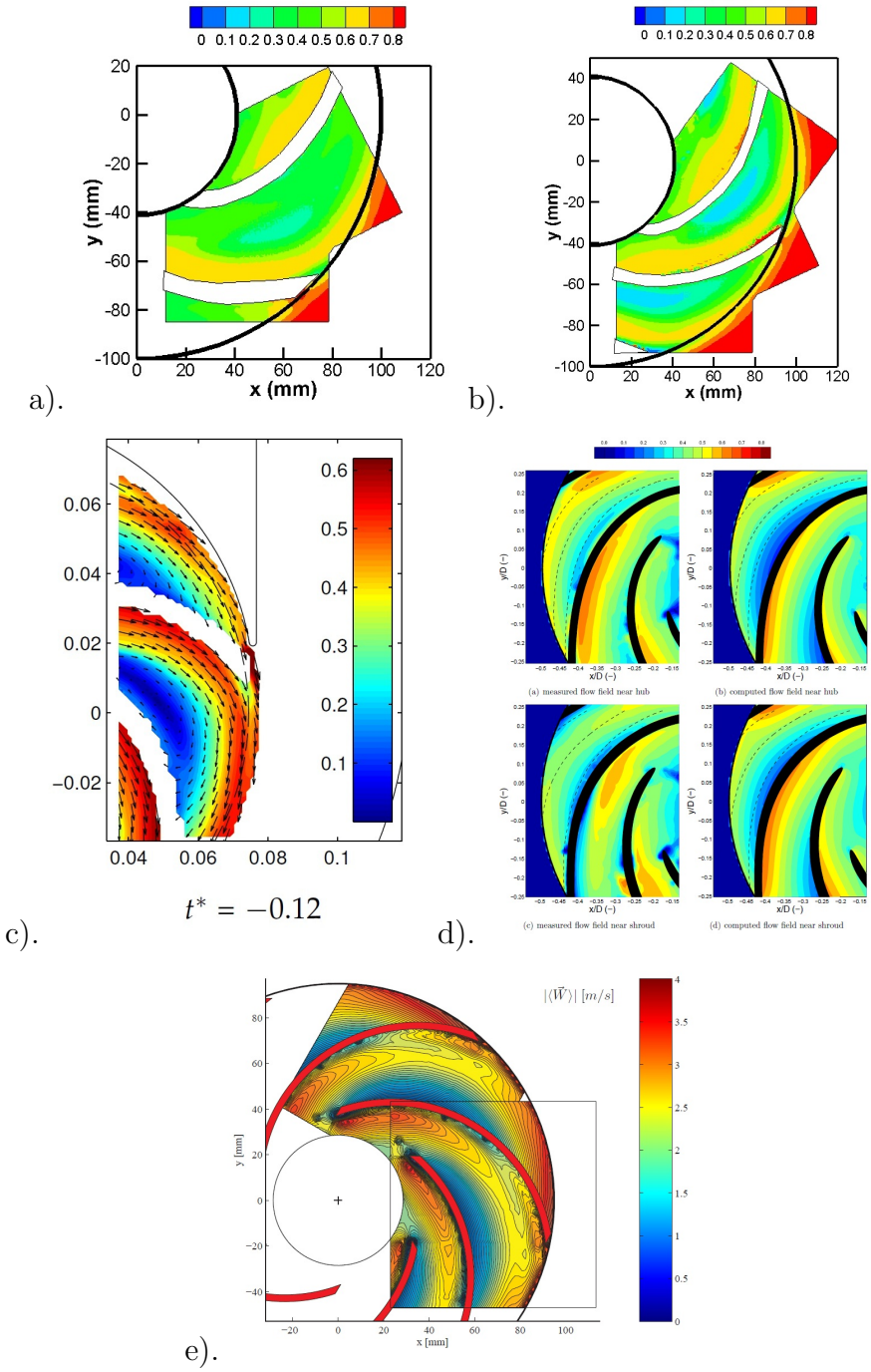

Figure 4.9: Normalized mean relative velocity contour to impeller tip speed at the design flow rate for a) 5 bladed impeller, b) 7 bladed impeller c) Keller [24], d) Westra [44], e) Pedersen [33]

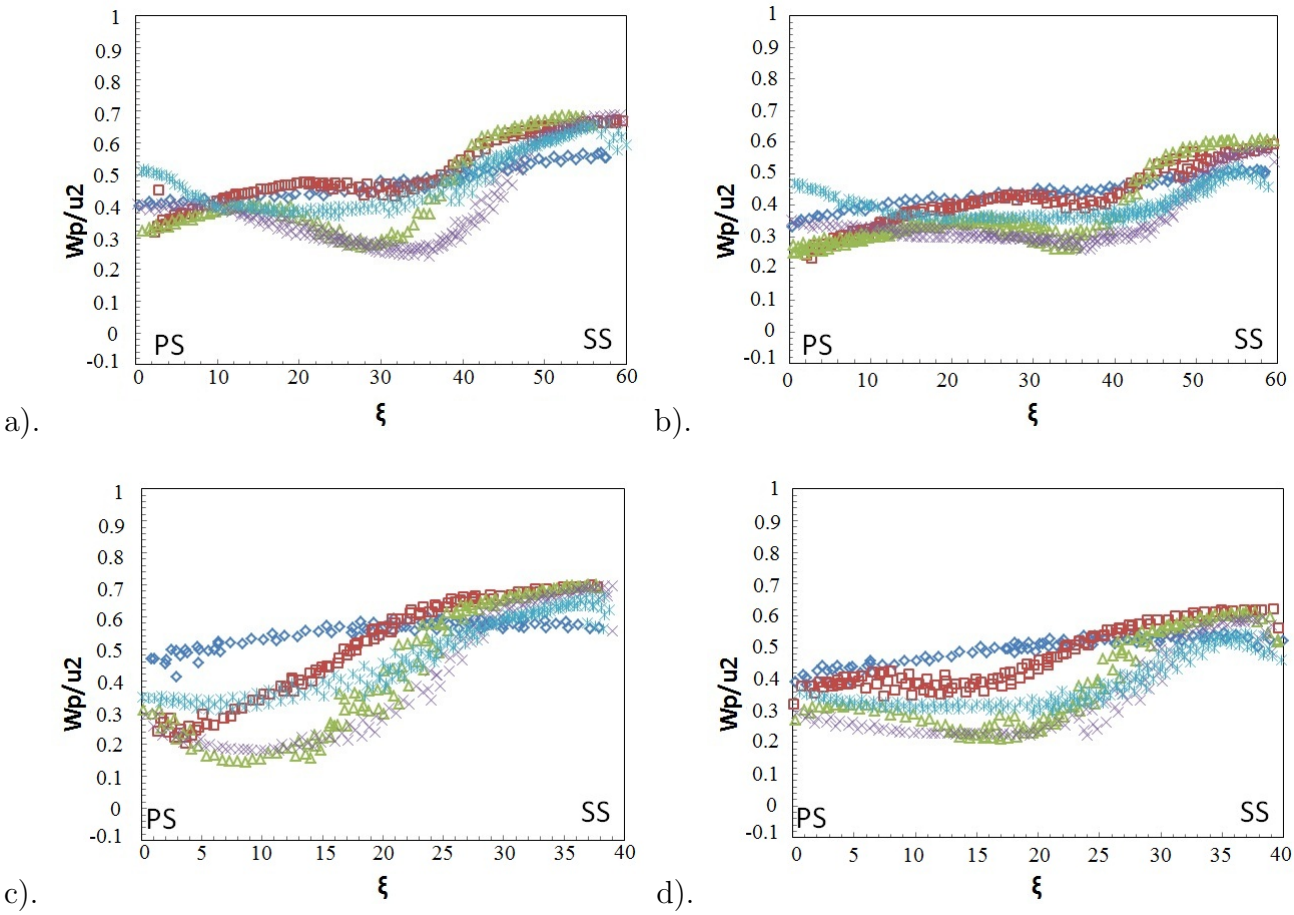

Figure 4.10: Mean normalized primary velocity at : $\diamond$ $R/R_2 = 0.5$; $\square$ $R/R_2 = 0.6$; $\triangle$ $R/R_2 = 0.7$; $\times$ $R/R_2 = 0.8$; $*$ $R/R_2 = 0.9$ for a) 5 bladed impeller 100% flow rate, b) 5 bladed impeller 75% flow rate, c) 7 bladed impeller 100% flow rate, d) 7 bladed impeller 75% flow rate

Westra *et al.* [44] and Keller [23]. Figure 1.18 shows velocity profile of fluid inside the 3 and 7 bladed impellers obtained by Murakami *et al.* [32]. It shows that close to the impeller inlet, the highest velocity occurs at the blade suction side, but close to the impeller exit, the velocity increases from the blade suction side to the blade pressure side. Figure 4.11 shows plots of mean normalized radial velocity obtained by Pedersen [33]. It shows that at the inlet ($R/R_2 = 0.5$, figure 4.11d), the relative velocity pattern agrees with the potential flow but the pattern changes when the flow moves toward the impeller exit ($R/R_2 = 0.98$, figure 4.11f). Pedersen *et al.* [34] mentioned that the increase of the relative velocity toward the blade pressure side near the impeller exit is caused by the Coriolis force. The illustration of the Coriolis force that is developed from the 2D analysis force balance of fluid inside the impeller passage is shown in figure 1.11. In addition, past studies also explained that the potential flow weakened when the fluid moves toward the impeller exit because of a rapidly growing boundary layer at the suction side of the impeller[18][32].

More detail observation is carried out of the fluid behavior close to the blade suction and pressure sides. On the blade suction side, the fluid velocity increases from the inlet before it decreases near the impeller exit. In comparison, on the blade pressure side, the fluid velocity decreases at the impeller inlet but then, it increases when the fluid moves toward the impeller outlet. Close to the impeller inlet, the centrifugal force seems dominantly influenced on the fluid near the blade suction side. As implied in equation 1.17, the centrifugal force has an important role in the velocity increase. The fluid on the blade pressure side seems to be more influenced by viscous effect, counter rotating flow and passage geometry. The illustration of counter rotating flow is shown in figure 1.12a. Close to the impeller exit, the fluid appears to be more influenced by Coriolis effect. When the fluid flows toward the exit, the relative velocity increases causing the Coriolis force to increase as implied in equation 1.18. As a result the fluid velocity close the blade pressure side increases and the fluid velocity close to the blade suction side decreases. At the design flow rate, the magnitude of the mean normalized W_p is high and far from the zero value. Therefore, it can be concluded that the fluid dominantly flows toward the exit of the impeller.

The dimensionless parameter, mean primary relative velocity to outlet rotational impeller velocity (W_p/u_2) for the 5 and 7 bladed impellers at 75% flow rate are presented in figures 4.10b and 4.10d, respectively. Generally, the pattern of W_p is similar to the design flow rate; the magnitude of W_p increases from the blade pressure side to the blade suction side near the impeller inlet, but at the impeller exit, the value of W_p decreases from the blade suction side, reaching a minimum value before increasing again at the blade pressure side. Similar to the design flow rate, a small jet is found at the impeller outlet of the blade pressure side. Close to the impeller exit ($R/R_2 = 0.8$ and 0.9), the minimum value of W_p

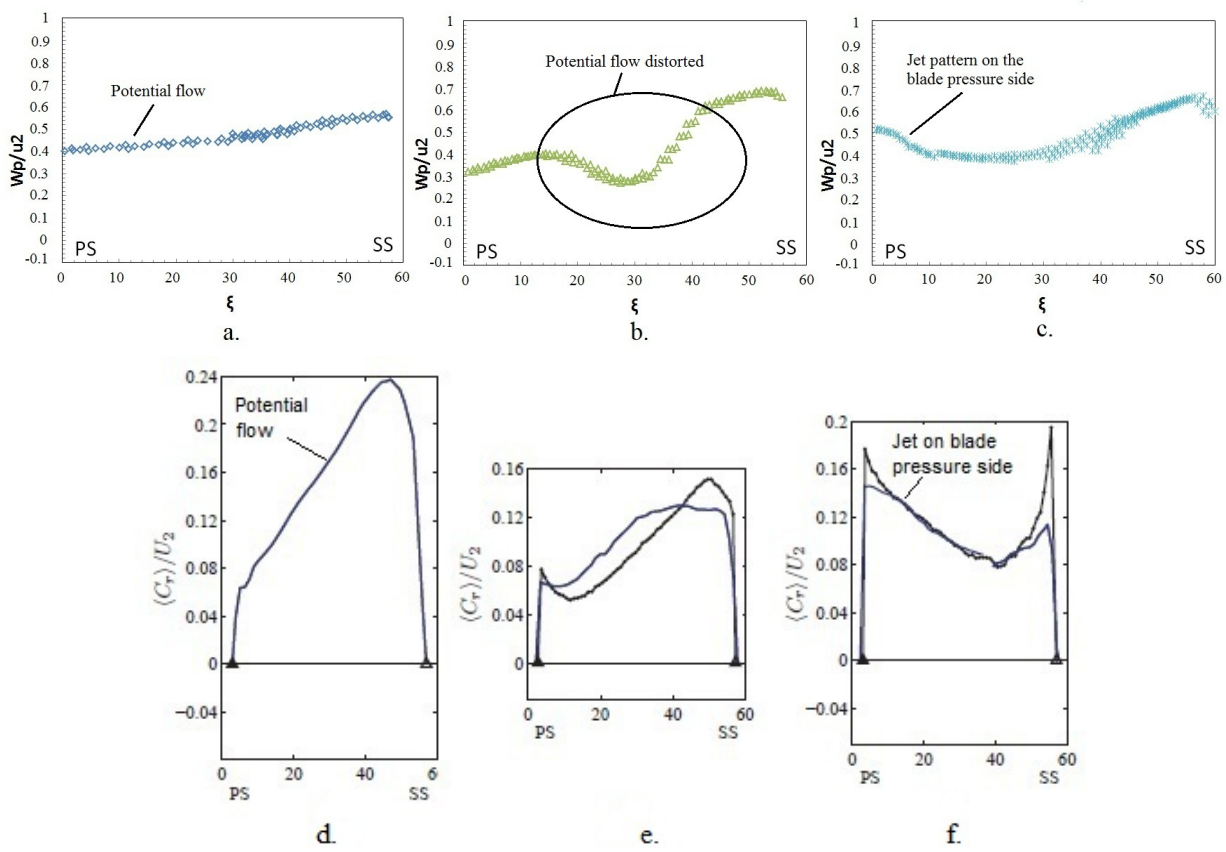

Figure 4.11: Current study primary velocity results at the design flow rate at a) R/R_2 0.5; b)R/R_2 0.7; c) R/R_2 0.9 and radial velocity obtained by LDV (black line) and PIV (blue line) from Pedersen [33] at the design flow rate for d) R/R_2 0.5; e)R/R_2 0.75; f) R/R_2 0.98

falls earlier compared to the design flow rate and a small jet at the blade pressure side becomes stronger at 75% flow rate. It is probably caused by the decrease of the fluid momentum when the flow rate is decreased so the boundary layer growth might start earlier. The decrease of the fluid momentum also is probably the reason that separation flow on the blade pressure side occurs which is also shown in the streamlines subsection.

The mean normalized secondary relative velocity to outlet rotational impeller velocity (W_s/u_2) for the 5 and 7 bladed impellers at the design flow rate are presented in figures 4.12a and 4.12c. The magnitude of mean normalized W_s for the fluid on the blade suction and pressure sides along the passage are very low (close to zero) compared to the magnitude of W_p so that close to the blade suction and pressure sides, the primary flow is dominant

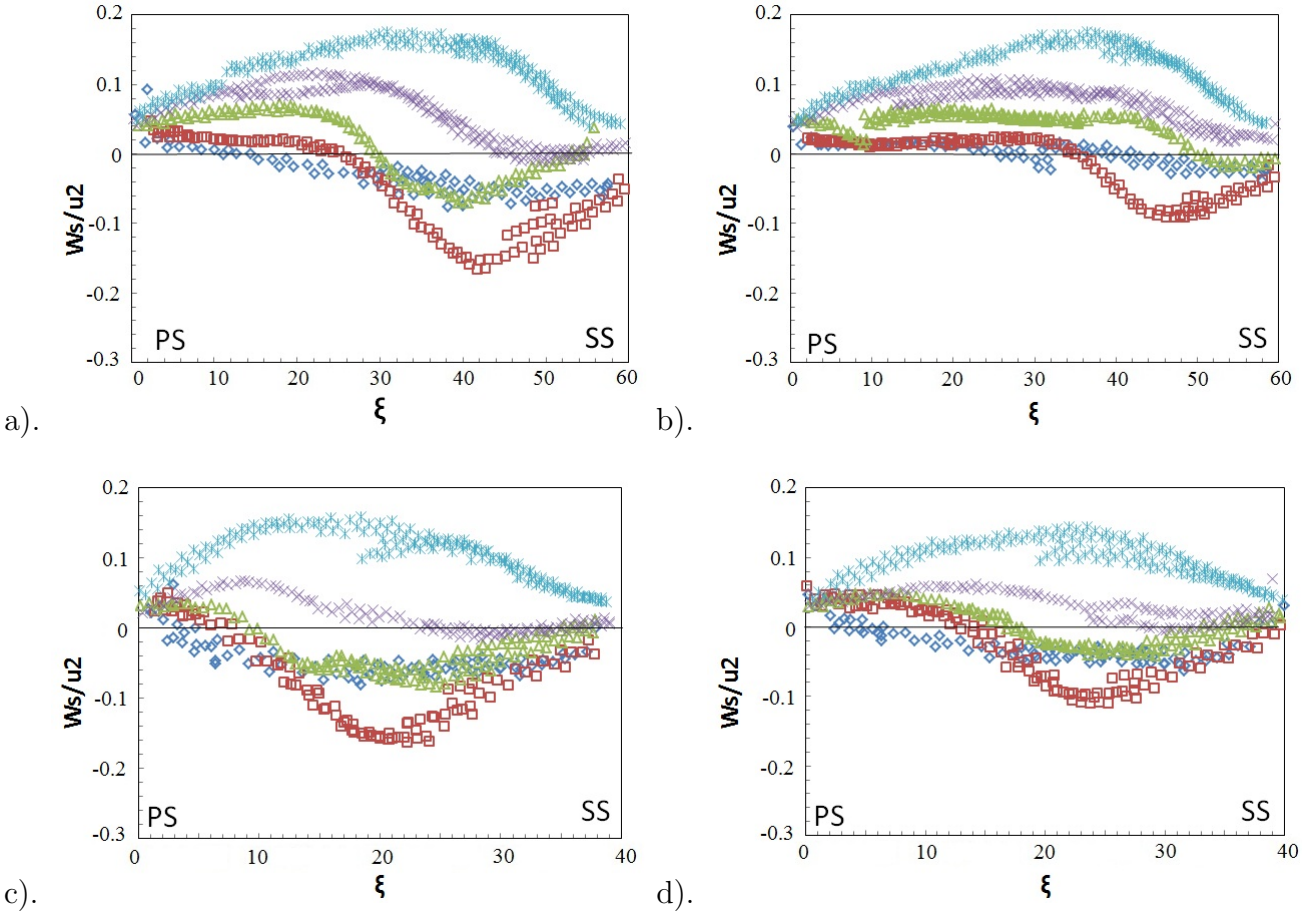

Figure 4.12: Mean normalized secondary velocity at : $\diamond$ $R/R_2 = 0.5$; $\square$ $R/R_2 = 0.6$; $\triangle$ $R/R_2 = 0.7$; $\times$ $R/R_2 = 0.8$; $*$ $R/R_2 = 0.9$ for a) 5 bladed impeller 100% flow rate, b) 5 bladed impeller 75% flow rate, c) 7 bladed impeller 100% flow rate, d) 7 bladed impeller 75% flow rate

over the secondary flow. However, at the middle of the passage, the influence of secondary flow becomes stronger. This is similar to the results obtained by Hesse and Howard [18] as shown in figures 1.19 c and d. The magnitude of the W_s is negative near the inlet which means that the fluid flow tends to move toward the blade suction side but it is positive at the outlet which means that the flow tends to move toward the blade pressure side. A similar W_s pattern to this study is found in experiments conducted by Altaf [3] and Hesse and Howard [18] and it is also found in an experiment inside the 3 bladed impeller conducted by Murakami *et al.* [32]. Figure 4.13 shows mean normalized secondary relative velocity obtained by Altaf [3]. It should be noted that in Altaf [3] and Hesse and Howard [18], if the W_s has a positive value, the flow tends to flow toward the blade suction side and vice versa. In this study, as discussed in section 3.5.6, if the W_s has a positive value, the flow tends to move toward the blade pressure side and vice versa. Hence, from the W_s perspective, it agrees with the potential flow theory that flow experiences a counter rotating effect. Figure 1.12a shows that at the inlet, the flow moves toward the blade suction side but close the exit the flow moves toward the blade pressure side. Similar to the results obtained by Murakami *et al.* [32] , the secondary flow in the middle of the passage (R/R = 0.7 and 0.8) has less influence on the flow structure.

The dimensionless parameter, mean secondary relative velocity to outlet rotational impeller velocity (W_s/u_2) for the 5 and 7 bladed impellers at 75 % flow rate are presented in figures 4.12b and 4.12d. The magnitude of W_s near the exit of the impeller is lower compared to the design flow rate but near the impeller inlet it is higher. This pattern is similar to Altaf [3] results as shown in figure 4.13. At the inlet, it seems that the influence of the inlet bulk flow decreases so it causes the W_s to increase at the inlet of the impeller. At the impeller outlet, the decrease of W_s might be caused by the decrease of the fluid momentum.

The magnitude of W_p and W_s at the design and 75% flow rates increases along the passage. Even though the area of the impeller expands from the impeller inlet to the impeller outlet, the energy transfer from the impeller to the fluid is large enough so that it causes an increase in energy transfer. The increase of the fluid velocity along the impeller passage has been mentioned and discussed in Chapter 1 (see figure 1.3) [37]. The results also show that generally, the magnitude of W at 75% flow rate decreases compared to the magnitude of W at the design flow rate. The average of W at the design flow rate is about 1.6 m/s whereas at the 75% flow rate, the average of W is about 1.4 m/s. Since the relative velocity decreases, based on the energy equations, the head increases [15]. The head rise calculation was performed to validate the performance results shown in figure 4.1. The equation 1.2 is applied to calculate the head rise. The assumptions used in the calculation are the inlet flow was uniform and it was not influenced by swirl flow so the

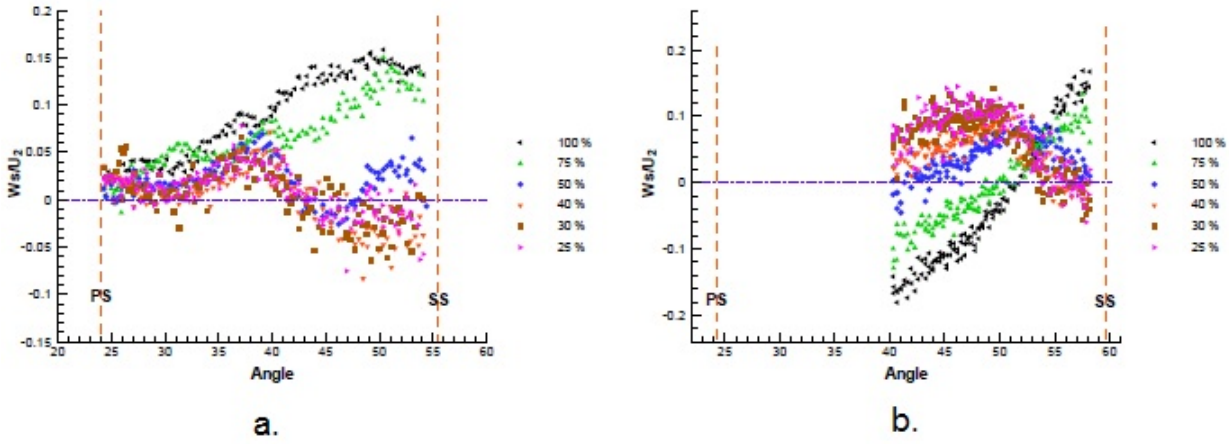

Figure 4.13: Mean normalized secondary velocity at the design flow from Altaf [3] of a) the inlet of the impeller; b) the outlet of the impeller

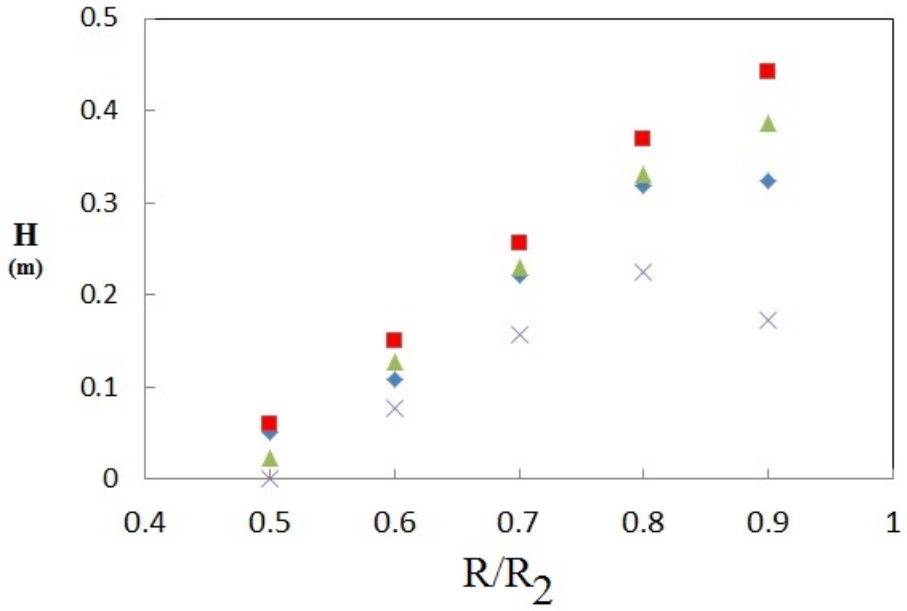

Figure 4.14: Comparison of the head rise of fluid inside the 5 bladed impeller at: $\diamond$ = design flow rate; $\triangle$ = 75% flow rate; $\times$ = 140% flow rate and the 7 bladed impeller at the design flow rate ($\square$)

inlet absolute velocity in the tangential direction ($v_{\theta 1}$) is assumed negligible. The head rise calculation was expected to be higher than the performance measurements because of the assumptions. The results of the head rise calculation is presented in figure 4.14. It shows that the head rise at 75% flow rate is higher than the head rise at the design flow rate. Therefore, the PIV results agree with the performance results.

Comparison of W_p and W_s at the design and 75 % flow rates between the 5 and 7 bladed impellers

PIV measurements were conducted to reveal the flow structure differences between the 5 and 7 bladed impellers. At the design and 75 % flow rates, the flow structure differences inside the passage of the 5 and 7 bladed impellers have already been shown. Generally, the magnitude and pattern of W_s are similar. The differences are clearly shown when comparing the value of W_p.

At the region close to the impeller inlet (R/R_2= 0.5 and 0.6), the magnitude of W_p for the 7 bladed impeller is higher than the 5 bladed impeller as shown in figure 4.15. This is probably caused by the effect of the passage geometry. The model passage geometry of the 5 and 7 bladed impellers can be seen in figure 4.16. The 2θ which is the angle of diffuser of the 7 bladed impeller is 25.6^o whereas the 2θ of the 5 bladed impeller is 36.5^o. Hence, the 7 bladed impeller has a narrower passage compared to the 5 bladed impeller. The larger angle diffuser experiences higher flow losses because it produces higher adverse pressure gradient [45].

The results also showed that the fluid velocity at the blade pressure side close to the impeller exit inside the 5 bladed impeller is higher than the fluid velocity of the 7 bladed impeller. This means that a small jet which is found on the blade pressure side inside the 5 bladed impeller is stronger compared to the jet pattern inside the 7 bladed impeller. This is also probably because of the passage geometry. Numerical research conducted by Houlin *et al.* [19] also found that a jet pattern will strengthen if the number of the blades is decreased.

At the design and 75% flow rates, the magnitude of W_p on the blade suction side along the passage is similar between 5 and 7 bladed impellers. However, on the blade pressure side, the magnitude of W_p for the 7 bladed impeller is lower than for the 5 bladed impeller. Hence, the blade loading that is described in Chapter 1 of the 7 bladed impeller appears to be higher than the blade loading of the 5 bladed impeller. This means energy transfer to the fluid for the 7 bladed impeller is higher than the 5 bladed impeller [1]. The head

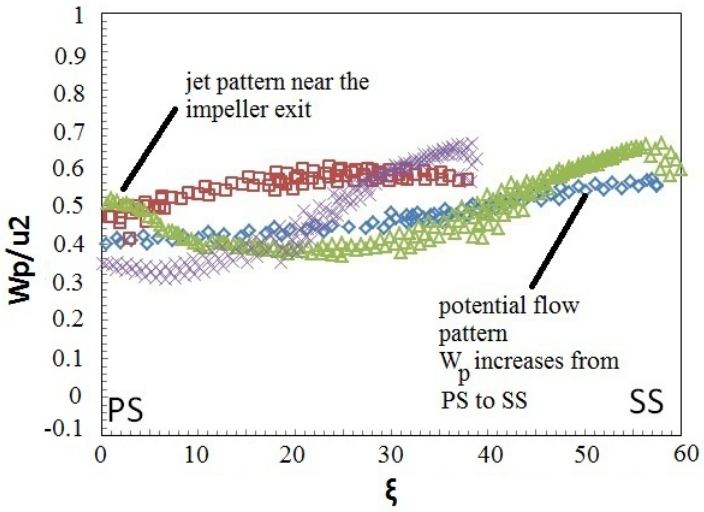

Figure 4.15: Comparison of mean normalized primary velocity between the 5 and 7 bladed impellers at the design flow rate obtained. $\diamond$ 5 bladed impeller at $R/R_2 = 0.5$; $\square$ 7 bladed impeller at $R/R_2 = 0.5$; $\triangle$ 5 bladed impeller at $R/R_2 = 0.9$; $\times$ 7 bladed impeller at $R/R_2 = 0.9$

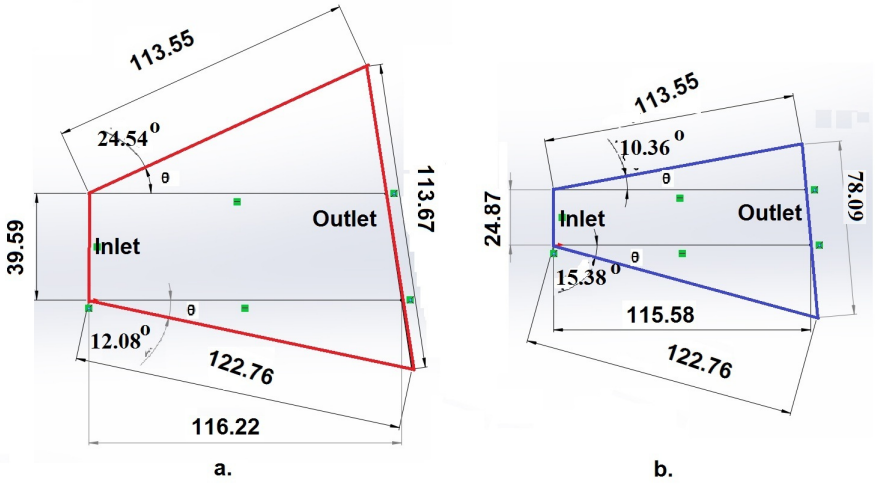

Figure 4.16: Comparison of passage geometry between: a. 5 bladed impeller and b. 7 bladed impeller

rise calculation results shown in figure 4.14 confirm that the fluid head rise of the 7 bladed impeller is higher than the fluid head rise of the 5 bladed impeller.

Turbulence intensity (TI) at the design and 75 % flow rates

Turbulence intensity (TI), defined in section 3.5.8, contours at the design and 75% flow rates for the 5 and 7 bladed impellers are presented in figure 4.17. Generally, when the flow is decreased from the design to 75% flow rate, the magnitude of TI in the impeller passage increases. The average TI of the 5 bladed impeller at the design flow rate is about 0.108 whereas the average TI at 75% flow rate is about 0.131. The flow that has higher magnitude of TI appears to experience higher turbulence losses. Hence, this result agrees with the centrifugal pump losses theory that is shown in figure 1.8. Figure 1.8 shows that the minimum turbulunce losses occurs at the design flow rate. At the design flow rate, a low magnitude contour turbulence intensity line is covering a whole passage. However at 75% flow rate, the low magnitude contour line of TI lies from inlet and stops at the end of the blade suction side. This is probably at 75% flow rate, the fluid momentum decreases because the fluid velocity decreases so that it makes the fluid fluctuation increase.

The differences between the 5 and 7 bladed impellers are clearly shown in the TI contour map. For the 5 bladed impeller, the low magnitude contour TI line attaches to both the blade suction and blade pressure side. However, for the 7 bladed impeller the low magnitude contour TI line only attaches at the blade suction side and high magnitude TI attaches the blade pressure side. The high magnitude TI is probably caused by separation flow occurs on the blade pressure side of the 7 bladed impeller as shown in the streamline subsection. The separation flow is probably due to the high inlet velocity of fluid inside the 7 bladed impeller. The high inlet velocity might cause a higher inlet flow angle. In this study, inlet flow angle (α) will be noted as 'angle of attack' of the fluid to the blade pressure side. The illustration of inlet fluid flow angle that is developed from the velocity triangle model at the inlet of a centrifugal pump shown in figure 1.6 can be seen in figure 4.18. It can be inferred from figure 4.18 that since the impeller rotation speed (u_1) and the inlet blade angle (β) are constant, the inlet fluid angle increases if the inlet velocity increases. The blade pressure side of the impeller has a shape similar to the upper surface of an airfoil that has high adverse pressure gradient around the leading edge and the adverse pressure gradient reduces as the fluid moves toward the trailing edge. The increase of 'angle of attack' causes the adverse pressure gradient to be stronger [45]. It appears that the fluid at the inlet of the 7 bladed impeller does not resist the high adverse pressure gradient so the fluid separates from the blade pressure side. Figure 4.19c showing a plot of the fluid angle deviation (β_d) of the 7 bladed impeller confirms that the fluid has relatively high

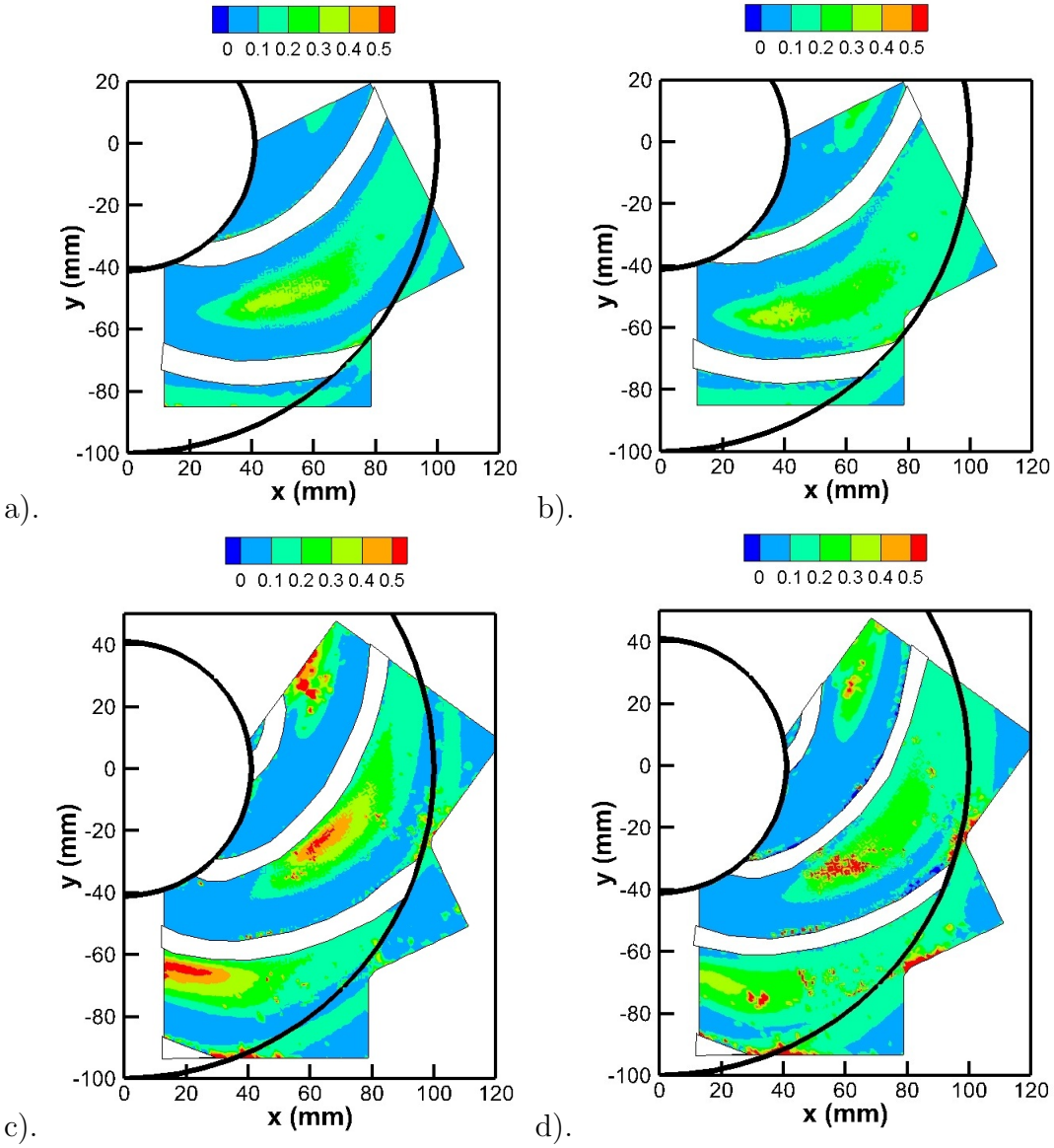

Figure 4.17: Fluid flow turbulence intensity inside the impeller passage for a) 5 bladed impeller 100% flow rate, b) 5 bladed impeller 75% flow rate, c) 7 bladed impeller 100% flow rate, d) 7 bladed impeller 75% flow rate

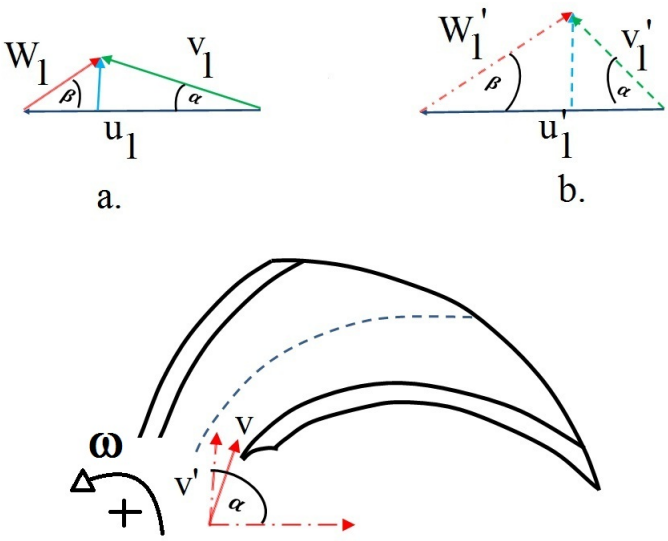

Figure 4.18: The influence of inlet fluid velocity on the fluid angle at the impeller inlet, a) low velocity; b) high velocity

'angle of attack' at the inlet close to the blade pressure side (marked in a little box).

The average magnitude TI of a passage inside the 7 bladed impeller is about 0.129. The TI of the fluid inside the 7 bladed impeller is higher than the 5 bladed impeller which has average TI of 0.108. The high TI of the 7 bladed impeller is probably caused by fluid separation on the blade pressure side. Consequently, the fluid inside the passage of the 7 bladed impeller near the blade pressure side fluctuates more and it has higher head rise. Separation flow might be prevented by narrowing the blade curvature (β). Consequently, the 'angle of attack' (α) becomes smaller as implied in figure 4.18. However, Li [26] in his study, reported that larger blade angle caused an increase in skin friction which is part of the hydraulic losses. In order to achieve best performance, optimization of blade numbers and blade curvature should be performed.

Fluid angle deviation (β_d) at the design and 75 % flow rates

Figures of fluid angle deviation (β_d), defined in section 3.5.8, at the design and 75% flow rates for the 5 and 7 bladed impellers are presented in figure 4.19. At the inlet region, relatively high β_d is concentrated on the blade suction side. Similar patterns of the fluid

angle deviation are found in the experiments conducted by Altaf [3] shown in figure 4.20a and Pedersen [33] shown in figure 4.20b. Pedersen [33] and Altaf [3] explained that the relatively high fluid angle deviation at the inlet was caused by the influence of the switching flow from axial entry flow to rotary flow creating swirl or bulk flow. Inlet flow naturally enters the passage and attaches the low pressure side which is on the blade suction side. When the flow decreases to 75% flow rate, the relatively high fluid angle deviation weakens. It is probably caused by the influence of the bulk flow decrease.

In figure 4.19, a zero contour of β_d that is marked on each β_d map crosses the impeller passage from the blade suction side to the blade pressure side. The zero contour lines is a separation line between the loading (inner part) and the unloading (outer part) of the blade [33]. Pedersen [33] explained that in the blade loading region, the velocity slip is not a significant influence on the flow. Pedersen [33] named the region as a 'true channel' region. On the other hand, at the outer part, the velocity slip becomes important. It is shown that as the flow is decreased to 75% flow rate the inner region reduces from about 25% area of the passage to 12% area of the passage. At 75% flow rate, the unloading part region is wider than the design flow rate so it appears that the fluid experiences higher slip losses. This confirms the theory that is shown in figure 1.8. The figure shows that as the flow rate is decreased, the slip losses region increases.

Westra [43], in his results, presented the absolute fluid flow angle (β_r) instead of fluid angle deviation (β_d) because along the passage, the blade angle was different as a result of the blade angle optimization [43]. Therefore, it is difficult to obtain the value of fluid flow angle deviation. The results are presented in figure 4.20c. The results show that at the inlet, generally, the magnitude of absolute flow angle is higher than the computed inviscid model which inferred that the flow tends toward the blade suction side. In comparison, at the exit, the flow angle is lower than the computed inviscid model which inferred that the flow tends to move toward the blade pressure side. Therefore, the result is similar to the results of this study and other past studies [3][33].

The contour map of β_d shows some differences between the 5 and 7 bladed impellers. For the 7 bladed impeller, the positive high deviation β_d lies starting from the blade suction side to the blade pressure side at the impeller inlet. In comparison, the positive high deviation β_d for the 5 bladed impeller lies only from the inlet blade suction side to the middle of the passage. It appears that inside the 7 bladed impeller, the fluid flow is more influenced by the bulk inlet flow.

The 'true channel' of the 7 bladed impeller at the design flow rate is about 38% of the area of the passage whereas as mentioned previously, the 'true channel' of the 5 bladed is about 25% area of the passage. Hence, the 'true channel' area of the 7 bladed impeller is

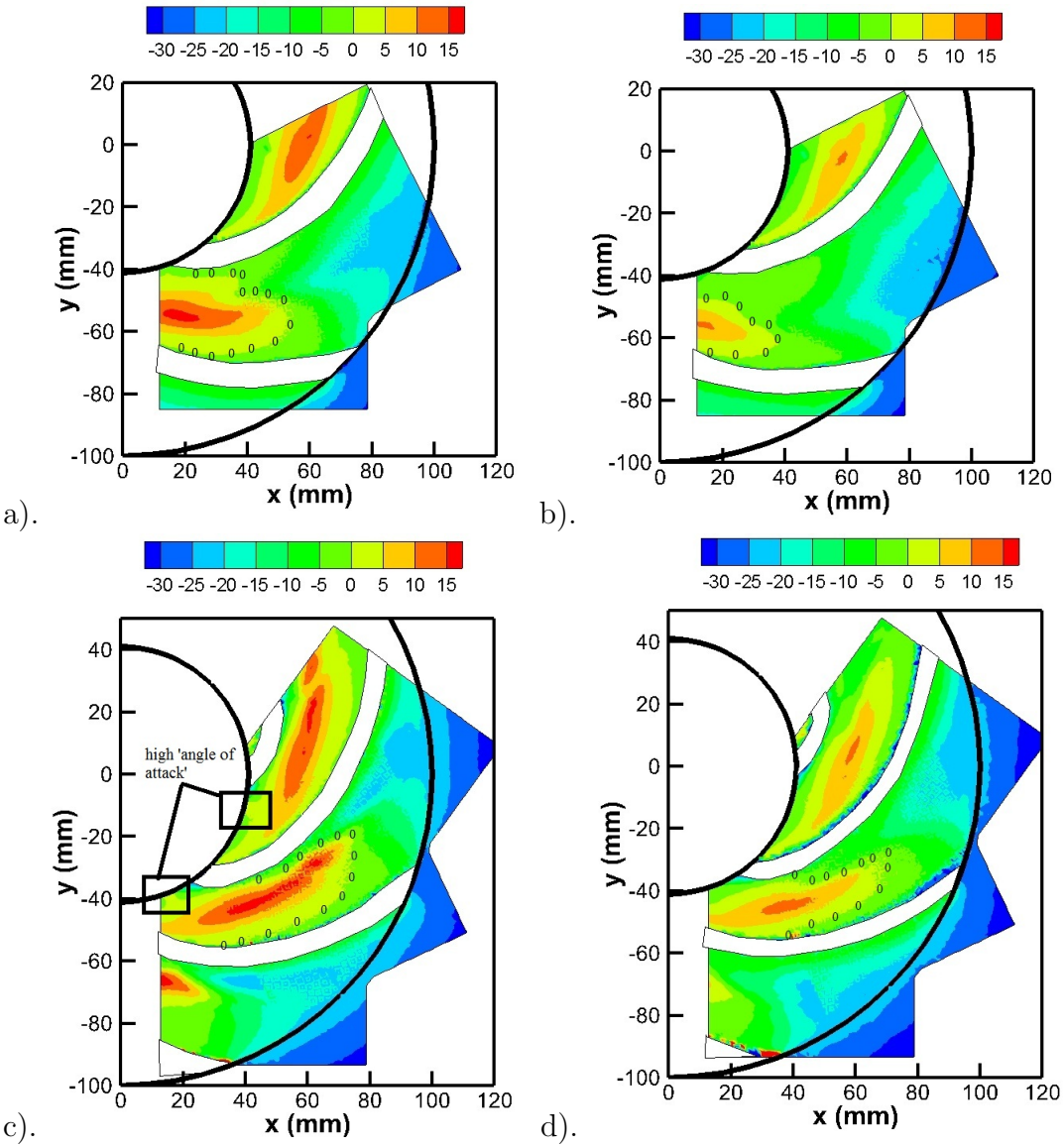

Figure 4.19: Fluid angle deviation in the impeller passage for a) 5 bladed impeller 100% flow rate, b) 5 bladed impeller 75% flow rate, c) 7 bladed impeller 100% flow rate, d) 7 bladed impeller 75% flow rate

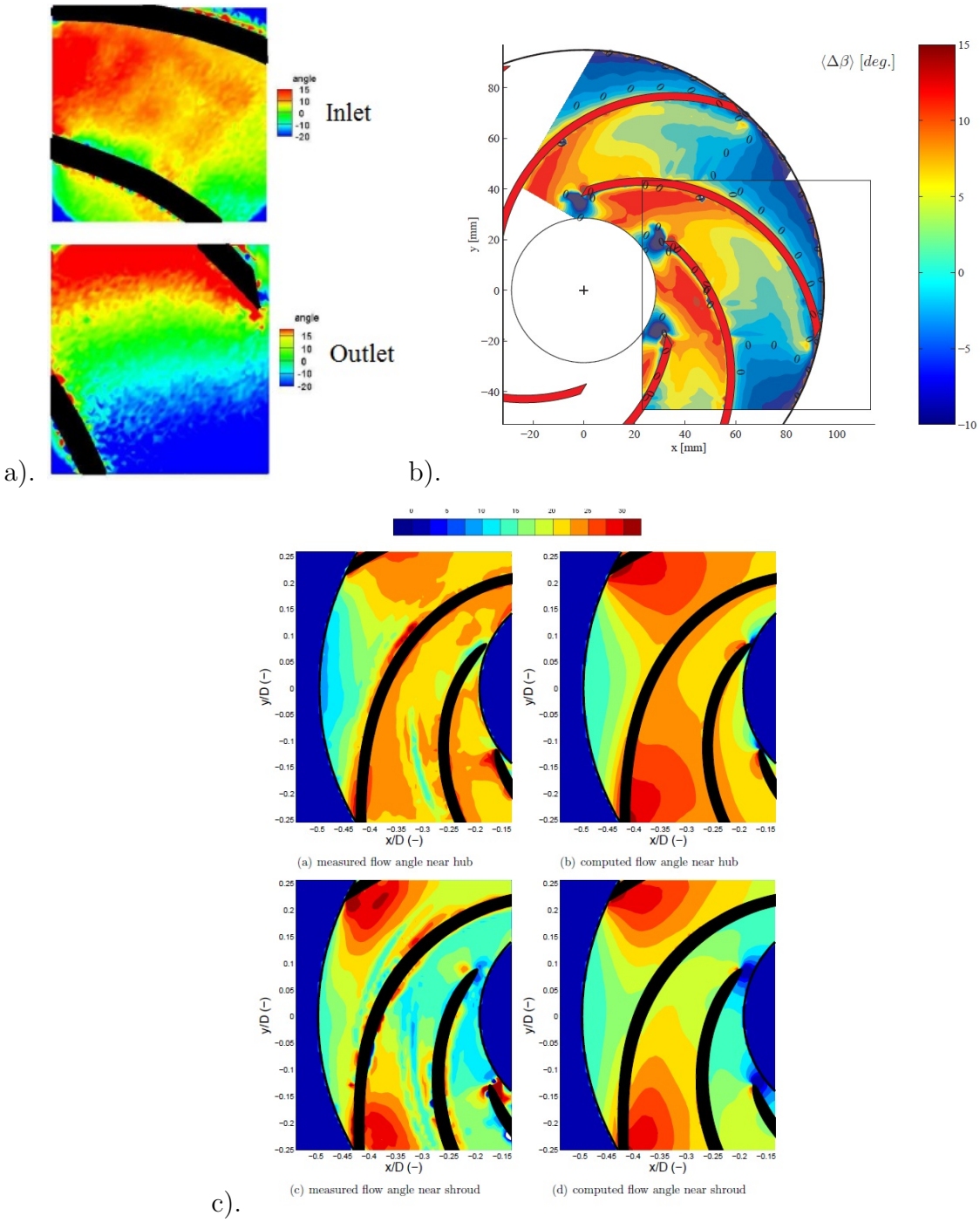

Figure 4.20: Fluid flow angle at the design flow rate for a) Altaf [3], b) Pedersen [33], c) Westra [44]

larger than the 'true channel' area of the 5 bladed impeller. It implies that the slip losses of fluid inside the 7 bladed impeller appears to be less than the fluid losses inside the 5 bladed impeller. This confirms the performance results shown in figure 4.6. The figure shows that the deviation between the theoretical head and the slip head prediction of the 7 bladed impeller is less than the deviation between the theoretical head and slip head prediction of the 5 bladed impeller at the design and 75% flow rates. Therefore, slip losses in the 5 bladed impeller are higher than slip losses in the 7 bladed impeller.

4.2.4 Flow behavior at high flow rates

Fluid flow streamlines at 140 % and 120 % flow rates

The fluid flow structures at high flow rates are represented by flow structures at 120% and 140% flow rates. The streamlines throughout the passage at high flow rates for the 5 and 7 bladed impellers are presented in figure 4.21. If at the design flow rate, no separation flow occurs on the blade pressure side of the 5 bladed impeller, the results show that there is a detached flow that occurs on the blade pressure side near the impeller inlet both of the 5 and 7 bladed impellers. This is probably caused by at high flow rate, the fluid velocity is high that makes the high 'angle of attack'. As discussed earlier the high 'angle of attack' can cause a separation flow on the blade pressure side. The streamline results also show that the flow close to the blade suction side follows the blade curvature.

Similar flow structures were found in studies by Westra [43] and Keller *et al.* [24] that are presented in figures 4.22b and 4.22d, respectively. Pictures of normalized relative velocity to tip blade speed (W/u_2) at high flow rate for this study are shown in figures 4.22a and b. In this study, the W/u_2 at high flow rate is represented by the contour plot at 140% flow rate whereas the W/u_2 in Westra [44] and Keller [24] are at 150% flow rate. As mentioned before, past studies have different impellers and experimental set up. However, the results of flow structure at high flow rate show similarity between this study and past studies. It can be seen that as the flow rate is increased, this study and past studies results confirm that the fluid velocity along the blade suction side increases. Moreover, the low velocity region which attaches to the blade pressure side becomes larger. Therefore, it can be concluded from the results of the streamlines and relative velocity that at high flow rates, the impeller geometry impeller and experimental set up becomes less of an influence on the flow structure.

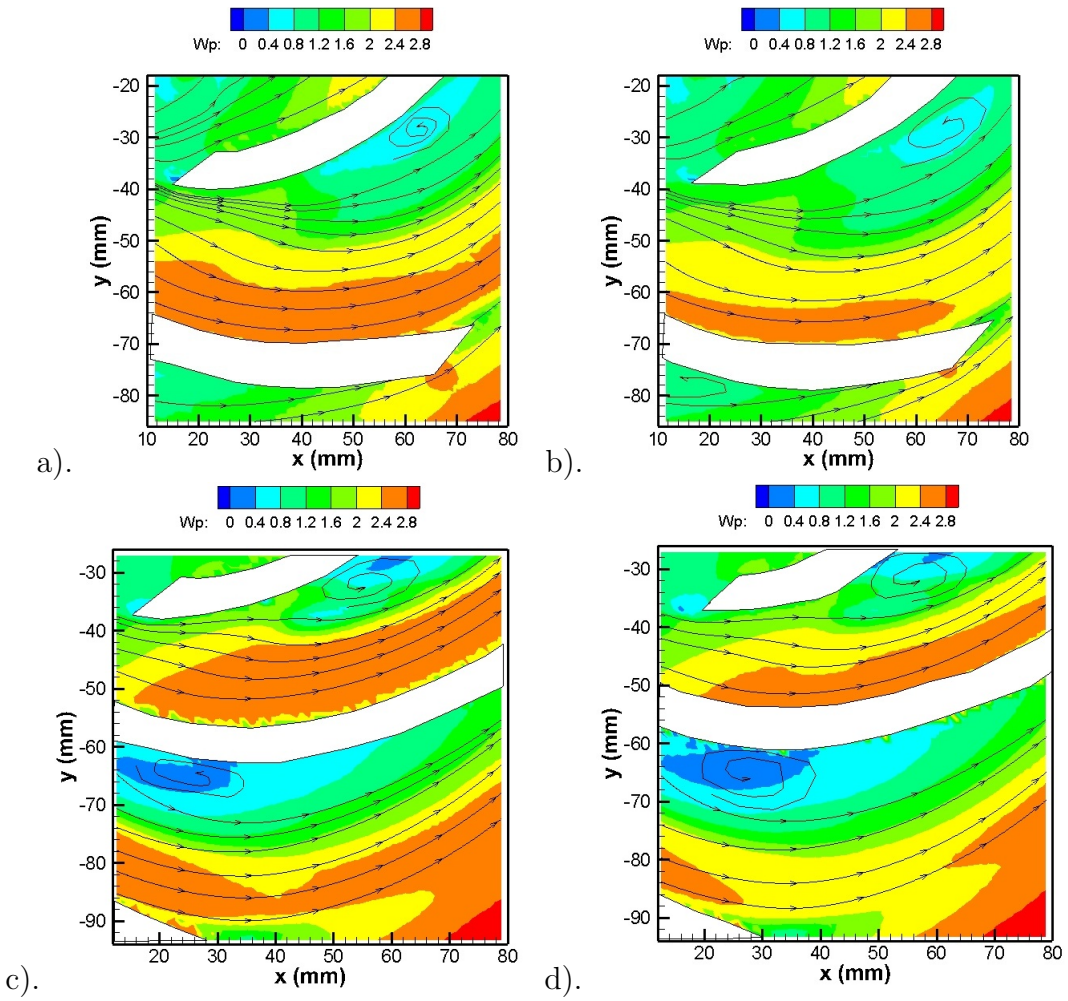

Figure 4.21: Fluid flow normalized streamlines at 300 rpm for a) 5 bladed impeller 140% flow rate t_d 0 ms, b) 5 bladed impeller 120% flow rate t_d 0 ms, c) 7 bladed impeller 140% flow rate t_d 0 ms, d) 7 bladed impeller 120% flow rate t_d 0 ms

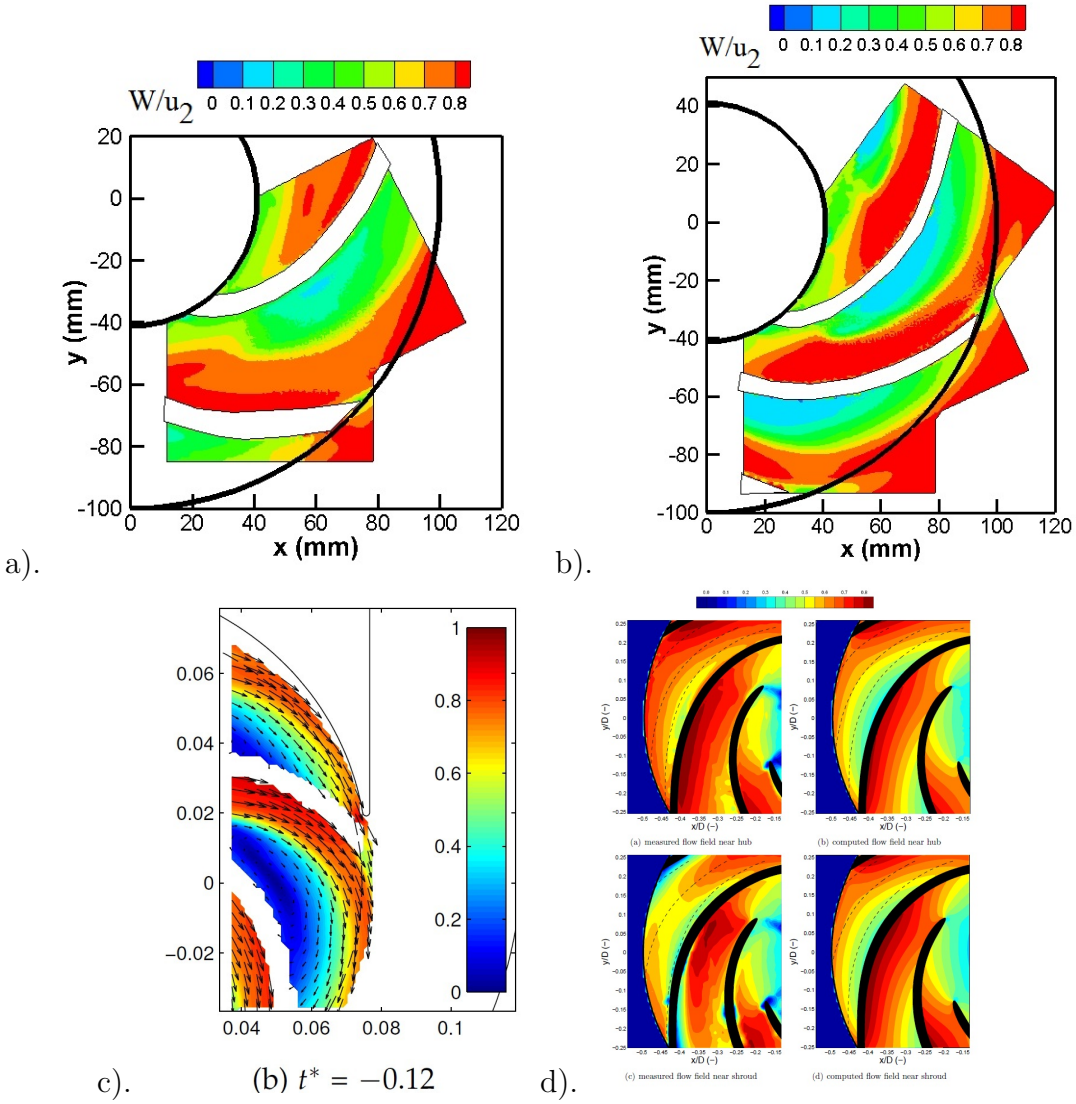

Figure 4.22: Normalized mean relative velocity contour to impeller tip speed at high flow rate for a) 140% 5 bladed impeller, b) 140% 7 bladed impeller, c) 150% Keller [24], d) 150% Westra [44],

Mean normalized primary and secondary velocity at 140% and 120% flow rates

Figure 4.23 shows plots of the mean normalized primary relative velocity to outlet rotational impeller velocity (W_p/u_2). At 140% flow rate, the magnitude of W_p increases from the blade pressure side to the blade suction side either along the impeller passage of the 5 and 7 bladed impellers. Hence, it can be inferred that the fluid flow along the passage at 140% rate agrees with the potential flow theory. It is also shown from the figures 4.23a and 4.23c, that a jet pattern does not occur. It is probably because at high flow rate, the fluid momentum is high because of high velocity and high mass flow rate. Hence, the boundary layer growth of fluid near the suction side is delayed [15] whereas as discussed in the design subsection, rapid growth fluid boundary layer near the blade suction side is one of the reasons jet pattern occurs at the exit of the blade pressure side. At the impeller inlet, The magnitude of W_p on the blade pressure side drops significantly which implies that a fluid detached occurs. Then, the magnitude W_p increases as fluid moves toward the impeller outlet. Similar to 140% flow rate, the magnitude of W_p at 120% flow rate also increases from the blade pressure side to the blade suction side. Hence, the fluid flow inside the impeller passage follows the potential flow theory. At the design flow rate, the jet pattern is evident at the exit of the blade pressure side but the jet pattern at high flow rates diminishes so it can be concluded that the jet pattern that occurs at the exit of the blade pressure side is more invisible when the flow is gradually increased.

The mean normalized secondary relative velocity profiles (W_s/u_2) at high flow rates are presented in figure 4.24. The magnitude of (W_s) is negative near the impeller inlet and it increases toward positive value as the fluid moves to the impeller exit. Hence, at the inlet, fluid tends to move to the blade suction side while close to the outlet, fluid tends to move to the blade pressure side. This is similar to the W_s pattern at the design flow rate. The secondary flow also has less influence on the fluid close to blade suction and pressure surface. However, in the middle of the passage, the secondary flow becomes stronger but the primary flow still has more influence on the flow structure since the magnitude of W_p is much higher than the magnitude of W_s.

Similar to the design flow rate, the magnitude of W_p and W_s at 120% and 140% flow rates increases as the fluid moves further from the impeller inlet so the energy is added from the impeller to the fluid. In addition, the magnitude of W at 120% is lower than the magnitude of W at 140% flow rate but it is higher than the magnitude of W at the design flow rate as expected. Hence, the head at 120% flow rate higher than at 140% flow rate but it is lower than the head at the design flow rate. Figure 4.14 shows that the fluid head rise at 140% flow rate is lower than the fluid head rise at the design flow rate. This result agrees with the performance results that are shown in figure 4.1.

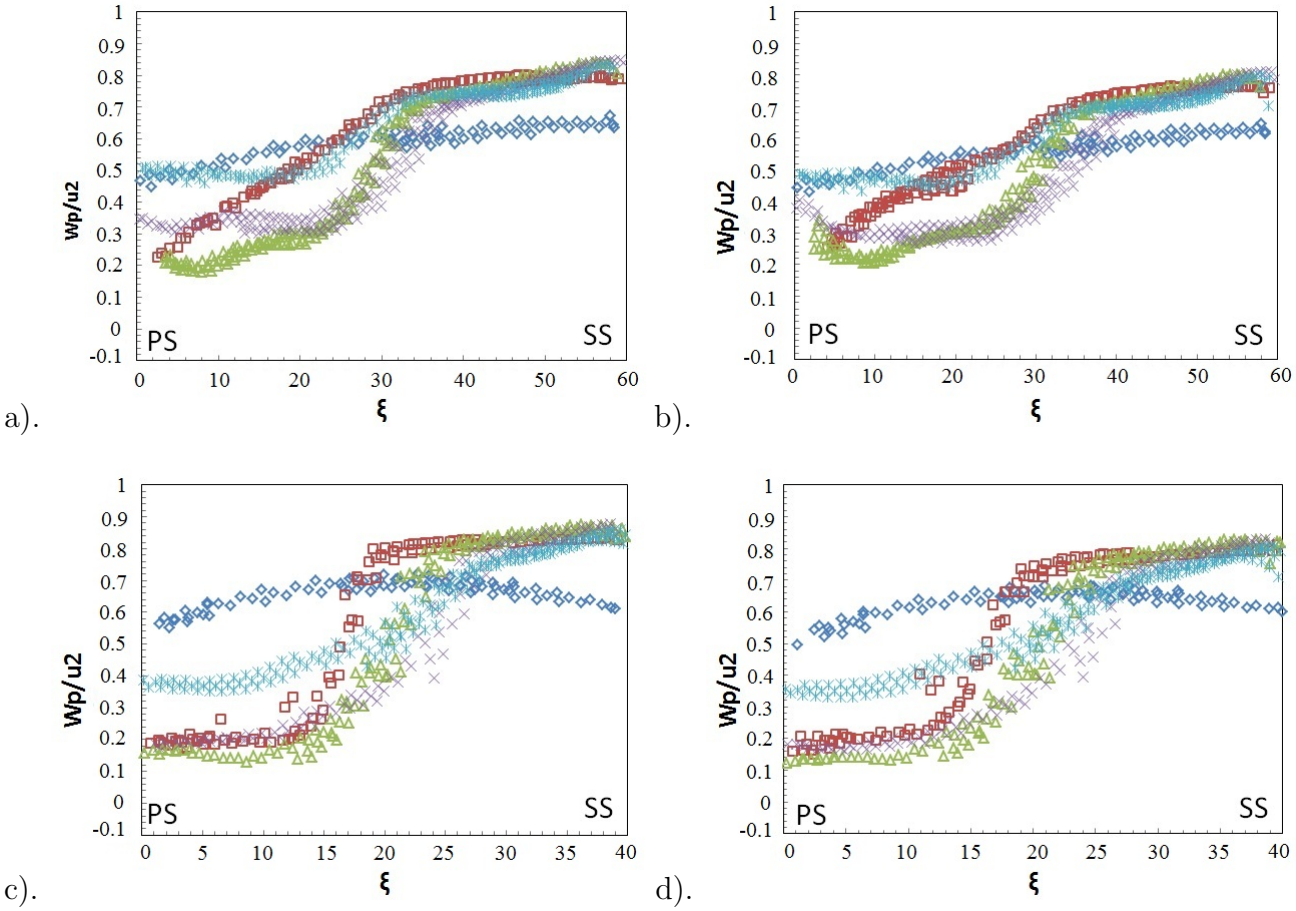

Figure 4.23: Mean normalized primary velocity at : $\diamond$ $R/R_2 = 0.5$; $\square$ $R/R_2 = 0.6$; $\triangle$ $R/R_2 = 0.7$; $\times$ $R/R_2 = 0.8$; $*$ $R/R_2 = 0.9$ for a) 5 bladed impeller 140% flow rate, b) 5 bladed impeller 120% flow rate, c) 7 bladed impeller 140% flow rate, d) 7 bladed impeller 120% flow rate

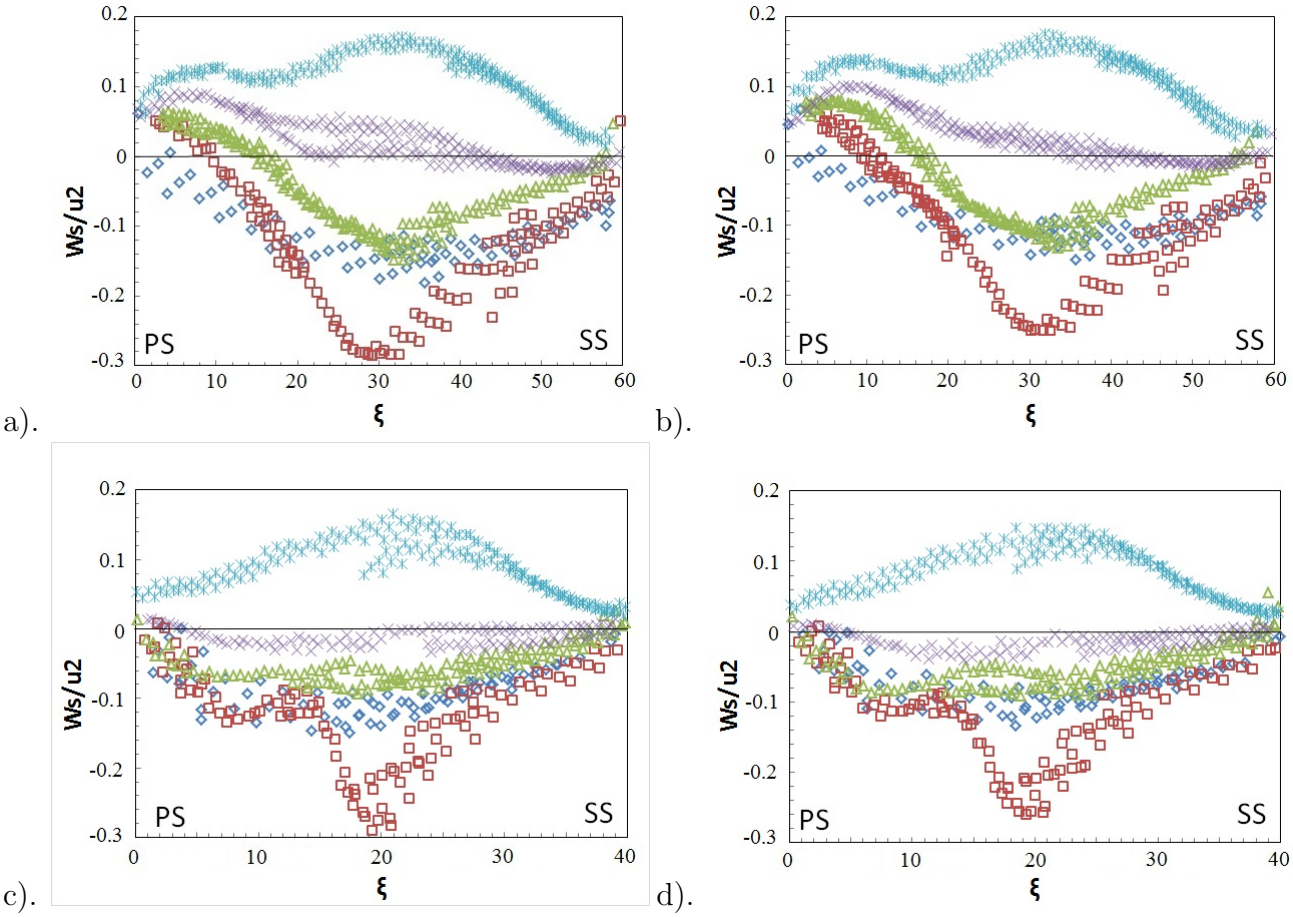

Figure 4.24: Mean normalized secondary velocity at $*$ $R/R_2 = 0.9$; $\times$ $R/R_2 = 0.8$; $\triangle$ $R/R_2 = 0.7$, $\square$ $R/R_2 = 0.6$, $\diamond$ $R/R_2 = 0.5$ for a) 5 bladed impeller 140% flow rate, b) 5 bladed impeller 120% flow rate, c) 7 bladed impeller 140% flow rate, d) 7 bladed impeller 120% flow rate

Comparison of W_p and W_s at 140 % and 120 % flow rates between 5 and 7 bladed impellers

The magnitude of W_p at the impeller inlet of the 7 bladed impeller is higher than the magnitude of W_p at the inlet of the 5 bladed impeller as shown in figure 4.25. The average magnitude of the W_p/u_2 at $R/R_2 = 0.5$ of the 5 bladed impeller is about 0.59 whereas the average magnitude of the W_p/u_2 at $R/R_2 = 0.5$ of the 7 bladed impeller is about 0.69. In addition, for the 7 bladed impeller, the magnitude of W_s/u_2 on the blade suction and pressure surface is about in zero line. In comparison, the magnitude of W_s/u_2 for the 5 bladed impeller on the blade pressure side surface is about 0.4. The reason that the 5 and 7 bladed W_p and W_s patterns are different at high flow rates is probably because of the geometry of the passage as previously discussed in the design flow rate section.

The results also show that the magnitude of W_p on the blade suction side along the passage of the 7 bladed impeller is about similar to the magnitude of W_p for the 5 bladed impeller. However, along the passage of the blade pressure side, the magnitude of W_p of the 7 bladed impeller is lower than for the 5 bladed impeller as shown in figure 4.25. This implies that the fluid inside the 7 bladed impeller receives higher energy transfer than the fluid inside the 5 bladed impeller as discussed in the design flow rate section. Therefore, similar to the design flow rate, the PIV results confirm the performance results that at flow high rates, the WHP for the 7 bladed impeller is higher than the 5 bladed impeller.

Turbulence intensity (TI) at 140 % and 120 % flow rates

The turbulence intensity (TI) contour at high flow rates for 5 and 7 bladed impellers are presented in figure 4.26. Similar pattern of TI at high flow rates was also obtained in the experiments conducted by Keller *et al.* [24] that is presented in figure 4.27. Keller *et al.* [24] used term of k^*_{2D} which is the normalized plane phase-averaged TKE with the blade tip velocity ($k^*_{2D} = (\overline{u'u'} + \overline{v'v'})/2u_2^2$) to show the fluid fluctuation inside the impeller. Recent and past studies results shows that the relatively high TI attaches the blade pressure side as a result of the separation flow.

Even though the region of low TI contour on the blade suction becomes larger compared to the design flow rate, the TI generally increases when the flow rate is increased. The average magnitude of TI of fluid inside a passage of the 5 bladed impeller at 140% flow rate is about 0.122 whereas as has been mentioned before, at the design flow rate the average magnitude of TI are 0.108. Hence, the fluid at high flow rates appears to experience higher losses which also agrees with the theory implied in figure 1.8 that higher flow rate will create higher turbulence losses.

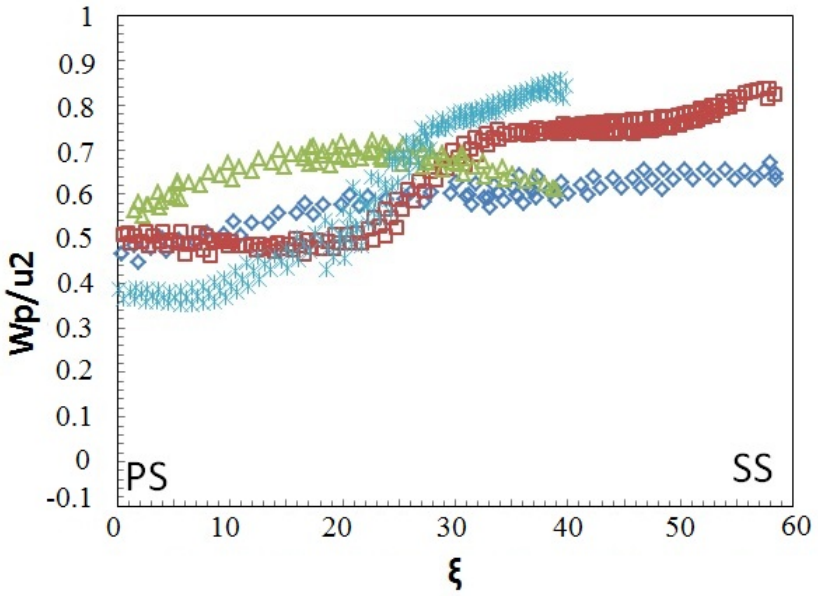

Figure 4.25: Comparison of Mean normalized primary velocity at 140% flow rate of the 5 bladed impeller at $\diamond$ R/R_2 0.5 and $\square$ R/R_2 0.9 and the 7 bladed impeller at $\triangle$ R/R_2 0.5 and $*$ R/R_2 0.9

In addition, it is also shown that the 7 bladed impeller has higher magnitude of TI than the 5 bladed impeller. The average TI of fluid inside a passage of the 7 bladed impeller at 140% flow rate is about 0.152. Similar to the design flow rate, it implies that fluid inside the 7 bladed impeller experiences higher losses.

Fluid angle deviation (β_d) at 140 % and 120 % flow rates

Fluid angle deviation (β_d) contours at high flow rates are presented in figure 4.28. Similar to the design flow rate, the high positive value of β_d is shown at the impeller inlet. However, at high flow rates, the area of the positive β_d is larger and it lies starting from the blade suction side to blade pressure side at the impeller inlet. This is probably because higher flow rates have higher bulk flow influence on the inlet flow.

The results also show that when the flow is gradually increased from the design flow rate to 140% flow rate, the inner region of zero contour line increases. The area of the 'true channel' of the 5 bladed impeller at 140% flow rate is about 52% of the passage whereas

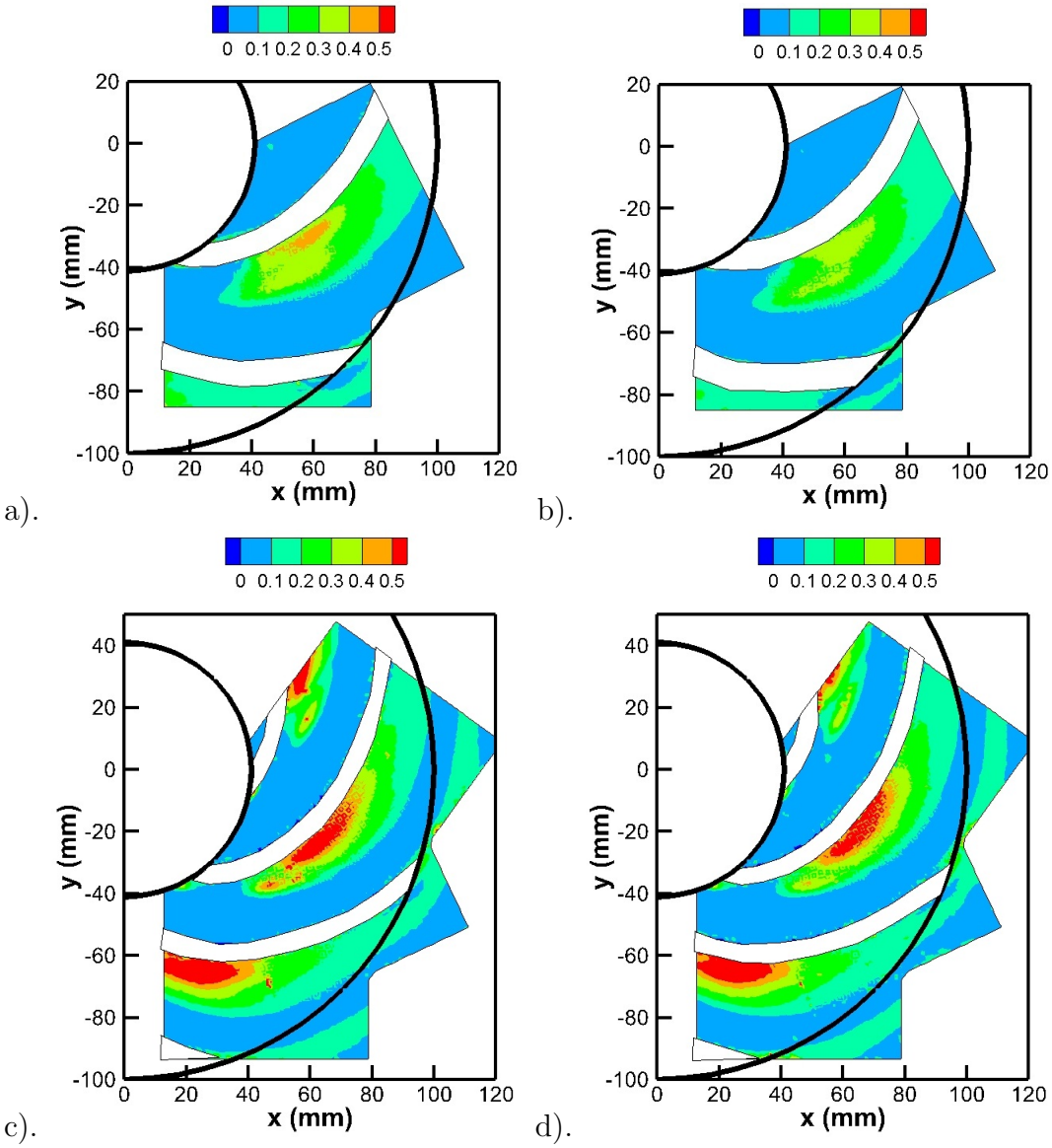

Figure 4.26: Fluid flow turbulence intensity inside the impeller passage for a) 5 bladed impeller 140% flow rate, b) 5 bladed impeller 120% flow rate, c) 7 bladed impeller 140% flow rate, d) 7 bladed impeller 120% flow rate

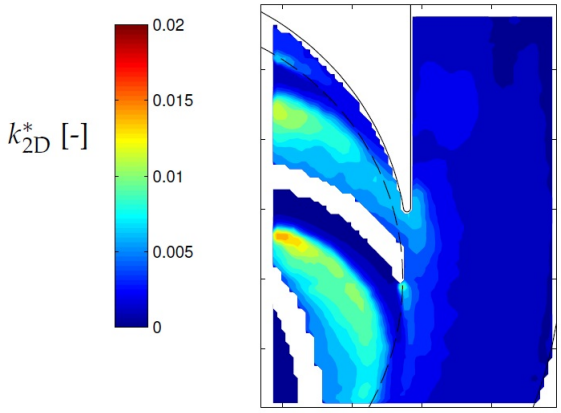

(a) $t^* = -0.25$

Figure 4.27: Normalized turbulence intensity to rotational impeller $k_2^* D$ at 150% flow rate conducted by Keller [23]

at the design flow rate the inner region is about 25% of the passage. In addition, similar to the design flow rate, the 'true channel' area of the 7 bladed impeller is larger than the 'true channel' area of the 5 bladed impeller at high flow rates. The 'true channel' of the 7 bladed impeller at 140% flow rate is about 68% of the passage. Hence, as discussed in the design flow rate section, this means that when the flow rate and the number of blades are gradually increased, the fluid experiences less slip losses which is validated from theory and performance results shown in figures 1.8 and 4.6. The high 'angle of attack' which might cause separation flow at high flow rates on the blade pressure side as shown in streamlines section appears at the inlet of both 5 and 7 bladed impellers (marked in the little box of figure 4.28).

4.2.5 Flow behavior at low flow rates

Fluid flow streamlines at 50 % and 25 % flow rates

The streamlines throughout the passage at low flow rates for the 5 and 7 bladed impellers are presented in figure 4.29. The results show that at 50% flow rate, there is a detached flow that occurs at the middle of the blade pressure side. At the trailing edge of the blade suction side, there is a small wake region. However, near the trailing edge of the blade

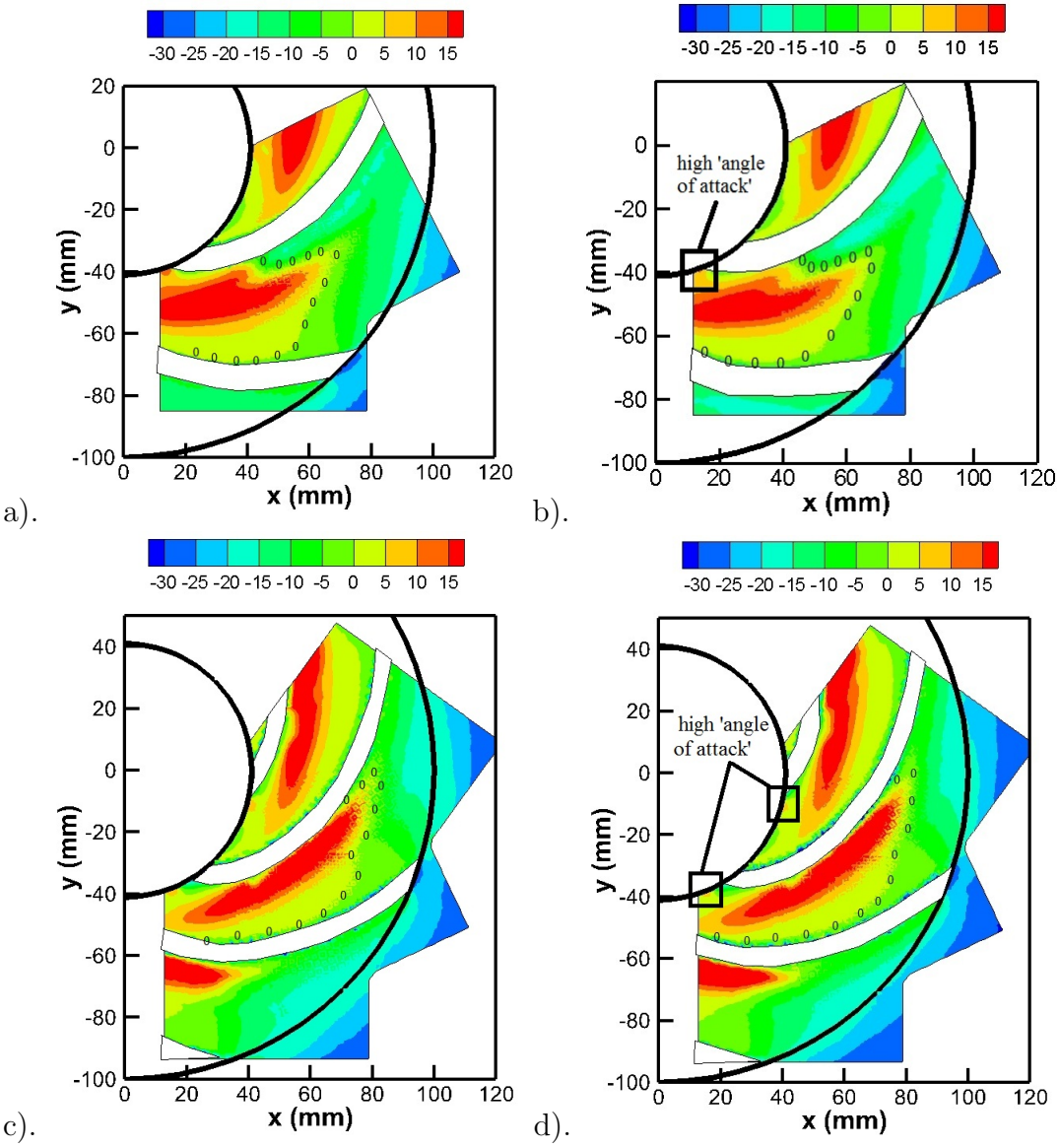

Figure 4.28: Fluid angle deviation in the impeller passage for a) 5 bladed impeller 140% flow rate, b) 5 bladed impeller 120% flow rate, c) 7 bladed impeller 140% flow rate, d) 7 bladed impeller 120% flow rate

pressure side, the fluid follows the blade curvature which is might an evidence of a jet pattern. Therefore, a jet-wake pattern evident appears at 50% flow rate.

At 25% flow rate, the wake region becomes stronger. The wake region on the trailing edge of the blade suction surface becomes larger. The wake region on the blade pressure surface moves from the middle blade surface toward the impeller outlet. It has been discussed that when the flow rate is decreased, the fluid momentum also decreases so the flow might experience more severe viscous effects.

The PIV result in this study is similar to the flow structure of a 7 bladed impeller in an experiment conducted by Murakami *et al.* [32]. The flow structure of the 7 bladed impeller at 33% flow rate was captured using surface oil flow visualization method shown in figure 4.30. The figure shows that at 33% flow rate, there are two wake regions that are captured on the hub of the 7 bladed impeller. The wake region on the blade suction side was appeared starting from the region that was covered by the blade pressure side (marked on the yellow line in figure 4.30). The separation line between the wake and flow regions was clearly visible straight from the inlet of the impeller to the trailing edge of the blade suction side (marked as the blue line in figure 4.30). The other wake region was attached on the blade pressure side close to the impeller exit and it looks smaller than the wake region on the blade suction side. These flow patterns are really similar to the flow structure that is obtained using PIV measurements in this study as shown in figure 4.29d.

Unlike the past study conducted by Pedersen *et al.* [34], in this study, the two-channel phenomena at low flow rates does not appear. Pedersen *et al.* [34] mentioned that two-channel phenomena occurred at low flow rates as a result of the even number of the blades. This study used 5 and 7 bladed impellers so it might be the reason that there is no 'stall-unstall' channel appeared in this study. The two-channel phenomena is shown in figure 2.9b. The past study conducted by Altaf [3] showed that at the quarter flow rate, fluid stall that blocked the impeller passage appeared. The stall was not stable but it was moving from inlet toward the impeller outlet.

Figure 4.31 shows plots of the dimensionless of mean relative velocity to outlet rotational impeller velocity at low flow rates (W/u_2) of several studies [23][43]. All of the studies show that at the low flow rate, the relative velocity at the inlet is still high but generally, the relative velocity decreases compared to the design flow rate. However, it can be seen that the low relative velocity region of each impeller is located in different area. Keller [23] found that at 40% flow rate, the low relative velocity region was at the middle of the passage which is shown in figure 4.31c whereas in Westra [43] shown in figure 4.31d, it was on the blade suction and pressure surface. In comparison, for the 5 bladed impeller in this study, the low relative velocity region is on the blade pressure surface and small region at

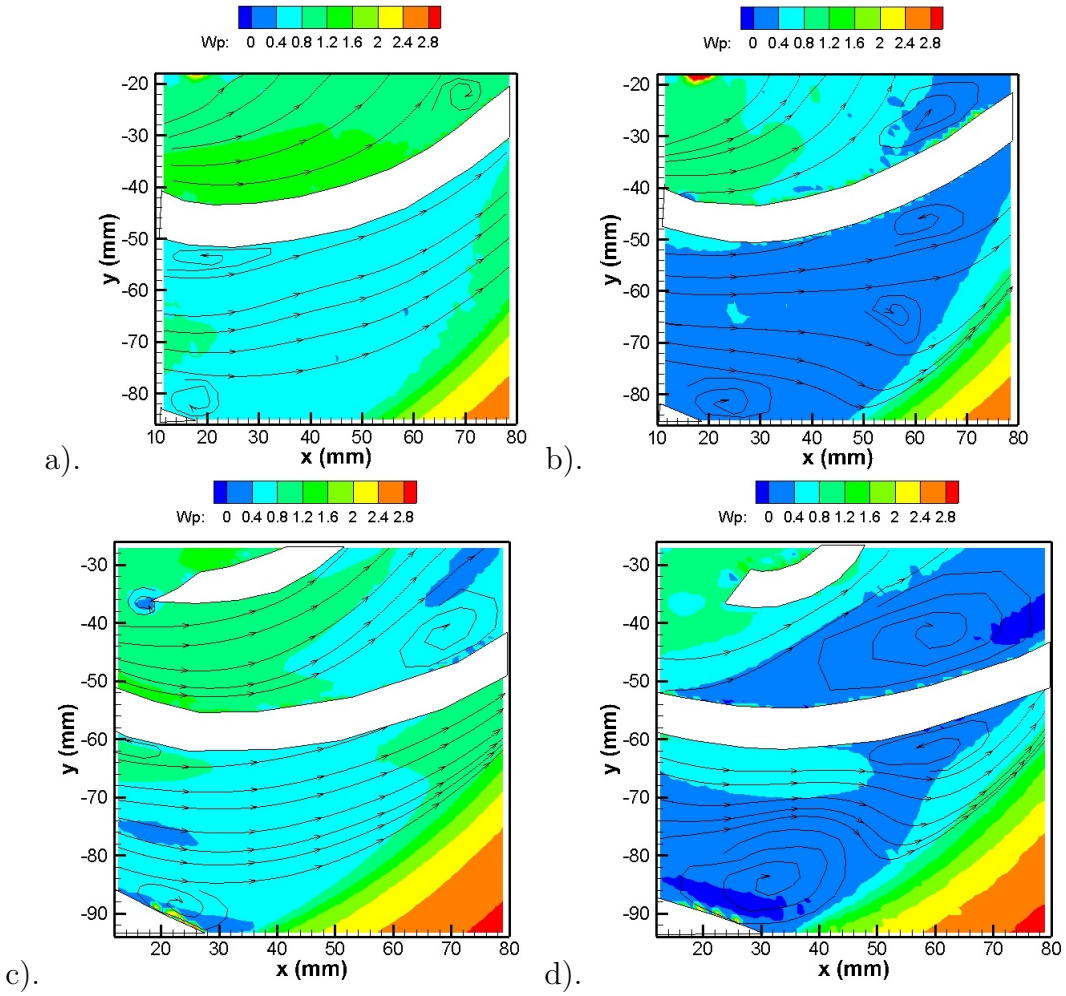

Figure 4.29: Fluid flow normalized streamlines at 300 rpm for a) 5 bladed impeller 50% flow rate at t_d of 15 ms, b) 5 bladed impeller 25% flow rate at t_d of 15 ms, c) 7 bladed impeller 50% flow rate at t_d of 0 ms, d) 7 bladed impeller 25% flow rate at t_d of 0 ms

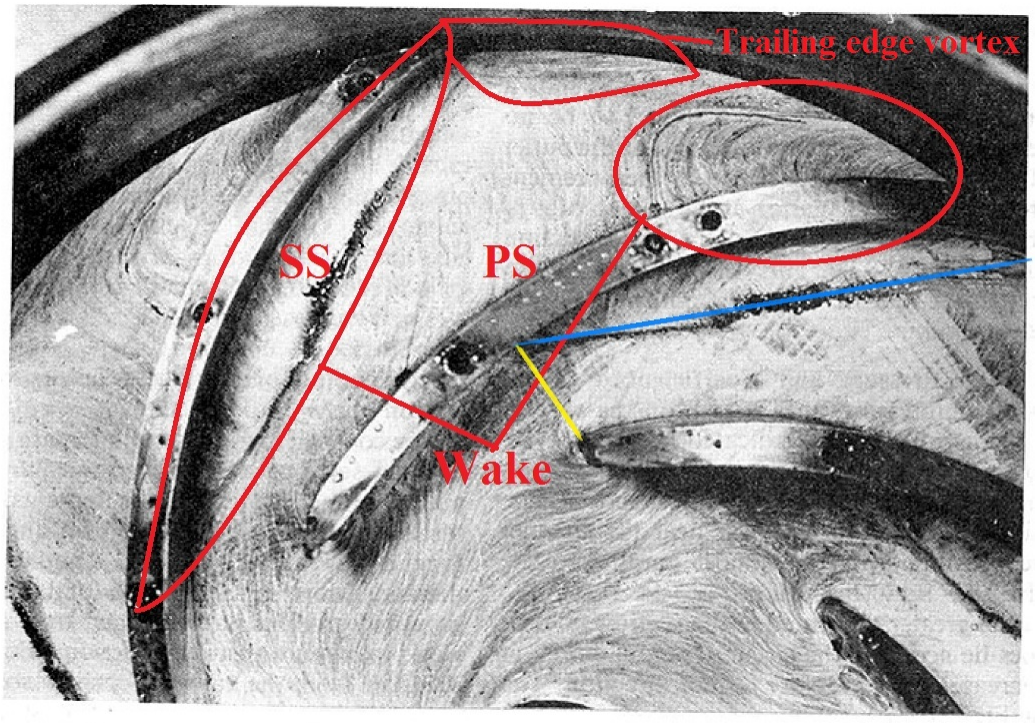

Figure 4.30: Oil flow surface of a 7 bladed impeller at 33% flow rate conducted by Murakami *et al.* [32]

the middle passage and for the 7 bladed impeller, the low velocity region is on the blade suction surface. Therefore, from the relative velocity perspective, the number of blades has a greater influence on the fluid structure compared to the design and high flow rates.

Some differences are found between flow structure inside the passage of the 5 and 7 bladed impellers. The results show that at 50% flow rate, the wake region on the blade suction and pressure surface for the 5 bladed impeller is smaller than the wake region inside the 7 bladed impeller. This is probably because the 7 bladed impeller has more restrictions compared to the 5 bladed impeller so the fluid experiences the a more severe viscous effect. At 25% flow rate, there are 2 main wake regions inside the 7 bladed impeller which are on the trailing edge of the blade suction surface and on the blade pressure surface. However, for the 5 bladed impellers, there are 3 main wake regions which are on the trailing edge of the blade suction impeller, on the blade pressure side and in the middle area of the impeller outlet. The wake region in the middle of the passage at the impeller outlet might be created because the fluid in the middle region is compressed by both of the fluids which detach

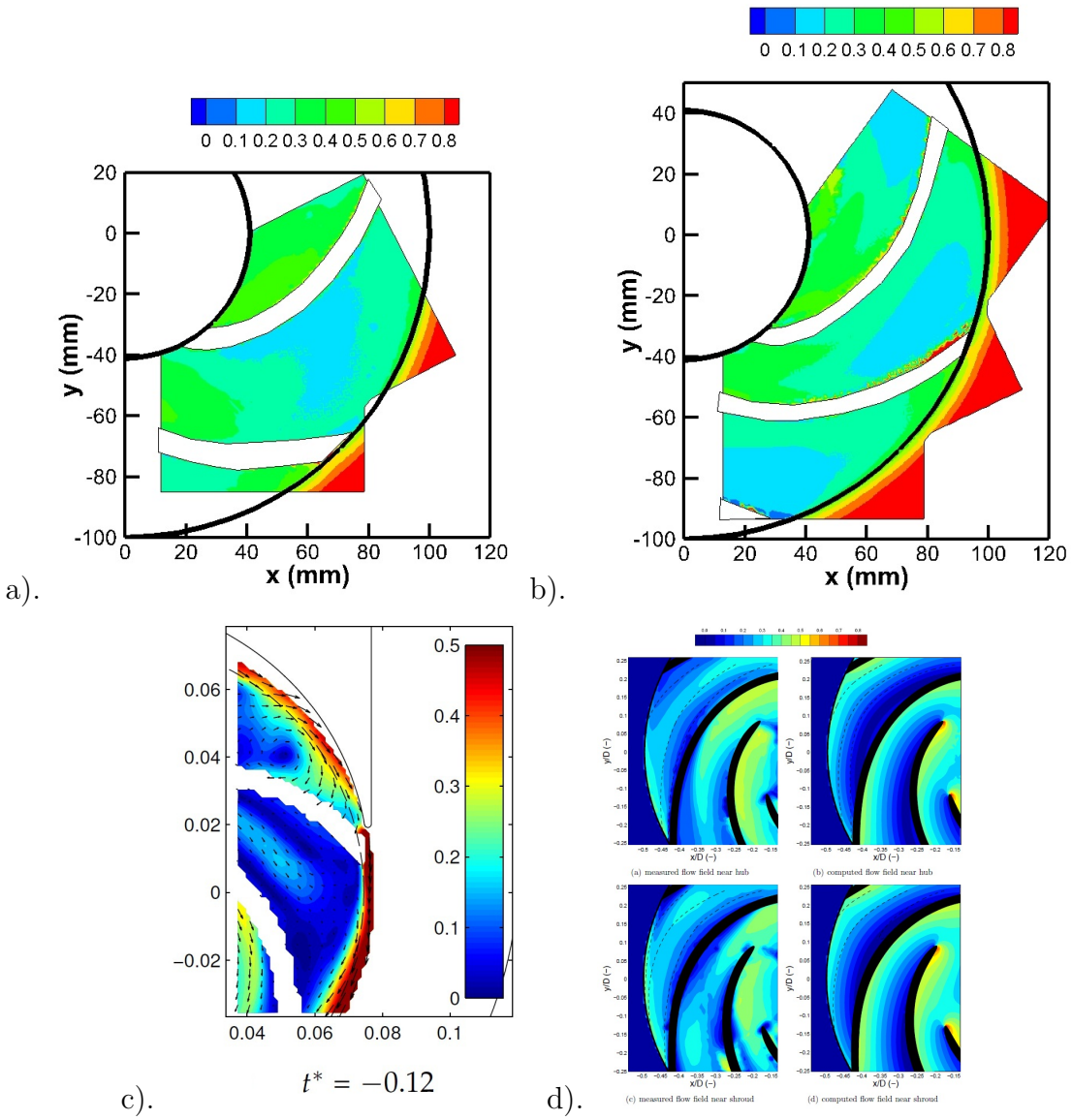

Figure 4.31: Normalized mean relative velocity contour to impeller tip speed at high flow rate for a) 50% 5 bladed impeller, b) 50% 7 bladed impeller, c) 40% Keller [24], d) 40% Westra [44]

from the blade suction and pressure surfaces. In addition, since the 5 bladed impeller has wider passage outlet area, both of detached flows closes the area in the middle of the passage. In summary, at low flow rates, the influence of the number of blades becomes stronger.

To validate the mean streamline results that are suspected to show any differences to the actual fluid motion at low flow rate, an investigation is performed to observe the instantaneous fluid streamlines map. The instantaneous streamlines maps show that small vortices are found in several locations of the blade suction and pressure sides. The appearance of the small vortices is probably because 3D effects influence the particle movement or the time between pulses of the laser is too short. The vortex has a very high velocity at the center but the velocity is very low in the outer radius vortex [15]. However, if the time between pulses was set longer, the error might also increase as discussed in the PIV error section. This problem probably can be solved by obtaining the relative velocity directly without involving a vector calculation. It will be discussed later in the recommendations. However, the location of the vortices from instantaneous streamline results is similar to the 1000 mean streamline results. In addition, the mean streamlines are similar to the visualization flow structure obtained in past experiments [32]. Therefore, it can be concluded that the mean streamlines map can be represented as flow structure at low flow rates since it is only has small differences to the instantaneous streamline map.

Mean normalized primary and secondary velocity at 50% and 25% flow rates

Figure 4.33 shows plots of the mean primary relative velocity to outlet rotational impeller velocity (W_p/u_2) at 50% and 25% flow rates. At 50% flow rate, the magnitude of W_p increases from the blade pressure side to suction side either for the 5 and 7 bladed impellers only at the inlet. However, starting at R = 70 mm, the pattern changes; the magnitude of W_p increases from the blade suction side to the blade pressure side. It is different to the design flow rate. Hence, the flow which agrees with the potential flow theory only occurs at the inlet. Detail observations of fluid close to the blade suction side reveal that the magnitude of W_p decreases along the blade. This shows that the viscous effect is probably influencing the fluid on the blade suction surface. This is probably because the fluid mass and the fluid velocity entering the impeller has decreased, so the fluid momentum decreases.

It has been discussed that 75% and 50% flow rates have a jet pattern, but at 75% flow rate no wake is found at the exit on the blade suction side. At 50 flow rate, the results show that the magnitude of W_p on the blade suction side is high at the inlet but very low at the outlet. This phenomena does not occur at 75% flow rate. This is a sign that there

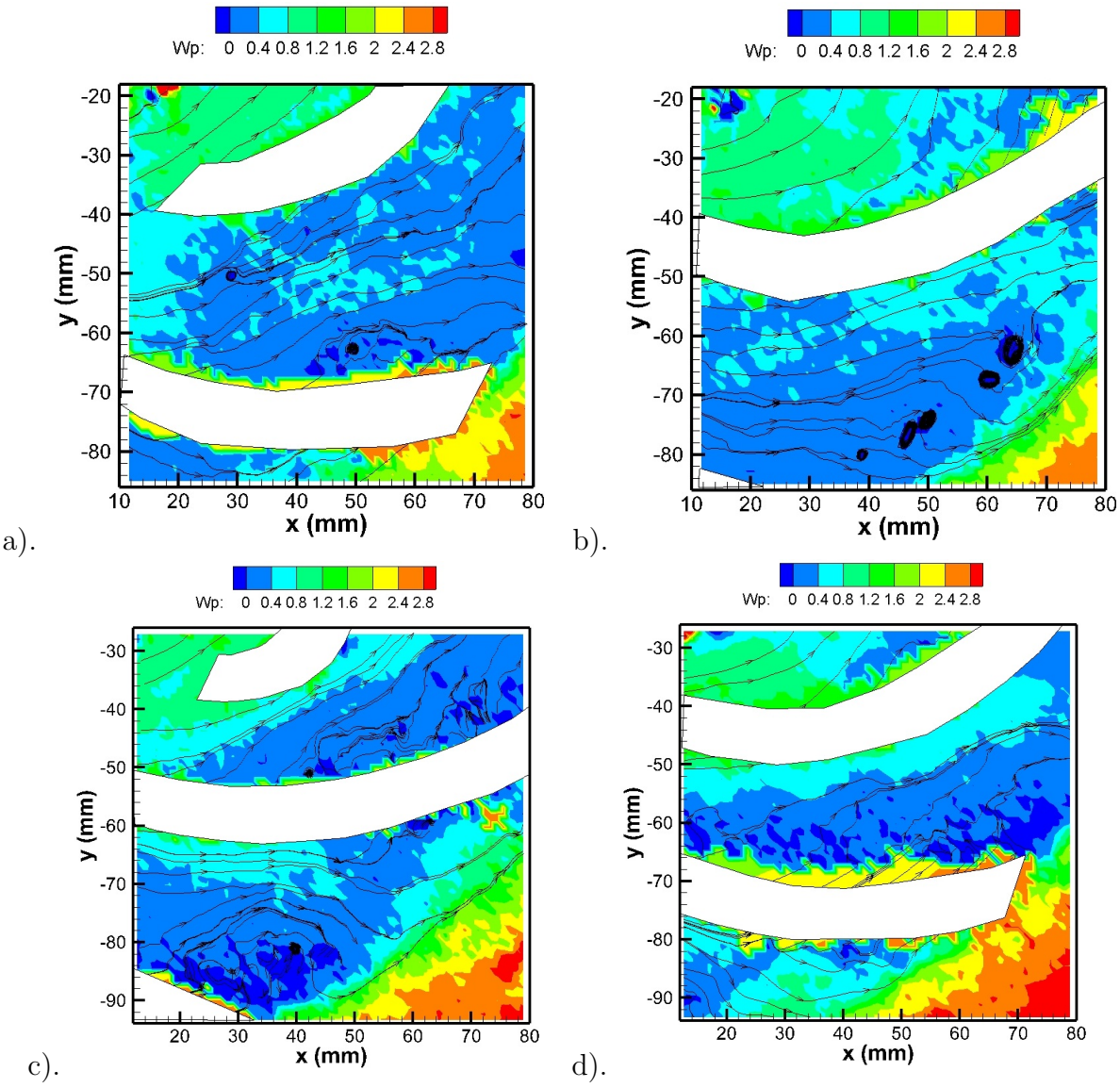

Figure 4.32: Fluid flow instantaneous streamlines at 25% flow rate for a) 5 bladed impeller at t_d of 0 ms, b) 5 bladed impeller at t_d of 15 ms, c) 7 bladed impeller at t_d of 0 ms, d) 7 bladed impeller at t_d of 14 ms

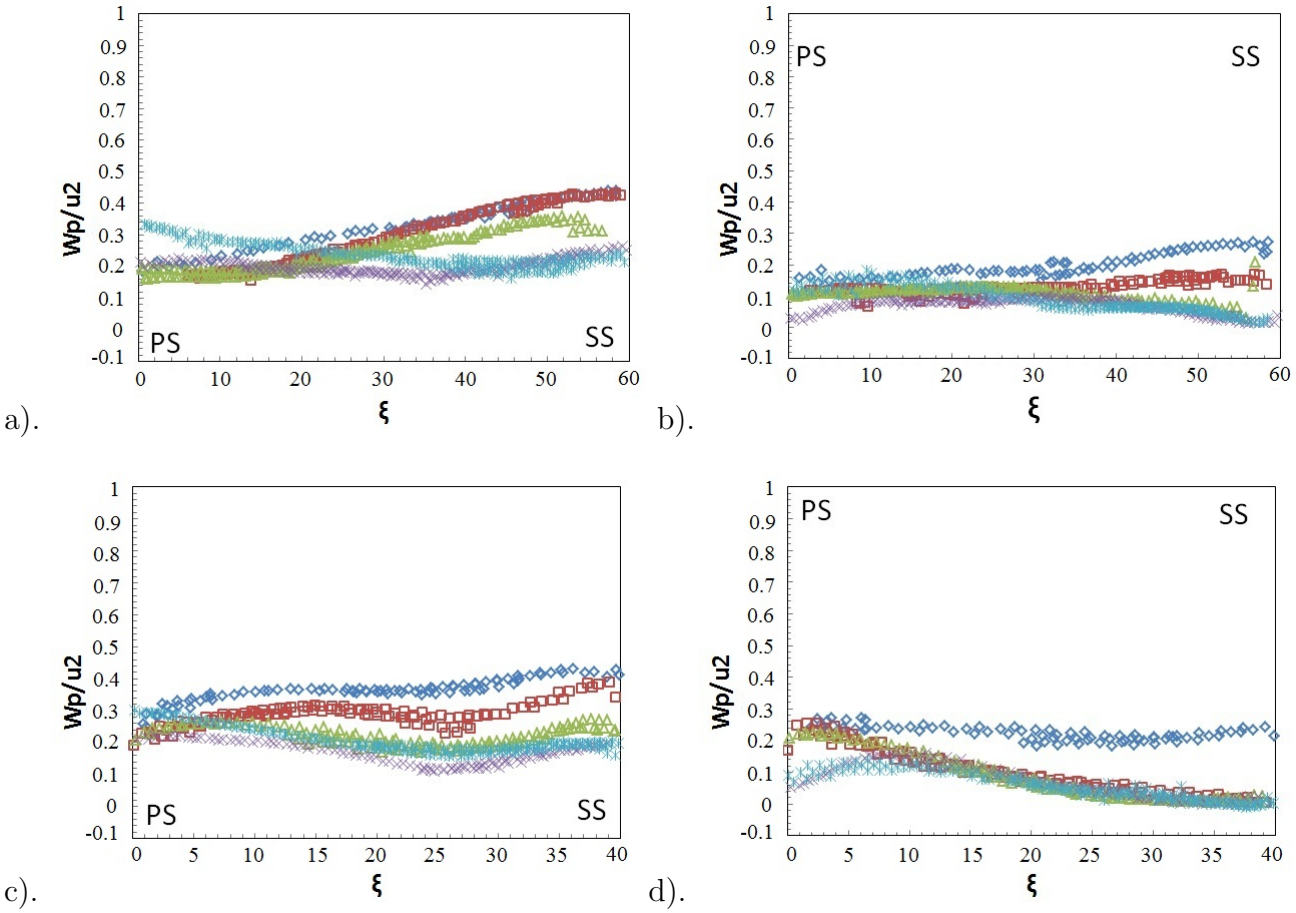

Figure 4.33: Mean normalized primary velocity at $*$ $R/R_2 = 0.9$; $\times$ $R/R_2 = 0.8$; $\triangle$ $R/R_2 = 0.7$, $\square$ $R/R_2 = 0.6$, $\diamond$ $R/R_2 = 0.5$ for a) 5 bladed impeller 50% flow rate, b) 7 bladed impeller 25% flow rate, c) 7 bladed impeller 50% flow rate, d) 7 bladed impeller 25% flow rate

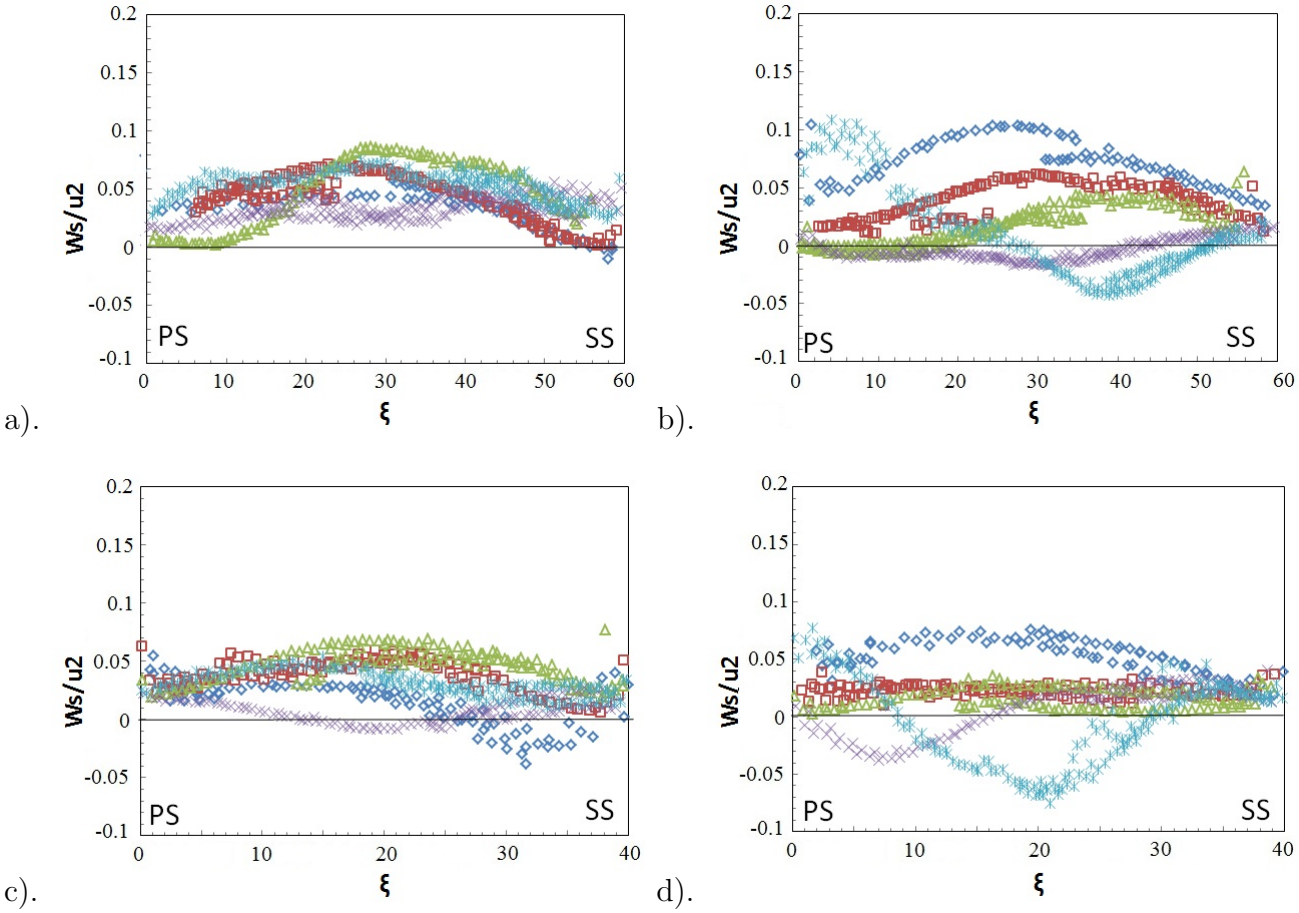

Figure 4.34: Mean normalized secondary velocity at $* \; R/R_2 = 0.9$; $\times \; R/R_2 = 0.8$; $\triangle \; R/R_2 = 0.7$, $\square \; R/R_2 = 0.6$, $\diamond \; R/R_2 = 0.5$ for a) 5 bladed impeller 50% flow rate, b) 5 bladed impeller 25% flow rate, c) 5 bladed impeller 50% flow rate, d) 7 bladed impeller 25% flow rate

might be a wake zone which contains vortices on the blade suction side near the impeller exit. Therefore, at 50% flow rate the phenomena of a jet-wake pattern might occur in this study. A similar W_p pattern at low flow rate was found in an experiment conducted by Murakami *et al.* [32] as shown in figure 4.35. It shows that as the fluid moves toward the impeller exit, W_p increases on the blade pressure side.

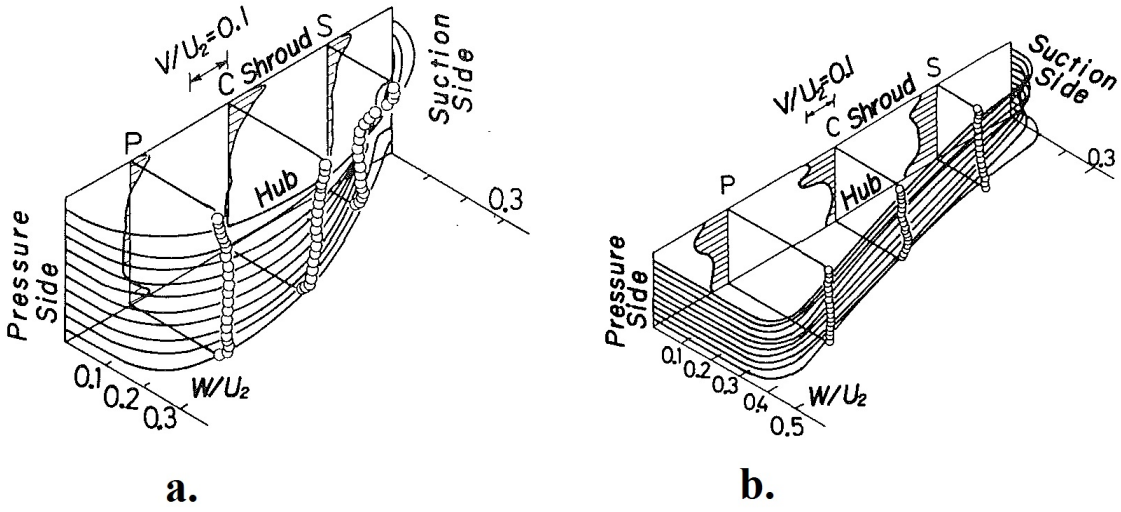

Figure 4.35: Primary and secondary velocity profile of a 7 bladed impeller at 65% flow rate at the impeller inlet (a) and outlet (b) conducted by Murakami *et al.* [32]

Unlike other flow rate conditions, the flow structure along the passage of the 5 and 7 bladed impellers at 25% flow rate shows that the fluid does not follow the potential flow theory. The magnitude of the W_p at 25% flow rate, especially for the 7 bladed impeller, increases from the blade suction side to the blade pressure side. At 25% flow rate, the decreasing of magnitude of W_p for fluid along the blade suction side becomes more obvious compared to 50% flow rate. This indicates that the wake region attaching the blade suction side becomes stronger when the flow rate is decreased. If the magnitude of the W_p for fluid along the blade pressure side at 50% rate increases from inlet to outlet but at 25% flow rate, the magnitude of W_p for the fluid along the blade pressure side decreases. This indicates that near the exit, there is probably a wake region similar on the blade suction side. However, because the drop of W_p on the blade pressure side is not significant compared to on the blade suction side, the wake region on the blade suction side is more obvious. It also can be inferred that the jet-wake pattern diminishes at 25% flow rate.

The mean normalized secondary relative velocity with rotational impeller velocity (W_s/u_2) at low flow rates are presented in figure 4.34. As seen in figures 4.34a and 4.34c, the magnitude of (W_s) for 50% flow rates is positive along the impeller passage. Hence, at the inlet, fluid tends to move to the blade pressure side. This indicates that the fluid does not follow the potential flow theory near the impeller exit which is also confirmed in the (W_p) results. A similar W_s pattern is obtained in past studies which is shown in figure 4.35 [32].

The profile of secondary flow at 25% flow rate for the 5 and 7 bladed impellers are presented in figures 4.34b and 4.34d. Similar to 50% flow rate, the magnitude of W_s at the impeller inlet of 25% flow rate is positive but it is higher compared to 50% flow rate. the tendency of the fluid to move to the blade pressure side is greater. Unlike the 50% flow rate, near the impeller outlet, the magnitude of W_s is negative which indicates that the fluid tends to move to the blade suction side. This pattern is the opposite of the pattern that is implied in potential flow shown in figure 1.12a. The very low fluid momentum might cause this pattern to happen.

Comparison of W_p and W_s at 50 % and 25 % flow rates between the 5 and 7 bladed impellers

The comparisons of flow structure between the 5 and 7 bladed impellers are shown from the results of mean normalized primary and secondary flow component at low flow rates. At low flow rates, the magnitude of W_p of the 5 bladed impeller is lower than the 7 bladed impeller. For instance, the average of W_p/u_2 at $R/R_2 = 0.9$ and 0.5 at 50% flow rate of the 5 bladed impeller are 0.318 and 0.327, respectively whereas the average of W_p/u_2 at $R/R_2 = 0.9$ and 0.5 of the 7 bladed impeller are 0.343 and 0.345, respectively. The secondary flow component also shows similarity with the primary velocity component the magnitude of W_s of the 5 bladed impeller is lower than the 7 bladed impeller. At 25% flow rate, the magnitude of W_s/u_2 of fluid the 5 bladed impeller at $R/R_2 = 0.5$ and 0.9 are 0.099 and 0.094, respectively. In comparison, the magnitude of W_s/u_2 of fluid the 7 bladed impeller at $R/R_2 = 0.5$ and 0.9 are 0.119 and 0.117, respectively. In addition, the magnitude of W_p/u_2 at $R/R_2 = 0.9$ close to the blade pressure of the 5 bladed impeller at 50% flow rate is 0.35 whereas The magnitude of W_p/u_2 at $R/R_2 = 0.9$ close to the blade pressure of the 7 bladed impeller is 0.29 which means that the jet pattern is stronger for the 5 bladed impeller. The lower W_p and W_s and the stronger jet pattern are probably caused by the passage geometry which has been discussed in the design flow rate subsection. As mentioned previously, past research conducted by Houlin *et al.* [19] also noticed that the jet pattern became stronger for an impeller that has a lower number of blades.

Turbulence intensity (TI) at 50 % and 25 % flow rates

Turbulence Intensity (TI) contour at low flow rates for the 5 and 7 bladed impellers are presented in figure 4.36. The results show that as the flow rate is decreased, the TI gradually increases. The average and maximum TI at 25% flow rate of fluid in a passage of the 5 bladed impeller is 0.374 and 3.804. it is obviously much higher compared to the design and high flow rates. This is because the mean velocities are low or the fluid fluctuates more. The results also show that if at the design and high flow rates on the blade suction side is attached the low TI contour, at low flow rates, on the blade suction side is attached the relatively high TI contour. The results also show that at 25% flow rate, there is a small region of high TI that attaches the blade pressure side near the impeller exit. The high intensity contour near the blade suction and pressure surfaces indicate the recirculation flow zone that has been mentioned in the streamlines subsection.

The results also show that at low flow rates, the fluid structure is identical between passages. It indicates that the two-channel phenomena does not occur in this study. If the two-channel appears in the experiment, the fluctuation will be similar to the figure 4.37 that one passage has a high fluctuation region on the inlet of the blade pressure region and the passage in front of it has a relatively low fluid fluctuation. It should be noted that Pedersen [33] used k_{2D} for showing the fluid fluctuation which is similar to TKE in this study (see equation 3.17). In Pedersen [33] results, the high TKE lay at the exit from the blade suction side to the blade pressure side. Pedersen [33] reported that the high TKE at the exit due to interaction of fluid exit the passage with diffusers. In this study, high TI also appears at the exit across the blade suction and pressure side. However, this might be caused by the interaction of fluid close the outlet with the fluid that exits from the blade pressure side of the passage in front of it. The fluid interaction at the impeller exit will be discussed in more detail in fluid angle deviation section.

The comparisons between the 5 and 7 bladed impellers are shown in the TI contour results. The relatively high TI contour lies close to the blade suction side of the 7 bladed impeller at 50% flow rate. However, the relatively high TI contour for the 5 bladed impeller at 50% flow rate is located near the impeller exit from the blade suction side to the blade pressure side. The average TI at 25% flow rate of fluid in a passage of the 7 bladed impeller is 0.83 which is much higher than 5 bladed impeller. This indicates that 7 bladed impeller has higher turbulence losses. It can be seen from figure B.2 in Appendix B that the efficiency of the 7 bladed impeller is very low at 25% flow rate although the 7 bladed impeller produces a higher head.

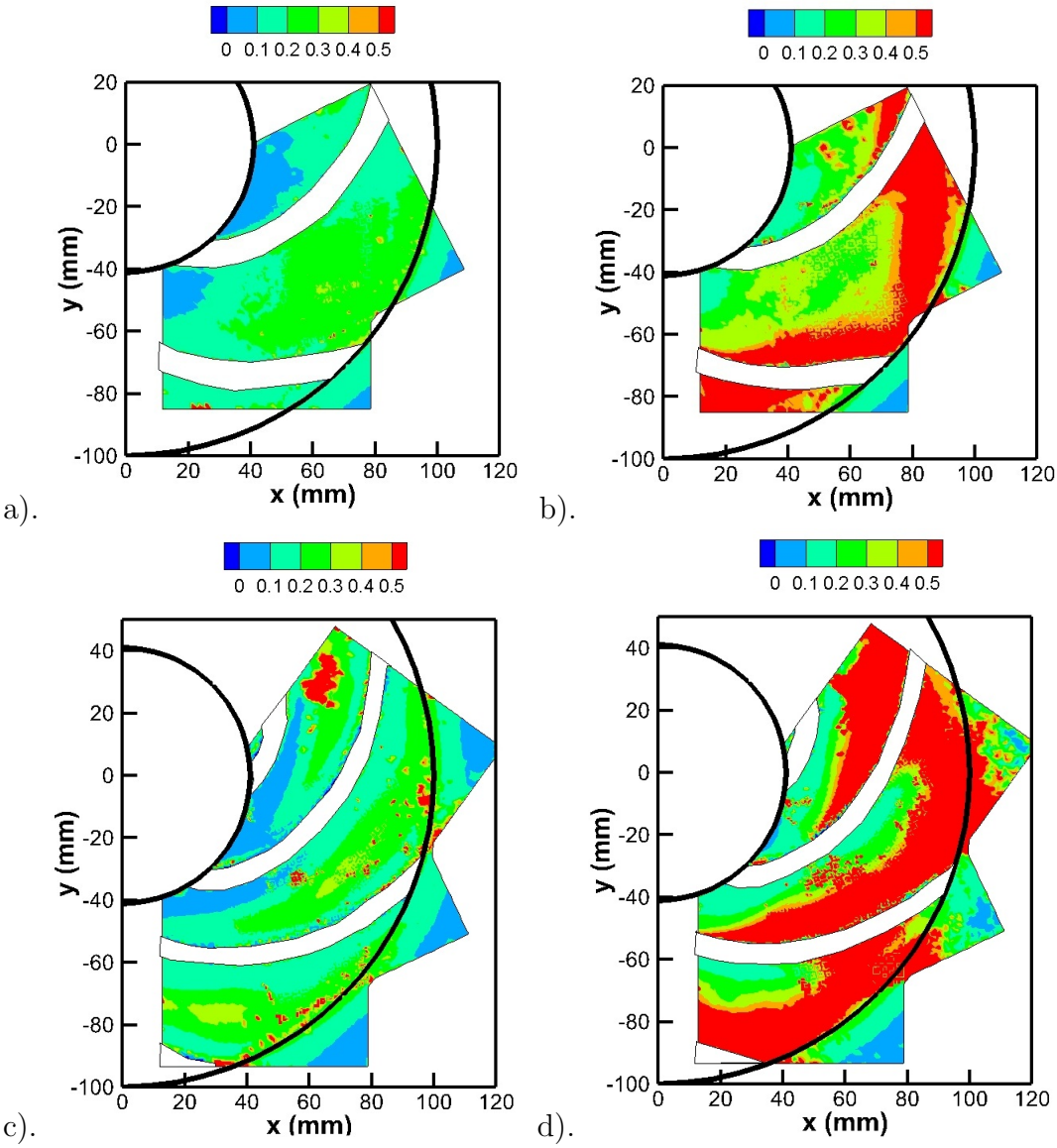

Figure 4.36: Fluid flow turbulence intensity inside the impeller passage for a) 5 bladed impeller 50% flow rate, b) 5 bladed impeller 25% flow rate, c) 7 bladed impeller 50% flow rate, d) 7 bladed impeller 25% flow rate

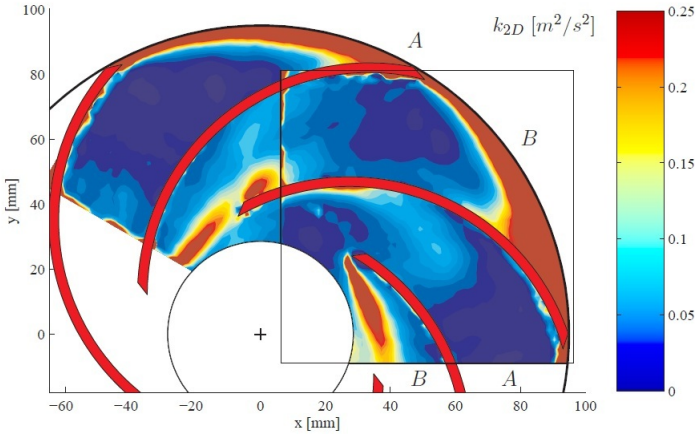

Figure 4.37: Turbulence intensity (TI) at the quarter flow rate obtained by Pedersen [33]

Fluid angle deviation (β_d)at 50 % and 25 % flow rates

Fluid angle deviation (β_d) contours at 50% flow rate for the 5 and 7 bladed impellers are presented in figure 4.38a and 4.38c. Different to the design flow rate, at 50% flow rate, the relatively high positive β_d is not found at the inlet of the flow. However, the relatively high negative β_d is found in the middle of the passage which indicates the bulk flow influence at the inlet is reduced and the fluid starting to be distorted because of the fluid detached on the blade suction and pressure sides. In addition, since the flow rate is decreased to a condition that slip becomes very influence on the flow, the zero contour line is very difficult to obtain.

At 25% flow rate, the results of β_d show that the fluid is now more complex. The high negative β_d lies on the blade suction side from inlet toward outlet impeller as indication of the wake region on the blade suction surface shown in the streamlines subsection. The high positive β_d is found on the trailing edge of the blade suction side and it lies from the blade suction side to blade pressure side. This might lead to a sign of a vortex region that lies on the trailing edge of the blade suction side. A similar vortex region on the trailing edge was found in an experiment conducted by Murakami *et al.* [32] as shown in figure 4.30. The vortex might be created from fluid flow that exit from the blade pressure side of the passage in front of it. Then, because the region of the blade suction side has a very low pressure, the exit flow enters the passage in behind [32]. This pattern is not showing at the streamline results because the streamlines were obtained based on all of the vectors in the map. The vectors outside the passage have a greater influence on the streamlines

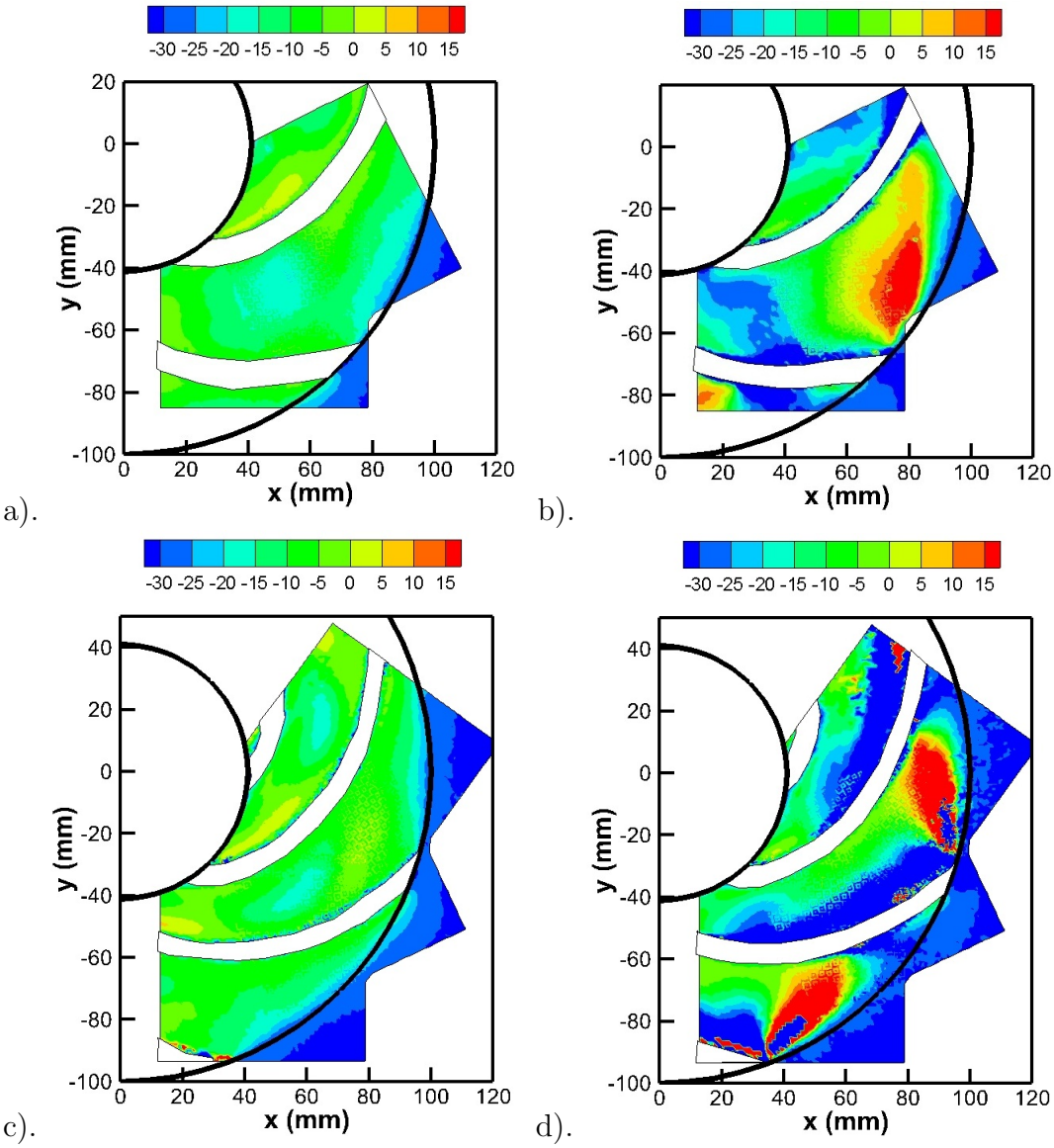

Figure 4.38: Fluid angle deviation in the impeller passage for a) 5 bladed impeller 50% flow rate, b) 5 bladed impeller 25% flow rate, c) 7 bladed impeller 50% flow rate, d) 7 bladed impeller 25% flow rate

calculation, so this vortex region is probably hidden.

Similar to the streamlines and TI results, the results of the β_d also show that at low flow rates, an identical flow structure is found between passages. If the two-channel phenomena exist in the impeller passages the β_d contour will be similar as the results found by Pedersen [33] shown in figure 4.39. Pedersen results showed that the high negative fluid angle deviation lay on the blade suction side at the impeller inlet and at the middle of blade pressure surface for the stall passage. In this study, however, a similar fluid angle deviation pattern is shown in each passage of the impeller. It can be concluded that the impeller geometry and the experimental set up has an important role in the fluid structure at low flow rates.

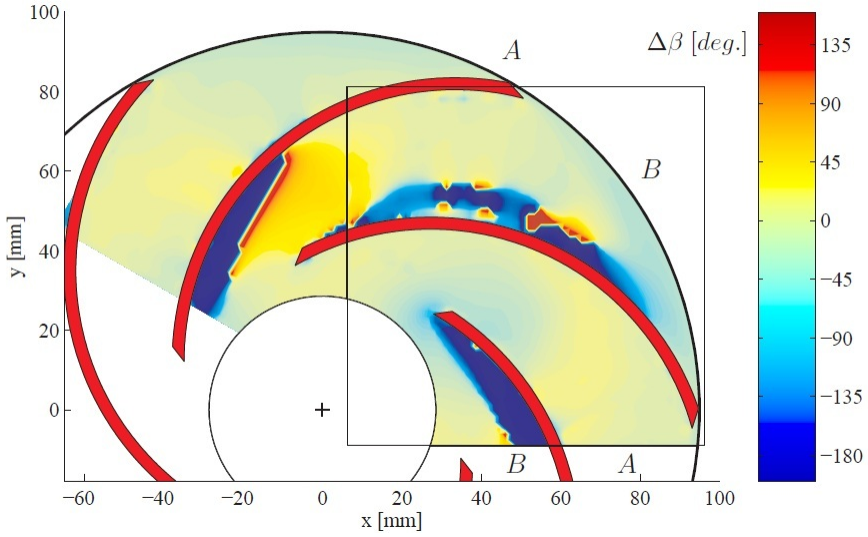

Figure 4.39: Fluid angle deviation at quarter load design results by Pedersen [33]

At the 50% flow rate, the results of β_d are difficult to be compared. However at 25% flow rate, the contour map of β_d shows some differences between the 5 and 7 bladed impellers at low flow rates. It shows that the region of the relatively high negative β_d which attaches on the blade suction side is larger for the 7 bladed impeller. The results also show that the region of the high positive β_d on the trailing edge of the blade suction side for the 7 bladed impeller is larger. Hence, the 7 bladed impeller might have a more complex 3D flow structure compared to the 5 bladed impeller.

4.2.6 Summary of PIV results

In this study, PIV measurements were conducted to observe the fluid structure at the design, high and low flow rates of the 5 and 7 bladed impellers. The analysis was done by observing the characteristic of primary and secondary relative velocity profile, turbulence intensity, fluid flow angle and streamlines of flow inside the design impellers. At the design and 75% flow rate conditions, the component of primary and secondary velocity profiles showed that flow structure in a passage of the 5 and 7 bladed impellers was very identical to the potential flow theory near the impeller inlet as shown in figure 4.15. However, the flow then, became distorted and the potential flow was weakened when the fluid flow moved toward the impeller outlet and a jet pattern was created. A similar relative velocity profile also found in past experiments conducted by Murakami *et al.* [32], Hesse and Howard [18], Pedersen [33], Westra *et al.* [44] and Keller *et al.* [24]. The results also showed that there was no strong evidence of a wake on the trailing edge of the blade suction side. The primary velocity component shows that at 75% flow rate, the jet pattern becomes stronger than the design flow rate as a result of viscous effects, passage geometry and Coriolis effects [32][18][33]. This results was validated when observing the fluid close to the blade suction and pressure sides that the inlet velocity decreases near the impeller inlet then the velocity increases near the impeller outlet.

Moreover, the results showed that the influence of the secondary component on the fluid structure near the blade pressure and suction surface was very low. The influence of the secondary component increased in the middle of the passage. The secondary component confirmed that close to the impeller inlet, the flow structure agreed with the potential flow theory but near the impeller outlet the potential flow weakened.

At the design and 75% flow rates, the results showed that the relative velocity of fluid inside the 5 and 7 bladed impellers increased from the inlet to the outlet meaning that the kinetic energy increased. It was validated by the head rise calculation shown in figure 4.14. The results also showed that the 7 bladed impeller produced higher head rise to the fluid. In addition, the results showed that when the flow rate was decreased from the design flow rate, the losses that was caused by the mismatch of fluid angle and the blade curvature increased.

The influence of the number of blades on the fluid structure was shown at the design flow rate. Unlike the fluid structure inside the 5 bladed impeller, there was a flow detached at the blade pressure side shown in the streamline inside the 7 bladed impeller. The separation flow was probably caused by high inlet velocity because of the passage geometry. Then, the high inlet velocity might lead the high 'angle of attack' of the fluid at the impeller inlet. The evidence of the high 'angle of attack' was shown in fluid angle deviation results

at the design flow rate.

At high flow rates, the results showed that the jet pattern weakened and the flow along the passage tends to agree with the potential flow. Moreover, the results showed that the 'true channel' shown in the fluid angle deviation contour became narrower compared to the 'true channel' at the design flow rate. Hence, the losses because of the mismatch of the fluid flow and blade angle appeared to decrease. The current studies and past studies showed that at high flow rates, the number of blades on the flow structure became less of an influence. Keller *et al.* [24] and Westra [43] that conducted PIV measurements at very high flow rates also confirmed that high fluid velocity lay along the blade suction side to the outlet of the blade pressure side. High flow turbulence was shown attached the blade pressure side as a result of detached flow.

At 50% flow rate, the results showed that there was evidence of jet-wake phenomena for the 5 and 7 bladed impellers. In addition, at low flow rate, the turbulence intensity increased which inferred that the fluid losses increased. At 25% flow rate, the results showed that there was a separation flow at the blade suction surface starting near the impeller inlet and there was also a separation flow at the blade pressure surface near the impeller outlet. Moreover, the results showed that when the flow rate was decreased from the design flow rate, the influence of impeller geometry and experimental setup became stronger. Past studies conducted by Pedersen [33] showed that at quarter load of a six bladed impeller, the two channel phenomena occurred in the passages. However, in this study, the two channel phenomena did not appear. A similar flow pattern was shown in an experiment conducted by Murakami *et al.* [32] that also used the 7 bladed impeller. The results of fluid angle deviation showed that the high positive β_d appeared on the trailing edge of the blade suction side. This might be a vortex region that was also found in Murakami *et al.* [32]. The 7 bladed impeller has a larger vortex region on the trailing edge compared to the 5 bladed impeller. Since the results between this study and past studies were different in the flow structure at low flow rate, it appeared that the influence of the number of blades on the fluid behavior at low flow rates became stronger compared with the design flow rate.

Chapter 5

Conclusions and Recommendations

5.1 Conclusions

In this study, experiments to obtain the impeller performance and PIV measurements to understand the flow behavior of the impellers which have different number of blades at several flow rates were conducted. This research observed the performance and flow behavior inside the passages of 5 and 7 bladed impellers. The impellers were closed back-swept blade impellers with a constant blade angle of 30^o. A newly constructed test rig impeller was built to measure impeller performance and conduct PIV measurements. For the PIV measurements, calibration tools were built to obtain the actual size of the image. Since PIV measurements only obtained the absolute velocity, calculations were performed to obtain the fluid relative velocity.

As expected, the performance results of both impellers showed that the head decreased when the flow rate was increased which is a characteristic of a centrifugal back-swept impeller. The experiment also was conducted to validate the similarity of a pump by testing the impellers performance at 200-500 rpm. The performance results at several impeller speeds showed satisfactory agreement with the similarity laws. The maximum efficiency at several impeller speeds were around 66%. Moreover, the performance results showed that the 7 bladed impeller produced a higher head compared to the 5 bladed impeller. However, the maximum efficiency was similar; the results showed that the best efficiency of the 5 and 7 bladed impellers was 66% and 67.5%, respectively. However at low flow rates, the 7 bladed impeller had lower efficiency as a result of high recirculation losses which was also seen in the PIV results.

The PIV measurements revealed the fluid structure inside the passage of the 5 and 7 bladed impellers at several flow rates. Primary and secondary relative velocity profiles, turbulence intensity, fluid flow angle and streamlines illustration were observed to determine the fluid flow structure of both impellers. The results showed that the number of blades were less of an influence on the flow structure at very high flow rate. However, the number of blades started to show an influence on the flow structure at the design flow rate and the influence became stronger at low flow rates. The turbulence intensity contours showed that the minimum value was at the design flow rate but it increased at low and high flow rates which implied that low flow rates produced more losses in the flow. The fluid flow angle deviation results showed that the largest loading region which was inside the zero contour line was at the very high flow rate which means that the least influence of the losses caused by a mismatch of the fluid angle and blade curvature was at high flow rates. The magnitude of turbulence intensity is higher at the 7 bladed impeller compared to the 5 bladed impeller so although the 7 bladed impeller had a higher energy transfer, the losses produced were also higher. Therefore, the efficiency between two impellers was not too different. In conclusion, PIV results showed agreement with the performance results.

At the design flow rate, a well behaved flow structure occurred inside the 5 bladed impeller. By comparison, separation flow occurred on the blade pressure side of the 7 bladed impeller. The separation flow caused the fluid more fluctuate as a result the turbulence losses increased. It has been discussed in Chapter 4, separation flow might be prevented by reducing the blade curvature. However, past studies reported that skin friction increased. Therefore, to obtain optimum performance of the impeller, optimization should be conducted to obtain appropriate blade numbers and blade angle curvature.

5.2 Recommendations

In this study, collecting the performance data used a Keithley Model 2700 with module 7000 multiplexer which is a mechanical data acquisition system. The acquisition equipment cannot collect all the data simultaneously because it needs to switch each channel measurement. The problem was when it switched from measuring current to VDC, the first measurement did not collect the true value. Hence, the measurements had to be repeated. In the future, collecting data should be used an acquisition card that can collect all of the data simultaneously. This system can give benefit by collecting the data at the determined impeller position so the data will be more related.

In this study, the impeller is designed closer to a mixed pump type because the n_s is 0.7. In the next study, the impeller should be designed with low n_s so it can be compared

more properly with other research that used a low specific speed impeller. To obtain low n_s, the blade height can be reduced or the impeller diameter can be larger. In addition, the inlet shroud diameter can also be reduced to restrict the inlet flow.

The fluid structure of all of the impeller passages can be observed when it interacts with a volute. It will be interesting to study the fluid structure at low flow rates because the impeller geometry and the volute has a strong influence at low flow rates. However, a new volute which should be stiff and clear so it can accommodate the PIV measurements.

It is interesting to observe the flow structure in several measurement planes or 3D PIV. In this study, parallax error is assumed to be negligible, stereo PIV can be done to observe the flow structure in several measurement planes. The phase-averaged flow variables can be obtained through stereo PIV.

In this study, the velocity component resulting from PIV measurements were fluid absolute velocity. The actual fluid velocity was obtained by subtracting the absolute velocity with the impeller tangential velocity. This happened because the camera was mounted on a bracket which was stationary. To obtain the relative velocity directly without involving a vector calculation, the camera should rotate at the impeller speed. The problem might occur when sending a trigger signal from the timer box to the camera or sending images from the camera to the computer. It needs equipments to send an electric signal from rotating equipment to static equipment or vice versa. A slip ring is one example of equipment which can be used to transfer an electric signal and image data from rotating to stationer equipment. In addition, wireless technology can also be used to transfer the signal or image data.

Lastly, as mentioned previously, study about optimization of blade number and blade angle curvature can be done. The study can be numerically then the results can be validated experimentally. Since impeller can be manufactured easily with facilities in the university and new experiment test rig was designed so that it is easy to install to the rig, this study become a potential research in the future.

APPENDICES

Appendix A

Uncertainty analysis

Determining the error of measurements is complicated because the actual value of the measurements is unknown. Therefore, the best way to predict the deviation of measurement reading is using the uncertainty approach. The value of the uncertainty each measurement can be sourced from instruments, measurement techniques and random error from environment which can excite the measurement value, etc. The best way to estimate the uncertainty is using root sum square of all of uncertainty sources. Total uncertainty must be calculated starting from design uncertainty (U_c), first order uncertainty (U_0) to N^{th} uncertainty (U_N). The expression of the uncertainty in this study can be

$$U_N = \pm \left[{U_c}^2 + \left(\sum_{i=0}^{N-1} {U_i}^2 \right) \right]^{\frac{1}{2}} \tag{A.1}$$

where U_c is expressed by

$$U_c = \pm \left[U^2_{\text{accuracy instrument}} + U^2_{\text{resolution instrument}} \right]^{\frac{1}{2}} \tag{A.2}$$

However, since U_c from the head, flow, voltage and current measurements which were stated in Chapter 3 was not significantly high compared to the reading uncertainty, so the U_c from those measurements can be neglected. The available U_c was sourced only from the tachometer which measured the impeller speed.

A.1 Uncertainty of pump performance measurements

Since U_c for measuring all of performance parameters can be neglected, the uncertainty was only sourced from experimental reading. In this section, an example will give to calculate the uncertainty which is stated as error bars in figure 4.1 as well as the uncertainty statement in Chapter 4. The example given was the uncertainty calculation for efficiency at the design flow rate of the 5 bladed impeller. At 300 rpm, the known uncertainty with 95 % of confidence level are $U_H = 1.2$ % $U_Q = 5.4$ % $U_V = 0.1$ % $U_I = 1.7$ %. Therefore, the relative uncertainty $\frac{U_\eta}{\eta}$ can be

$$\frac{U_\eta}{\eta} = \pm \left[{U_H}^2 + {U_Q}^2 + {U_V}^2 + {U_I}^2 \right]^{\frac{1}{2}}$$

$$\frac{U_\eta}{\eta} = \pm \left[1.2\%^2 + 5.4\%^2 + 0.1\%^2 + 1.7\%^2 \right]^{\frac{1}{2}}$$

$$\frac{U_\eta}{\eta} = \pm 5.8\%$$

The efficiency of the 5 bladed impeller at the design flow rate and 300 rpm was 66.0%. Therefore, the uncertainty for this example is

$$U_\eta = 66 \pm 3.8 \ \%$$

The most contribution of the uncertainty comes from the flow meter measurement. However, it could be reduced by taking more flow rate measurements. Because of the limited time of this research and still acceptable uncertainty level, the flow measurements was not taken any longer.

A.2 Uncertainty of PIV measurements

Velocity calculations were conducted to be used for analysis when discussing in the PIV results. To obtain the uncertainty in the PIV measurements was complicated because it was difficult to state the design uncertainty. To determine the design uncertainty, most of the considerations was referred to several past research in PIV measurements.

It has been also mentioned in section 2.2 that to obtain small error in PIV measurements, the particles must be chosen big enough but still follows the flow. The diameter of particles should be in the range of 1-2 pixels and achieved minimum around 2 pixels [41].

This study used about 50 μm particles which was around the acceptable range. Another consideration is the number of particles in each interrogation area. Based on Monte Carlo Simulations [40], the recommendation number of particles in each interrogation area are 5 particles. More over, if there are 8 particles each interrogation area the error is estimated around 4% [3]. Furthermore, the impeller was designed to be 2D so it was predicted that the out of plane error was not significant. The impeller speed was measured by stroboscope which has accuracy about 1% and resolution 0.1%. Since the stroboscope accuracy is dominated the error, the relative uncertainty that contributes to the angular velocity was about 1%. In conclusion, the design uncertainties which will be involved in the uncertainty calculation are number of particles error prediction and the stroboscope uncertainty.

The calculation such as W_p, W_s, $\frac{W_p}{u_2}$ and $\frac{W_s}{u_2}$ were obtained for analysis in PIV results. The uncertainty calculation for W_p were conducted within 1000 image pair results. Then, W_p the uncertainty was calculated from the standard deviation of velocity measurements. The calculation example of W_p uncertainty below is done for the 5 bladed impeller at 300 rpm, $\theta = 75^o$ and R = 80 mm. The W_p uncertainty at that point can be

$$W_r = w_x \cos\theta - w_y \cos\alpha$$

$$W_t = w_x \cos\alpha + w_y \cos\theta$$

$$W_p = w_t \cos 30^o + w_r \sin 30^o$$

$$W_p = 0.86 w_t + 0.5 w_r$$

$${S_{w_p}}^2 = (0.86 S w_x + 0.5 S w_y)^2$$

$${S_{w_p}}^2 = 0.74 {S w_x}^2 + 0.25 {S w_y}^2 + 0.86 S w_x S w_y$$

where the uncertainty of the relative velocities in x and y coordinates with 95% confidence level are

$$S_{w_x} = 0.14 m/s$$

$$S_{w_y} = 0.04 m/s$$

then

$${S_{w_p}}^2 = 0.74 0.14^2 + 0.25 0.04^2 + 0.86 0.14 0.04$$

$${S_{w_p}}^2 = 0.02 m/s$$

$$U_{w_p} = {S_{w_p}}^2 = 0.02 m/s$$

if W_p at this point is 1.24 m/s, so the relative uncertainty of W_p is

$\frac{U_{w_p}}{w_p} = \pm 1.63\%$ The relative uncertainty of the u_2 was come from the tachometer which the relative uncertainty is 1%. Hence, the relative uncertainty of $\frac{W_p}{u_2}$ can be

$$\frac{U_{\frac{W_p}{u_2}}}{\frac{W_p}{u_2}} = \pm \left[{U_{w_p}}^2 + {U_{u_2}}^2 \right]^{\frac{1}{2}}$$

$$\frac{U_{\frac{W_p}{u_2}}}{\frac{W_p}{u_2}} = \pm \left[1.61\%^2 + 1\%^2 \right]^{\frac{1}{2}}$$

$$\frac{U_{\frac{W_p}{u_2}}}{\frac{W_p}{u_2}} = \pm \left[1.91\% \right]$$

At this point $\frac{W_p}{u_2} = 0.39$ m/s, so the uncertainty of $\frac{W_p}{u_2} = 0.39$ m/s $\pm \left[1.91\% \right]$ or 0.39 $\pm \left[0.007 \right]$ m/s

Appendix B

Performance result charts

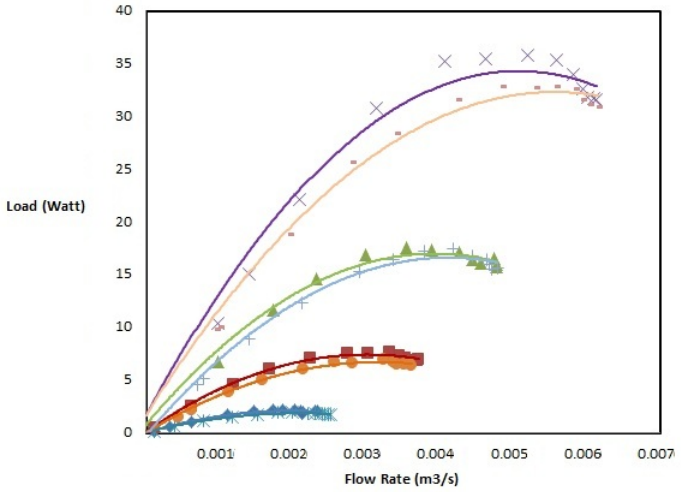

Figure B.1: WHP Performance curves of the 5 bladed impeller at: $\times$ 500 rpm; $\triangle$ 400 rpm; $\square$ 300 rpm; $\diamond$ 200 rpm and the 7 bladed impeller at :$-$ 500 rpm; $+$ 400 rpm; $\circ$ 300 rpm; $*$ 200 rpm

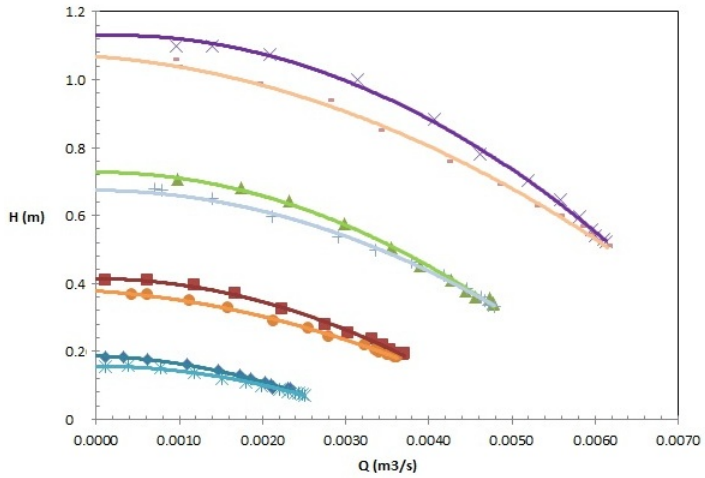

Figure B.2: H-Q Performance curves of the 5 bladed impeller at: $\times$ 500 rpm; $\triangle$ 400 rpm; $\square$ 300 rpm; $\diamond$ 200 rpm and the 7 bladed impeller at :$-$ 500 rpm; $+$ 400 rpm; $\circ$ 300 rpm; $*$ 200 rpm

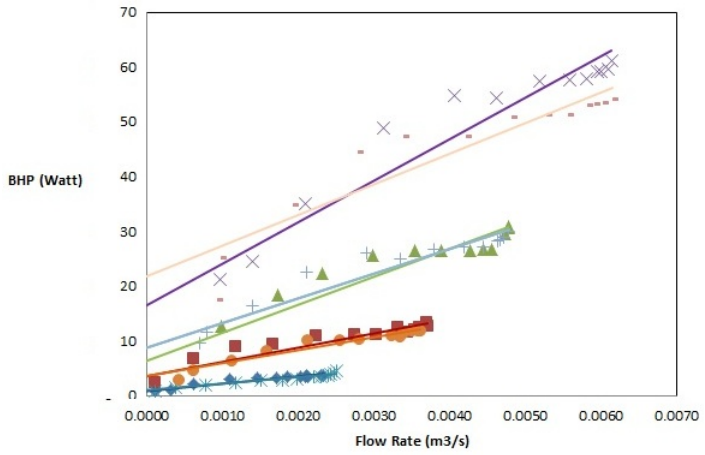

Figure B.3: BHP curves of the 5 bladed impeller at: $\times$ 500 rpm; $\triangle$ 400 rpm; $\square$ 300 rpm; $\diamond$ 200 rpm and the 7 bladed impeller at :$-$ 500 rpm; $+$ 400 rpm; $\circ$ 300 rpm; $*$ 200 rpm

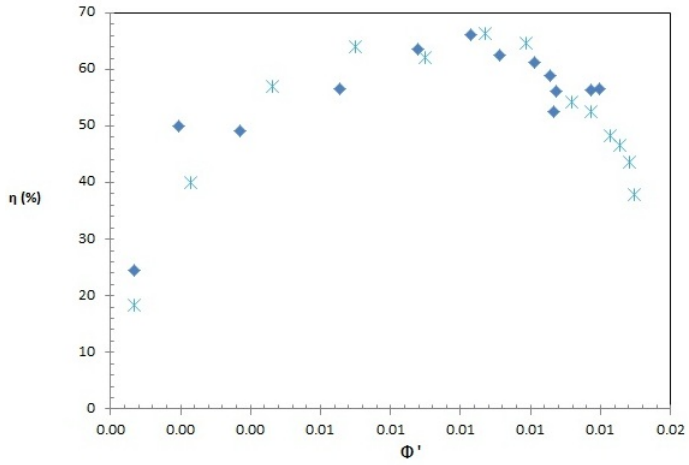

Figure B.4: efficiency curves of the 5 bladed impeller at $\diamond$ 200 rpm and the 7 bladed impeller at $*$ 200 rpm

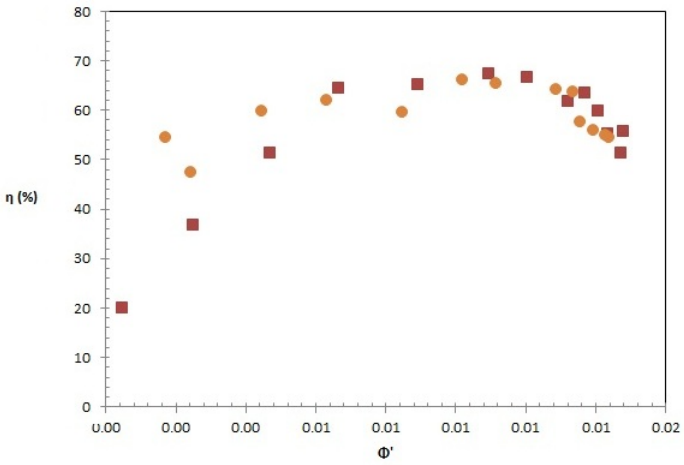

Figure B.5: Efficiency curves of the 5 bladed impeller at $\square$ 300 rpm and the 7 bladed impeller at$\circ$ 300 rpm

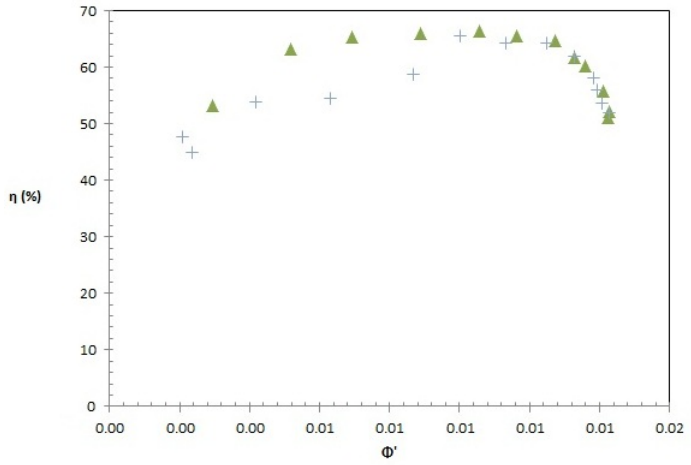

Figure B.6: Efficiency curves of the 5 bladed impeller at$\triangle$ 400 rpm and the 7 bladed impeller at + 400 rpm

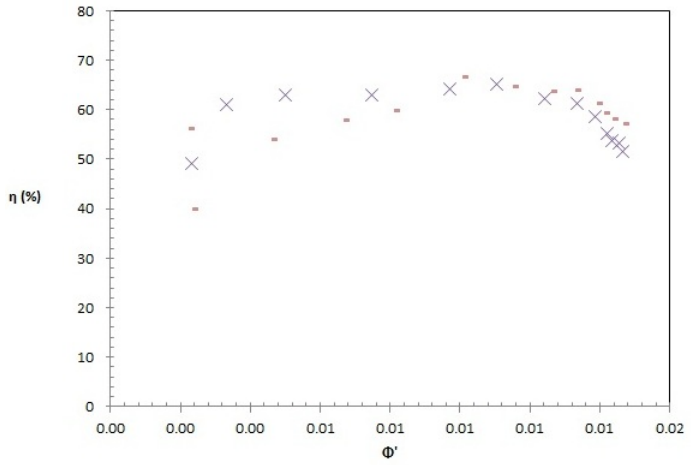

Figure B.7: Efficiency curves of the 5 bladed impeller at $\times$ 500 rpm and the 7 bladed impeller at $-$ 500 rpm

Appendix C

Other PIV results

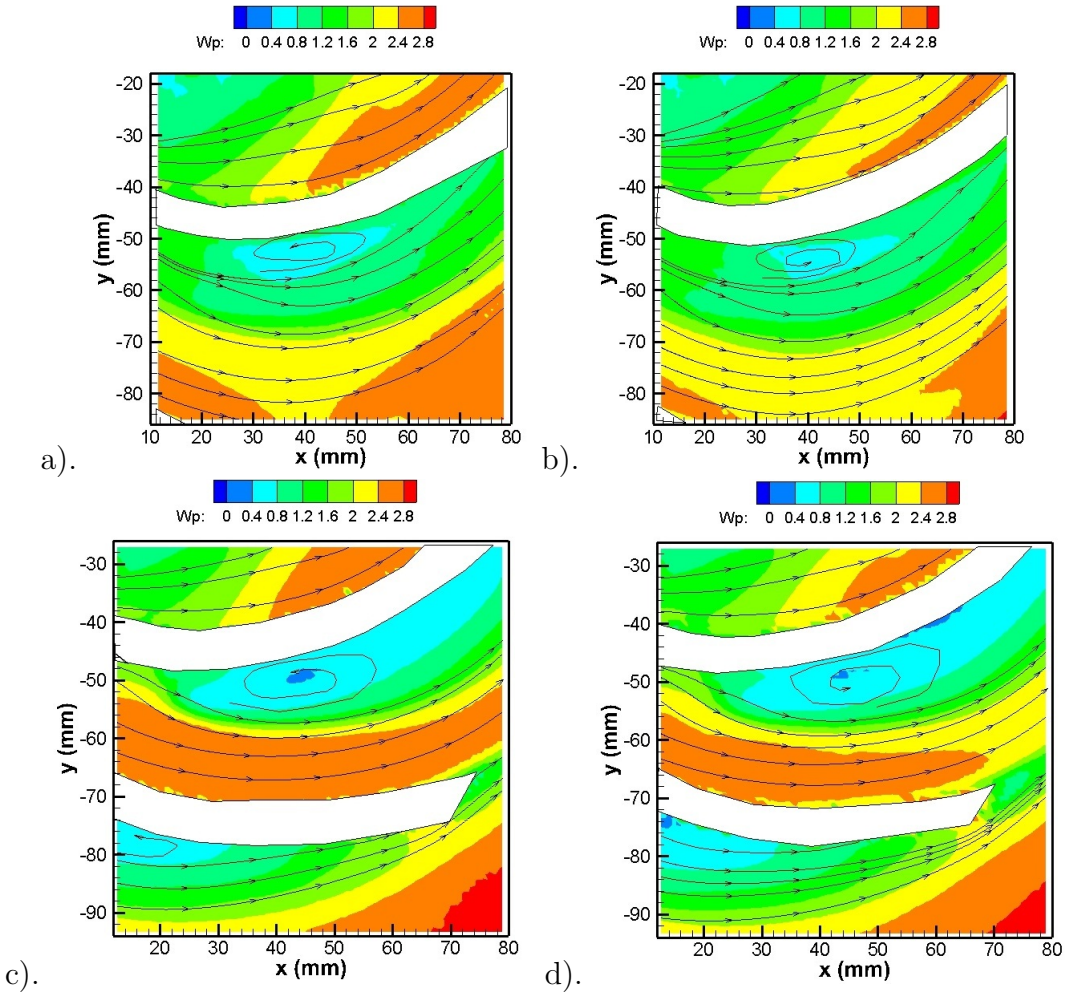

Figure C.1: Fluid flow normalized streamlines for a) 5 bladed impeller 140% flow rate t_d 15 ms, b) 5 bladed impeller 120% flow rate t_d 15 ms, c) 7 bladed impeller 140% flow rate t_d 15 ms, d) 7 bladed impeller 120% flow rate t_d 15 ms

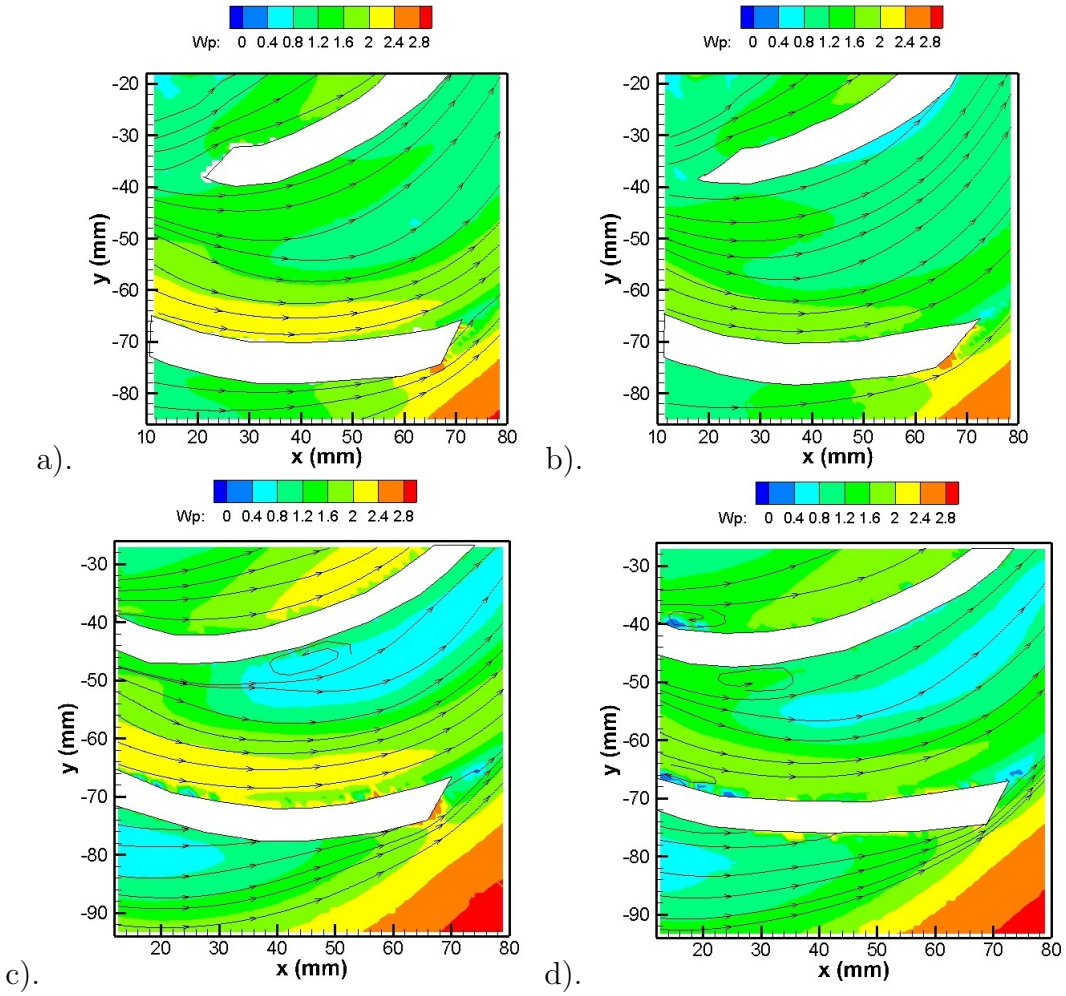

Figure C.2: Fluid flow normalized streamlines for a) 5 bladed impeller 100% flow rate t_d 0 ms, b) 5 bladed impeller 75% flow rate t_d 0 ms, c) 7 bladed impeller 100% flow rate t_d 15 ms, d) 7 bladed impeller 75% flow rate t_d 15 ms

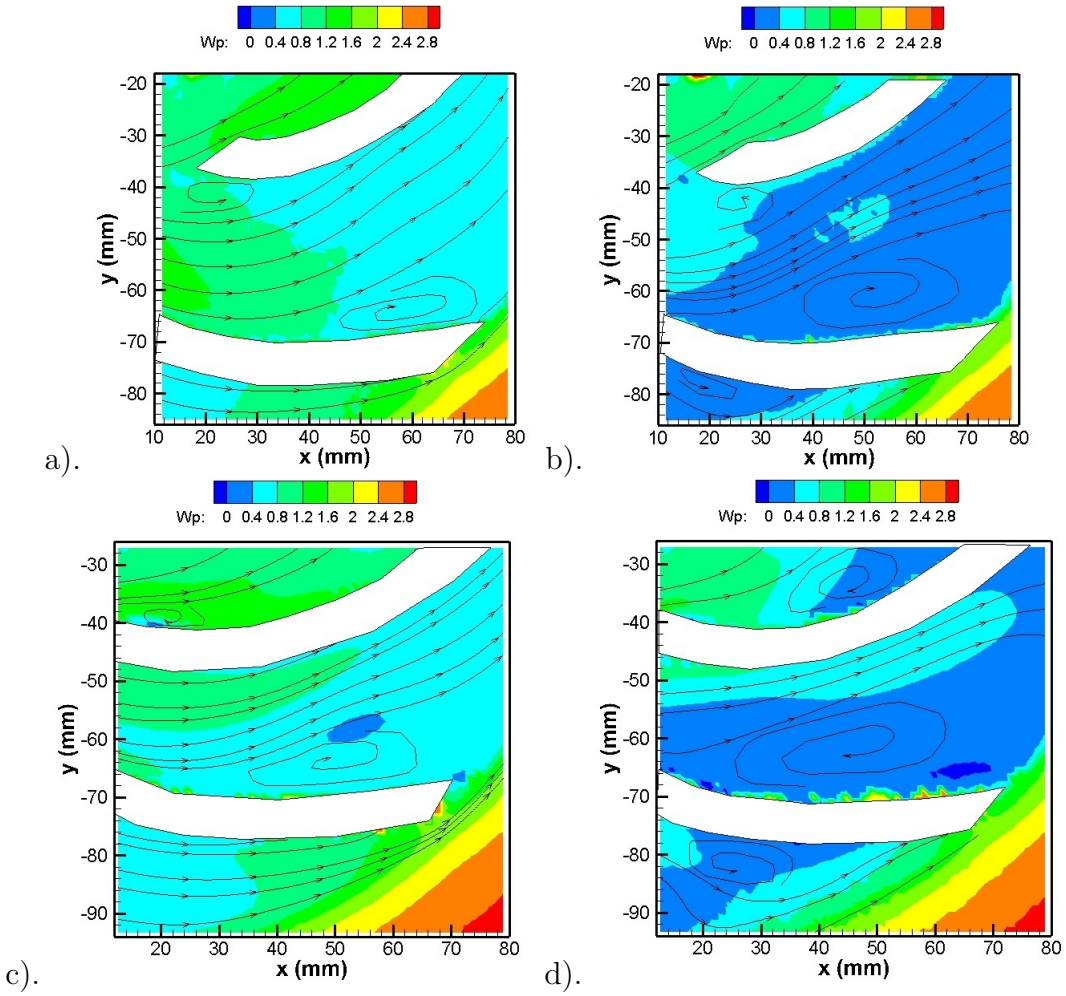

Figure C.3: Fluid flow normalized streamlines for a) 5 bladed impeller 50% flow rate t_d 0 ms, b) 5 bladed impeller 25% flow rate t_d 0 ms, c) 7 bladed impeller 50% flow rate t_d 15 ms, d) 7 bladed impeller 25% flow rate t_d 15 ms

References

[1] M. Abramian and J. H. G. Howard. Experimental investigation of the steady and unsteady relative flow in a model centrifugal impeller passage. *Journal of Turbomachinery*, 116(2):269–279, Apr 1994.

[2] A. Akhras, M. El Hajem, R morel, and J.Y. Champagne. The internal flow investigation of a centrifugal pump. *10 th International Symposium on Application of Laser Techniques to Fluid Mechanics*, 10:28.5.1–28.5.9, 2000.

[3] Ammar Mohammadnour Altaf. Experimental investigation of the flow behaviour inside a centrifugal impeller channel at design and off-design flow rates. Master's thesis, University of Waterloo, 2007.

[4] E.C. Bacharoudis, A.E. Filios, M.D. Mentzos, and D.P. Marfaris. Parametric study of a centrifugal pump impeller by varying the outlet blade angle. *The Open Mechanical Engineering*, 2:75–83, 2008.

[5] O.E. Balje. *Turbomachines: A Guide to Design Selection and Theory*. A Wiley-interscience publication. Wiley, 1981.

[6] Sepideh Behseta. Off-design condition analysis of a centrifugal impeller. Master's thesis, University of Waterloo, 2005.

[7] S. Chakraborty and K.M. Pandey. Numerical studies on effects of blade number variations on performance of centrifugal pumps at 4000 rpm. *International Journal of Engineering and Technology*, 3(4):410 – 416, August 2011.

[8] Young-Do Choi, Junichi Kurowa, and Jun Matsui. Performance and internal flow characteristics of a very low specific speed centrifugal pump. *Journal of Fluids Engineering*, 128(2), 2006.

[9] Controlotron Corporation. *Field manual System 990 Uniflow universal clamp-on NEMA flow meter Multi pulse, transit time system*, 1989.

[10] Cui Dai and Liang Dong. Flow in a low specific speed centrifugal pump using piv. *Advances in Mechanical Engineering*, 5, 2013.

[11] Susanta K. Das. Experimental performance evaluation of a centrifugal pump with different impeller vane geometries. In *Proceedings of ASME 2014 International Mechanical Engineering Congress and Exposition*, volume 7: Fluid Engineering System and Technologies, page V007T09A096; 6 pages. ASME, 2014.

[12] R. Dong, S. Chu, and J. Katz. Quantitative visualization of the flow within the volute of a centrifugal pump. part a: Technique. *Journal of Fluids Engineering*, 114(3):390–395, Sep 1992.

[13] R. Dong, S. Chu, and J. Katz. Quantitative visualization of the flow within the volute of a centrifugal pump. part b: Results and analysis. *Journal of Fluids Engineering*, 114(3):396–403, Sep 1992.

[14] Talib Z. Farge and Mark W. Johnson. Effect of flow rate on loss mechanisms in a backswept centrifugal impeller. *International Journal of Heat and Fluid Flow*, 13(2):189 – 196, 1992.

[15] R.W. Fox, A.T. McDonald, and P.J. Pritchard. *Introduction to Fluid Mechanics*. Wiley, 2009.

[16] M. Hajem, R. Morel, and Champagne. Detailed measurements of the internal flow of a backswept centrifugal impeller. *9 th International Symposium on Application of Laser Techniques to Fluid Mechanics*, 9:36.2.1–36.2.6, 1998.

[17] C. P. Hamkins and R. D. Flack. Laser velocimeter measurements in shrouded and unshrouded radial flow pump impellers. *Journal of Turbomachinery*, 109(1):70–76, Jan 1987.

[18] Nicholas H. Hesse and J. H. G. Howard. Experimental investigation of blade loading effects at design flow in rotating passages of centrifugal impellers. *Journal of Fluids Engineering*, 121(4):813–823, Dec 1999.

[19] Liu Houlin, Wang Yong, Yuan Shouqi, Tan Minggao, and Wang Kai. Effects of blade number on characteristics of centrifugal pumps. *Chinese of Journal of Mechanical Engineering*, 23:1–6, 2010.

[20] Keithley Instrument.Inc. *Model 2700 Multimeter/Switch sytem user's manual*. Keithley Instrument.Inc, Cleveland Ohio, U.S.A, 8 2011. An optional note.

[21] David A Johnson. *Turbomachines ME 563 Lecture Notes*. University of Waterloo, 2014.

[22] I.J. Karassik. *Pump Handbook*. Harvard Business Review Bks. McGraw-Hill, 2001.

[23] Jens Keller. *Fluid-dynamic fluctuations and flow structures in centrifugal pumps due to rotor stator interaction*. PhD thesis, Universidad de Oviedo.

[24] Jens Keller, Eduardo Blanco, Ral Barrio, and Jorge Parrondo. Piv measurements of the unsteady flow structures in a volute centrifugal pump at a high flow rate. *Experiments in Fluids*, 55(10), 2014.

[25] Wen-Guang Li. *Influence of the number of impeller blades on the performance of centrifugal oil pumps*. World Pumps. Elsevier Scinece Ltd, 2002.

[26] Wen-Guang Li. Effect of exit blade angle viscosity and roughness in centrifugal pumps investigated by cfd computation. In *Task Quarterly*. CI Task, 2011.

[27] Wen-Guang Li. Effects of blade exit angle and liquid viscosity on unsteady flow in centrifugal pumps. In *Proceedings of the Institutuion of Mechanical Engineers*. SAGE, 2012.

[28] Wen-Guang Li. Effects of flow rate and viscosity on slip factor of centrifugal pump handling viscous oils. *International Journal of Rotating Machinery*, 2013(317473):12, 2013.

[29] A Melling. Tracer particles and seeding for particle image velocimetry. *Measurement Science and Technology*, 8(12):1406, 1997.

[30] Mohamad Memardezfouli and Ahmad Nourbakhsh. Experimental investigation of slip factors in centrifugal pumps. *Experimental Thermal and Fluid Science*, 33(5):938 – 945, 2009.

[31] S. M. Miner, R. J. Beaudoin, and R. D. Flack. Laser velocimeter measurements in a centrifugal flow pump. *Journal of Turbomachinery*, 111(3):205–212, Jul 1989.

[32] M. Murakami, K. Kikuyama, and E. Asakura. Velocity and pressure distributions in the impeller passages of centrifugal pumps. *Journal of Fluids Engineering*, 102(4):420–426, Dec 1980.

[33] Nicholas Pedersen. *Experimental Investigation of Flow Structures in a Centrifugal Pump Impeller Using Particle Image Velocimetry*. PhD thesis, Fluid Mechanics Department of Engineering Technical University of Denmark, 2000.

[34] Nicholas Pedersen, Poul S. Larsen, and Christian B. Jacobsen. Flow in a centrifugal pump impeller at design and off-design conditions part i: Particle image velocimetry (piv) and laser doppler velocimetry (ldv) measurements. *Journal of Fluids Engineering*, 125(1):61–72, Jan 2003.

[35] Sean Peterson. *Experimental Methods of Fluid Mechanics ME 770 Lecture Notes*. University of Waterloo, 2014.

[36] M. Raffel, C.E. Willert, and J. Kompenhans. *Particle Image Velocimetry: A Practical Guide*. Engineering online library. Springer, 1998.

[37] George F. Round. *Incompressible Flow Turbomachines:Design, Applications, and Theory*. Butterworth Heinemann, 2004.

[38] Toru Shigemitsu, Juniro Fukutomi, and Kensuke Kaji. Influence of blade outlet angle and blade thickness on pump performance and internal flow of mini centrifugal pump. In *Proceeding ASME Digital collection*, volume 1, pages 179–185, Japan, 2011. ASME-JSME-KSME 2011 Joint Fluids Engineering Conference.

[39] M. H. Shojaeefard, M. Tahani, M. B. Ehghaghi, M. A. Fallahian, and M. Beglari. Numerical study of the effects of some geometric characteristics of a centrifugal pump impeller that pumps a viscous fluid. *Computers & Fluids*, 60:61–70, May 2012.

[40] Dantec Measurement Technology. *Flow Map Particle Image Particle Velocimetry Instrumentation, Installation and User's Guide*. Engineering online library. Dantec Dynamics, Copenhagen, Denmark, 1999.

[41] Ulrik Ullum. *Imaging techniques for planar velocity and concentration measurements*. PhD thesis, Technical University of Denmark, 1999.

[42] Varley and F A. Effects of impeller design and surface roughness on the performance of centrifugal pumps. *Proceedings - Institution of Mechanical Engineers*, 175:955–989, 1961.

[43] Remko Willem Westra. *Inverse-design and optimization methods for centrifugal pump impellers*. PhD thesis, University of Twente.

[44] R.W. Westra, L. Broersma, K. Van Andel, and N.P. Kruyt. Piv measurements and cfd computations of secondary flow in a centrifugal pump impeller. *Journal of Fluids Engineering*, 132(6), 2010.

[45] Frank M. White. *Fluid Mechanics*. McGraw Hill, Reading, Massachusetts, 2011.

[46] F.J. Wiesner. A review of slip factors for centrifugal impellers. *Journal of Engineering Power*, 189(4), 1967.

[47] T. Wright and P. Gerhart. *Fluid machinery: application, selection, and design*. CRC Press, 2009.

[48] L Zhou, W G Lu, and W D Shi. Piv measurements in a compact return diffuser under multi-conditions. *IOP Conference Series: Materials Science and Engineering*, 52(2):022019, 2013.